Solid Oxide Fuel Cell Propulsion System Fueled by Ammonia

Subjected to a vessel from the Watertaxi Rotterdam Company

L. N. Henderik

Solid Oxide Fuel Cell Propulsion System Fueled by Ammonia

by

L. N. Henderik

to obtain the degree of Master of Science
at the Delft University of Technology,
to be defended publicly on Wednesday March 25, 2020 at 2:00 PM.

Student number:	4301706	
Project duration:	June 12, 2019 – March 25, 2020	
Thesis committee:	Prof. Dr. Ir. P. V. Aravind,	TU Delft, chairman
	Dr. Ir. O. Moultos	TU Delft
	Ir. T. Woudstra	TU Delft
	Ir. S. A. Saadabadi	TU Delft
	Ir. J. N. Stam	TU Delft
	Dr. Ir. G. van Zee	Proton Ventures, Advisor

This thesis is confidential and cannot be made public until March 26, 2020.

Acknowledgements

Starting my MSc Energy & Process Technology in 2017 was with a reason: I wanted to contribute to a more sustainable world. I see a bright future for fuel cells, expelling the outdated conventional fossil burning engines. During my internship I studied the proton exchange membrane fuel cell fueled by hydrogen. I was delighted to expend my knowledge in the field by starting my MSc thesis at Proton Ventures: researching the solid oxide fuel cell fueled by ammonia.

I would like to thank Giorgio Fagioli, for establishing this MSc thesis opportunity at Proton Ventures. Special gratitude to Gerard van Zee, being my daily supervisor at Proton Ventures. Guiding me through the process, not only discussing the technical matters, but to see the bigger picture.

Also many thanks to Ali Saadabadi and Jelle Stam, my daily supervisors at the Technical University Delft. Their knowledge about solid oxide fuel cells was of great importance in order to discuss issues occuring in the MSc thesis and beyond. Finally I would like to thank professor Aravind for completing the MSc thesis in his fuel cell group and being my committee chairman.

Last but not least I want to thank Amogh Amladi, my fellow student graduating on the solid oxide fuel cell as well. Many discussion have taken place, contributing to the quality of the MSc thesis.

Abstract

As a result of the Paris Agreement, energy technologies require to shift from fossil fuel based to carbon neutral. In 2015, the maritime sector was responsible for 2.6 % of the global CO_2 emissions. The combination of the solid oxide fuel cell fueled by sustainable synthesized ammonia is seen as a potential solution to reduce emissions. Ammonia is considered as a balanced solution in terms of ease of storage, volumetric energy density and cost of production. The solid oxide fuel cell is generally regarded to be a promising technology owing to its high efficiency and combined heat and power usage. This MSc thesis investigates the technical viability of a sustainable SOFC propulsion system fueled by ammonia. Technical viability is expressed in equipment weight and volume, whereas sustainability is determined by efficiency and emissions. The solid oxide propulsion system is subjected to a case study: A diesel engine powered vessel from the Watertaxi Rotterdam company with an assumed shaft power of 25 kW. A model was compiled to determine the efficiency, weight and volume of the solid oxide fuel cell system. The model covers activation losses, ohmic losses and diffusion losses within the solid oxide fuel cell stack. With the model, a sensitivity study with a selected set of system parameters was performed to gain insight in the solid oxide fuel cell system. The selected system parameters are: Number of cells in the stack, single-pass fuel utilization, cathode off-gas recirculation rate and anode off-gas recirculation rate. The final solid oxide fuel cell system has a significantly higher efficiency based on the higher heating value than the diesel engine system: 46.0 % versus 35.0 % respectively. Also, no carbon dioxide is emitted, leading to a reduction of 56.9 ton per year. Furthermore, nitrogen oxide emissions are considered to be negligible compared to the diesel engine system. However, the weight and volume of the solid oxide fuel cell system are significantly larger: 1199 kg versus 278 kg and 1175 L versus 432 L respectively. Mainly caused by the battery module, required for compensating for temporarily imbalances between power demand and power supply. As a result, it is concluded that the solid oxide fuel cell system is unpractical for the small inland vessel selected for the case study. larger sized vessels have more potential for the application, because large sized vessel sail more continuously, reducing the battery capacity requirement, may allow for more tolerance regarding heavy and bulky equipment and have more benefit of the higher efficiency due to a lower refuel frequency.

Abbreviations

AC	Alternating Current
CHP	Combined Heat and Power
DC	Direct Current
FoS	Factor of Safety
GDC	gadolinium-doped Ceria
GHG	Greenhouse Gasses
HFO	Heavy Fuel Oil
HOR	Hydrogen Oxidation Reaction
ICE	Internal Combustion Engine
IMO	International Maritime Organization
LHV	Lower Heating Value
LMTD	Logarithmic Mean Temperature Difference
LSM	Lanthanm Strontium Manganite
LSCF	Lanthanum Strontium Cobalt Ferrite
NO_x	Nitrogen Oxides
PEMFC	Proton Exchange Membrane Fuel Cell
PEN	Anode-Electrolyt-Cathode
SoC	State-of-Charge
SOFC	Solid Oxide Fuel Cell
SO_x	Sulphur Oxides
SSECA	Solid State Energy Conversion Alliance
YSZ	Yttria-Stabilised Zirconia

Nomenclature

Physical constants

F	Faraday's constant	96485 C/mol_{e^-}
g	Gravitational constant	9.81 m/s^2
μ	Number of electrons	2 mol_{e^-}/mol_{H_2}
R	Universal gas constant	8.314 $J/mol/K$

Greek Symbols

α	Transfer coefficient
β	Symmetry factor
ϵ	Ohmic resistance
η	Efficiency
κ	Thermal conductivity
λ	Heat transfer coefficient
ρ	Density
σ	Conductivity
τ	Thickness
ϕ	Voltage
ψ	Yield strength

Other Symbols

A	Area
a	Activity
b	Pre-exponential factor
D	Diffusion coefficient
d	Diameter
E	Energy
e	Specific exergy
f	Fugacity coefficient
G	Gibbs free energy
g	Specific Gibss free energy
H	Height
h	Specific enthalpy
I	Current

i	Current density
i_o	Exchange current density
k	Rate constant
L	Length
M	Molar mass
m	Mass
$\dot{m}$	Mass flow
Nu	Nusselt number
n	Number of moles
$\dot{n}$	Molar flow
P	Power
Pr	Prantl number
p	Pressure
$\dot{Q}$	Heat transfer
Ra	Rayleigh number
r	Recirculation rate
S	Stoichiometric coefficient
s	Specific entropy
T	Temperature
t	Time
U_f	Single-pass fuel utilisation
V	Volume
$\dot{V}$	Volumetric flow rate
W	Width
$\dot{W}$	Work per time
y	Molar fraction
$\#_{cells}$	Number of cells

Subscripts

a	Anode
ac	Air channel
act	Activation
amb	Ambient

b	Boundary
bm	Battery module
c	Cathode
ch	Chemical
cir	Circuit
$conv$	Converter
d	Destruction
$diff$	Diffusion
e	Outlet
em	Electromotor
el	Electrolyte
fc	Fuel channel
gw	Glass wool
hex	Heat exchanger
i	Inlet
in	Insulation
int	Interconnection
inv	Inverter
j	Species
o	Standard
rev	Reversible
TPB	Triple phase boundary
tm	Thermo-mechanical

Contents

1 Introduction

As a result of the Paris Agreement COP21 on climate change, energy technologies require to shift from fossil fuel based to carbon neutral. In 2015, the maritime sector was responsible for 2.6% of global CO_2 emissions [1]. The International Maritime Organization (IMO) has set the goal to reduce greenhouse gasses (GHG) by 50% and carbon-intensity by 70% in 2050 with respect to 2008 [2]. To achieve this, sustainable fuels and innovative technologies play a crucial role.

The combination of sustainable synthesized ammonia fuel and solid oxide fuel cell (SOFC) technology is considered as a potential solution by the Dutch company Proton Ventures. Proton Ventures develops NFuel technology: Decentralized production of ammonia using renewable energy resources. Nitrogen is extracted from the air. Hydrogen is produced by electrolysis of water using renewable electricity from e.g. wind or solar. Nitrogen and hydrogen are converted into ammonia by the Haber-Bosch process. With regard to maritime application, Proton Ventures currently studies the realization of a prototype propulsion system fueled by a carbon free fuel. The potential for ammonia as fuel has been investigated for propulsion systems based on the SOFC, internal combustion engine (ICE), proton exchange membrane fuel cell (PEMFC) and steam engine.

This document reports a MSc thesis research on the application for ammonia fueled SOFC technology in maritime propulsion systems. A vessel owned by the Watertaxi Rotterdam company has been selected as case study. A model was compiled to investigate performance characteristics and initial system equipment dimensions and layout.

1.1 Ammonia as Sustainable Maritime Fuel

As mentioned, Proton Ventures has the ambition to use sustainable ammonia as maritime fuel. Key properties of ammonia are given in Table 1.

Table 1: *Properties of ammonia.*

Molar mass	17.031	g/mol
Hydrogen mass	17.8	wt%
Density (25 °C, 1 atm)	0.699 [3]	kg/m^3
Density (liquid)	696 [3]	kg/m^3
Melting point (1 atm)	-77.7 [4]	°C
Boiling point (1 atm)	-33.4 [4]	°C
Higher heating value	22.5 [5]	MJ/kg
Lower heating value	18.6 [5]	MJ/kg
Flammability range	15-28 [5]	%
Auto ignition	903 [4]	K
Adiabatic flame temperature	2073 [5]	K
Laminar flame speed	0.07 [5]	m/s

Next to ammonia, hydrogen is a sustainable fuel with an established reputation. Ammonia has a lower gravimetric lower heating value (LHV) than hydrogen: 18.8 versus 120 kJ/kg [5]. However, hydrogen is commonly stored under pressure to increase the volumetric energy density. This approach generally requires storage systems of relatively high weight. The company NPROXX, for example, manufactures hydrogen gas storage cylinders for pressures up to 350 bar with a weight of 12.8 kg per kg hydrogen. Accounting for the equipment weight leads to a gravimetric energy density of hydrogen when stored of 8.7 kJ/kg. In contrast, ammonia is easier to liquefy by cooling, owing to its relatively low boiling point or by pressurization at pressure levels at 10 bar and 25 °C [6]. Whereas hydrogen must be cooled to -253 °C [7] to be liquid. But even then, the volumetric LHV is lower than ammonia, as can be seen in Figure 1.

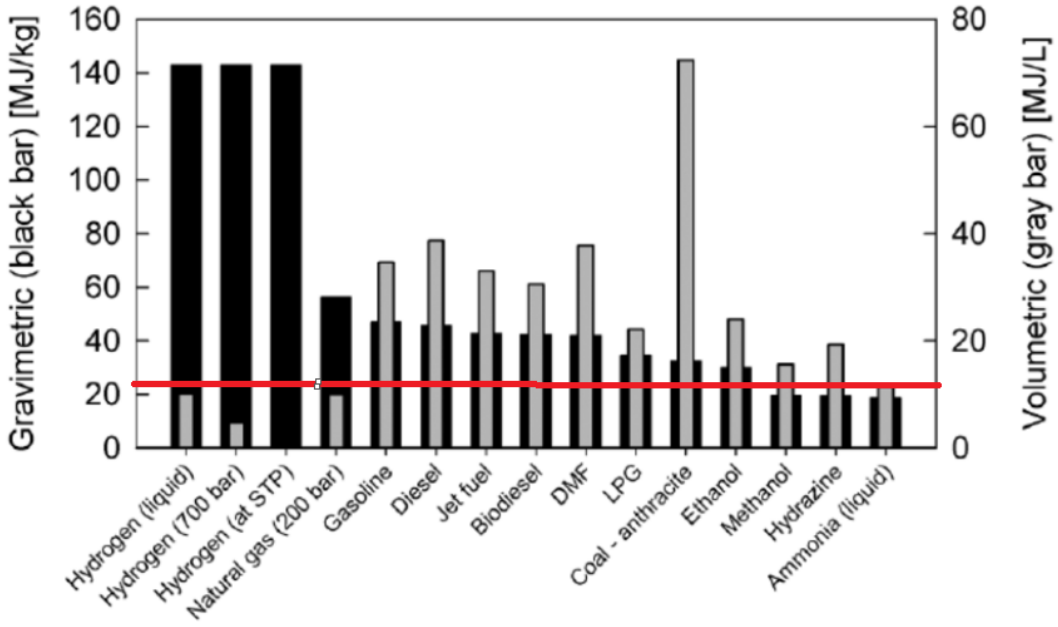

Figure 1: *Gravimetric and volumetric lower heating value of various chemical compounds. The red line represents the volumetric lower heating value of ammonia [8].*

A downside of ammonia is its toxicity, However, ammonia is easily detected by the human nose under 1 ppm [9]. Furthermore, ammonia is corrosive. However, experience in the well established distribution net, that, in contrast to hydrogen, already exists can cope with these issues. In 2018, 180 million tonnes of ammonia was produced. This makes it the sixth largest chemical produced in the world [10]. Bartels [11] has performed a feasibility study of the implementation of an ammonia economy. A cost comparison of production, storage and transportation of hydrogen versus ammonia was made. The results are shown in Table 2.

Table 2: *Cost comparison of production, storage and transportation of hydrogen versus ammonia [11]. The ammonia values are normalized to hydrogen.*

	Hydrogen [\$/kg H_2]	Ammonia [\$/kg H_2]
Production	3.00	3.80
Pipeline transport	1.87	0.19
Storage - 15 days	1.97	0.06
Storage - 182 days	14.95	0.54

Table 2 shows that the cost of transport and storage of ammonia versus hydrogen is order of magnitudes lower. Storage of fuel is an important aspect for large cargo ships. Which are at sea for days or weeks.

The role of ammonia as sustainable maritime fuel has also been recognized in a study performed by DNV GL [2] on shipping fuels for the future. This study expects widespread commercial adoption of ammonia fuel beginning in 2037. By 2050, 25% of the maritime fuel usage consists of ammonia, which translates to approximately 120 million tons of ammonia per year, representing two thirds of today's global ammonia production. From 2044 onwards, DNV GL predicts that more than 90% of the new build vessels will be fueled by ammonia. Figure 2 shows the prediction of the maritime fuel mix till 2050. Hydrogen does not play a significant role in this forecast.

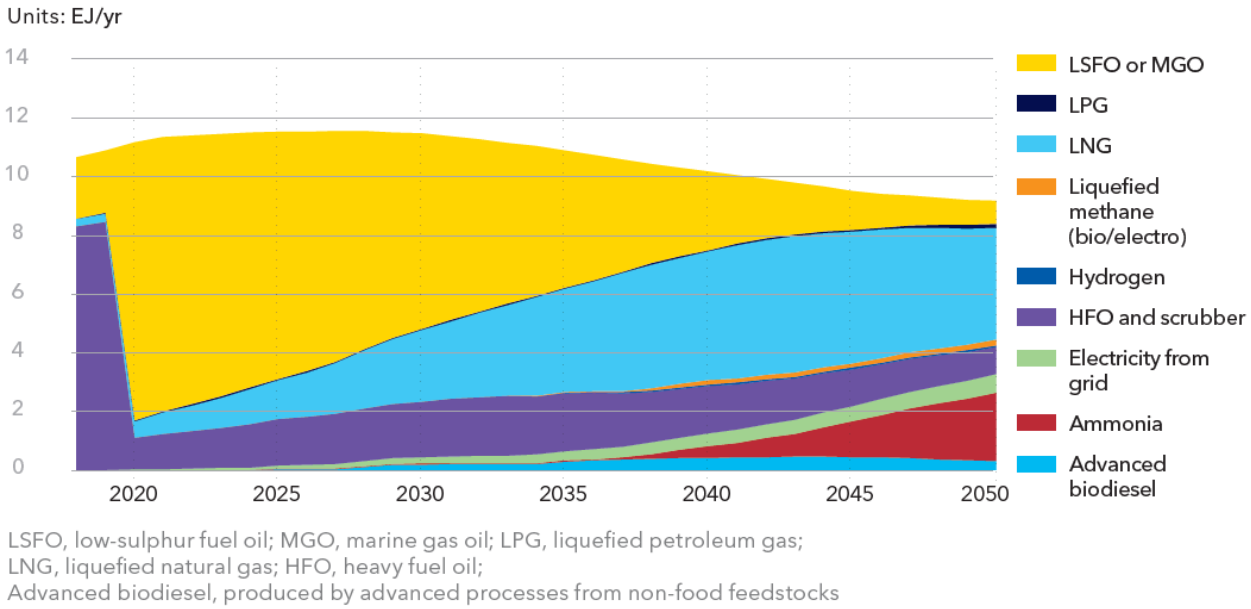

Figure 2: *Predicted maritime fuel mix till 2050 by DNV GL [2].*

1.2 Solid Oxide Fuel Cell Technology

The SOFC electrochemically converts hydrogen and oxygen to water, producing electricity and heat. Air is used to provide the oxygen and for cooling purposes. The operating temperature of the SOFC lies between 500 and 1000 °C [12]. The high operating temperature offers high reaction rates without the need for expensive catalysts, such as platinum for PEMFCs. Also, hydrocarbons can be internally reformed and other types of fuels, such as ammonia, can be internally cracked when selecting the appropriate catalyst [12] [13]. This makes the SOFC flexible in fuel choice. Furthermore, the exhaust heat of the SOFC gives potential to combined heat and power (CHP) applications. Figure 3 gives and indication of the electrical efficiency and electrical power output range for various technologies, including the SOFC.

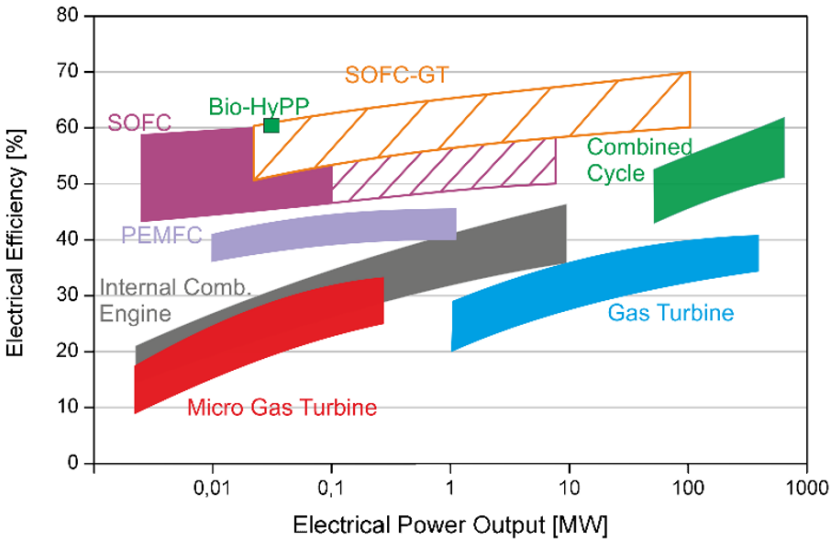

Figure 3: *Electrical efficiency and electrical power output for various energy technologies [14].*

The SOFC commonly contains ceramic material for the anode-electrolyte-cathode (PEN) structure and metal alloys for the interconnections and frame structure [15]. Due to mismatch between thermal expansion coefficients during start-up operations, thermal stress can give complications. Also, sealing is an issue for planar SOFCs [16]. To avoid implications with the different materials, the fuel and oxidant entering the SOFC need to be preheated. Also, response and start-up operations should be done gradually. This leads to a long start-up and slow response [16]. Therefore, SOFCs are not practical for transient operations. General properties of the SOFC are summarized in Table 3.

Table 3: *General properties solid oxide fuel cell.*

Operating temperature	500 - 1000 °C [12]
Electrical efficiency	45 - 60% [14]
Operating cell voltage	0.7 - 0.8 V [17]
Main characteristics	Internal reforming Fuel flexibility Combined heat and power

1.3 Selected case study

The vessel selected for the case study, as used by the Watertaxi Rotterdam company, is powered by a diesel engine. Information of the vessel has been obtained through internal communication. The engine has a weight of 229 kg and a volume of 384 L. The LHV efficiency is approximately 35%. The vessel is shown in Figure 4.

Figure 4: *Selected vessel form the Watertaxi Rotterdam company [18].*

When the vessel is in service, a shaft power of 25 kW for 8 hours per day is assumed. For 25 kW shaft power, 71.4 kW chemical power from heavy fuel oil (HFO) is needed. The LHV of HFO is 41.8 MJ/kg [19]. The resulting HFO consumption is 49.2 kg per day. The density of HFO is 0.98 kg/L [19]. Therefore, the HFO occupies a volume of 50.2 L in the fuel tank.

A publication by SenterNovem [20] provides a list of standard carbon dioxide emission factors. HFO has a carbon dioxide emission of 3201 g_{CO_2}/L. The assumed HFO consumption of the case study results into a carbon dioxide emission of 58.7 ton/year.

1.4 Research Objective

The objective of the research work in this MSc thesis is to investigate the technical viability of a SOFC propulsion system fueled by sustainable synthesized ammonia. Viability is expressed in this MSc thesis in terms of equipment weight and equipment volume, whereas sustainability is expressed in efficiency and emissions. A cost analysis and the potential of CHP is out of the scope of this MSc thesis. Questions to be answered are:

- What are the components of the SOFC propulsion system?
- Which system parameters influence the system's efficiency, equipment weight and equipment volume?
- What are the optimal system parameters for the SOFC propulsion system?
- What decrease in GHG reduction can be achieved?
- What are the most important exergy loss mechanisms in the SOFC propulsion system?

2 Literature Study

Chapter 1 ended by defining the objective of this MSc thesis: Investigate the viability of a SOFC propulsion system fueled by sustainable synthesized ammonia. This chapter is divided into two parts. Section 2.1 focuses on the general operation principle of SOFCs fueled by ammonia. Section 2.2 concentrates on the characteristics of SOFC ammonia propulsion systems as reported in literature. A summary of this chapter is given in in section 2.3.

2.1 Solid Oxide Fuel Cell Fueled by Ammonia

2.1.1 Working Principle

The SOFC fueled by ammonia is characterized by a two-stage process [21]. First, endothermic cracking of ammonia occurs at the anode owing to the high operating temperature and catalyst activity. The reaction mechanism is given by Equation 1.

$$2NH_3 \rightarrow 3H_2 + N_2 \qquad \Delta h_{298K} = 46.2\ kJ/mol_{NH_3} \tag{1}$$

where h is the specific enthalpy.

The decomposition equilibrium of ammonia into its constituent elements depends strongly on temperature and pressure, as seen in Figure 5. In accordance with Le Chatelier's principle, an endothermic reaction is favored by a higher temperature and if the total number of moles in a reaction increases, favored by a lower pressure.

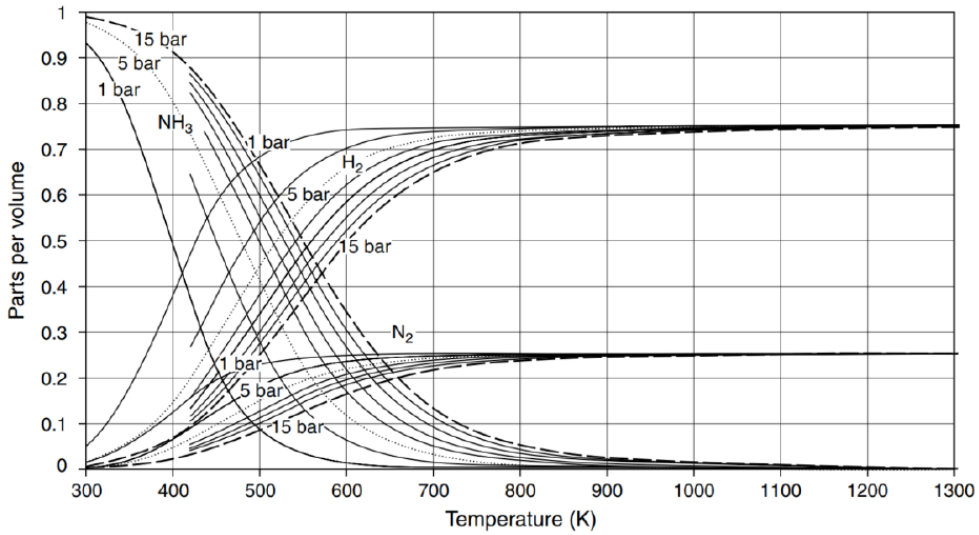

Figure 5: *Thermodynamic equilibrium of ammonia, hydrogen and nitrogen as function of temperature and pressure [22].*

At 450 °C and 1 bar, more than 99% of the ammonia is decomposed into its constituent elements when reaching equilibrium. However, the conversion rate is slow [23].

Ni et al. [24] developed a thermo-electrochemical model to investigate electrochemical reactions in a planar SOFC fueled by ammonia. Cracking of ammonia, is besides temperature and pressure, dependent on the flow velocity of ammonia in the cell. The higher the flow velocity, the lower the residence time, the lower the conversion of ammonia into nitrogen and hydrogen. The ammonia fraction over the length of the anode obtained from the model by Ni et al. [24] is shown in Figure 6.

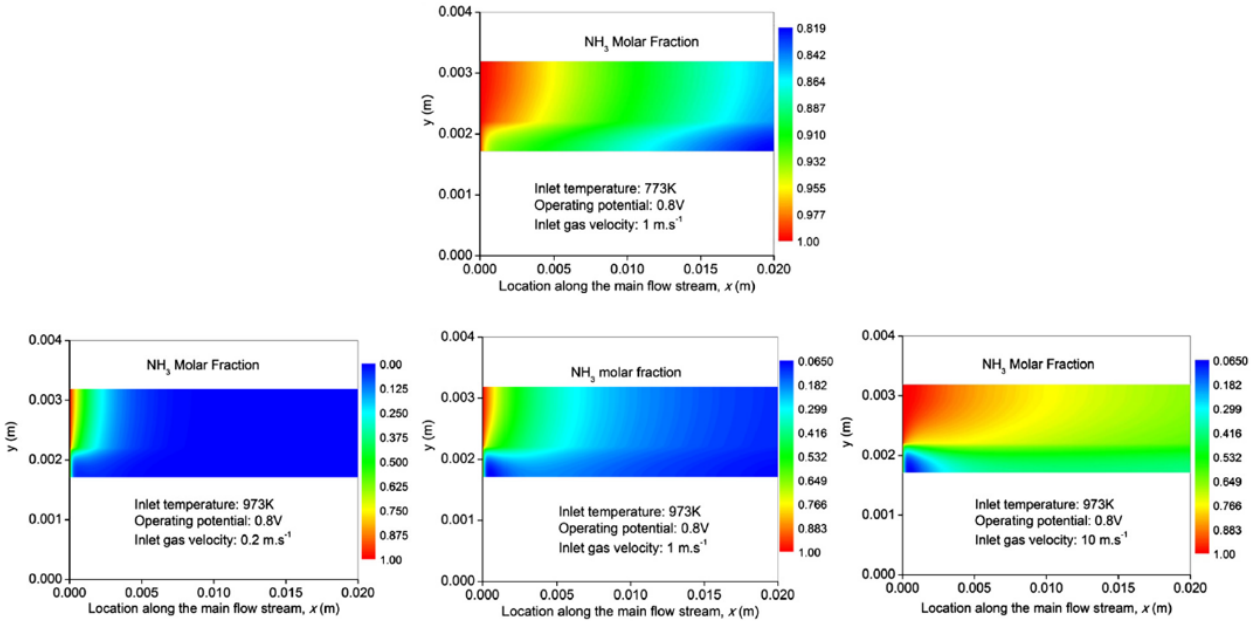

Figure 6: *Ammonia molar fraction as function of location at 1 bar. The y-axis scale denotes the cell path length: From 1.7 to 2.2 mm is the porous anode and from 2.2 to 3.2 is the fuel channel [24].*

Figure 6 shows that ammonia is practically completely cracked a high temperatures above 700 °C and moderate flow velocities below 1 m/s.

After cracking ammonia, the hydrogen oxidation reaction (HOR) takes place. The HOR consists of a oxidation and reduction reaction. For the oxidation reaction, hydrogen combines with oxygen ions at the anode forming water and electrons as in Equation 2. To prevent starvation of the anode, not all the hydrogen can be used. Therefore, the single-pass hydrogen utilization U_f is lower than 100 %. The released electrons travel in an external circuit and combine with oxygen at the cathode to form oxygen ions as in the reduction Equation 3. The oxygen ions travel through the solid electrolyte from the cathode to the anode which balances the charges in the system.

$$H_2 + O^{2-} \underset{\text{c}}{\overset{\text{a}}{\rightleftharpoons}} H_2O + 2e^- \tag{2}$$

$$\frac{1}{2}O_2 + 2e^- \underset{\text{a}}{\overset{\text{c}}{\rightleftharpoons}} O^{2-} \tag{3}$$

where subscript a denotes the anode and subscript c denotes the cathode.

At both the anode and cathode, there is a forward and a backward reaction, resulting in an equilibrium. At the cathode, the forward reaction is denoted by subscript c. At the anode, the forward reaction is denoted by subscript a. By combining Equations 2 and 3, the overall HOR reaction is obtained as in Equation 4.

$$H_2 + \frac{1}{2}O_2 \rightleftharpoons H_2O \qquad \Delta h_{298\ K} = -285.8 kJ/mol H_2O \tag{4}$$

The HOR is highly exothermic relative to endothermic cracking of ammonia. If 1 mol ammonia is cracked and subsequently all the hydrogen is oxidized, the enthalpy of reactioin is -405.6 kJ/mol NH_3. Therefore, the overall process is exothermic. As a result the SOFC needs to be cooled to maintain its temperature. The air, also providing the oxygen, is used as a coolant. Figure 7 gives the schematic operating principle of the SOFC fueled by ammonia.

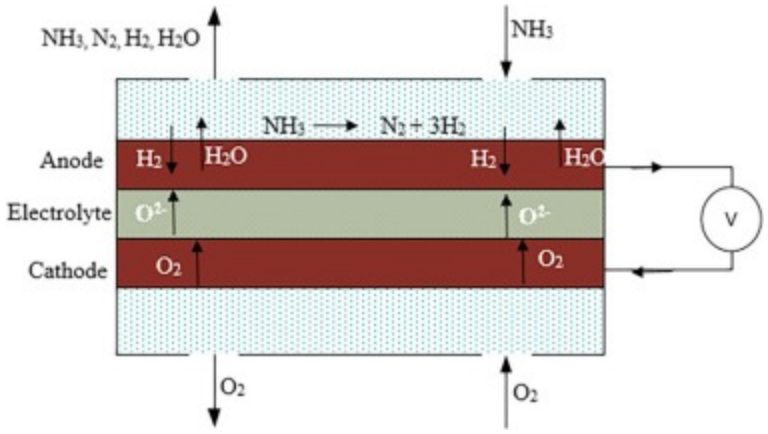

Figure 7: *Operating principle of the solid oxide fuel cell fueled by ammonia [25].*

Thermal conduction, convection and radiation within the SOFC stack define the temperature distribution. The better the heat transfer within the SOFC, the more uniform the SOFC stack and the smaller the temperature difference between the anode and cathode outlet. Aguiar et al. [26] mathematically modelled a 1-dimensional internal reforming SOFC stack fueled by methane. The temperatures of the air channel, PEN structure, fuel channel and interconnection as function of electrode length are plotted in Figure 8.

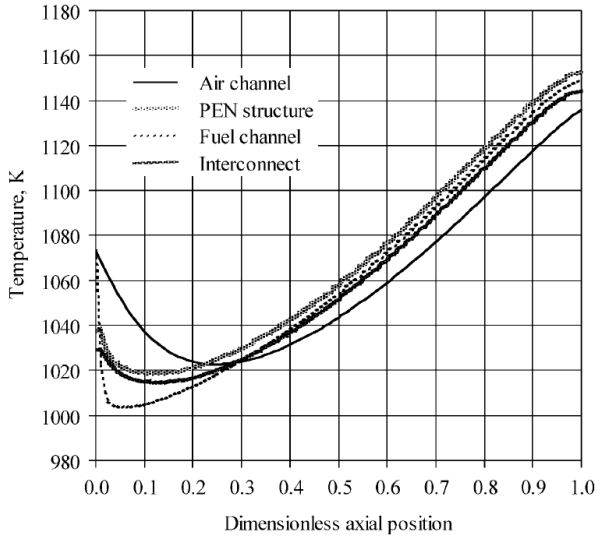

Figure 8: *Temperature of the air channel, PEN structure, fuel channel and interconnection as function of dimensionless axial position [26].*

Figure 8 shows that the temperature gradients follow closely, indicating good heat transfer within the SOFC stack. Also, the outlet temperature of the fuel channel and air channel only differ by approximately 5 °C.

As discussed in Section 1.2, a single SOFC operates between 0.7 and 0.8 V [17]. To increase system the voltage, SOFCs are stacked in series. Bipolar plates are commonly used [15]. For a bipolar plate, the anode and cathode of two different cells are placed opposite to each other. An interconnection is placed in between. Electrons travel from the anode, via the interconnection, to the cathode. The voltage is collected between the beginning and end of the stack. The principle is shown in Figure 9.

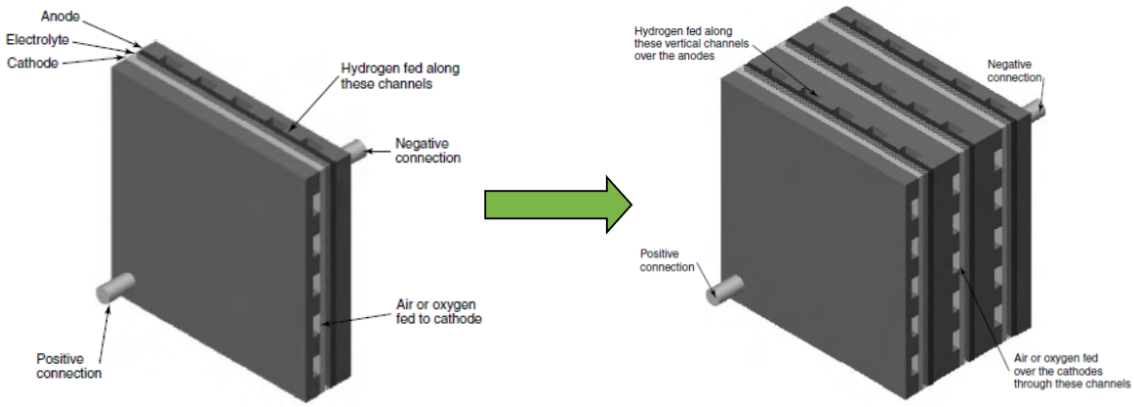

Figure 9: *Stacking of bipolar solid oxide fuel cells in series [15].*

Less exotic and expensive materials are used in SOFC than in many other fuel cell technologies [15]. A widely used material for the anode is a nickel cermet, such as a combination of nickel with yttria-stabilized zirconia (YSZ) [15]. The solid electrolyte has the function to transport ions and to avoid the transport of gas, which causes voltage losses. Widely used electrolyte materials for SOFCs are YSZ or doped ceria [15]. For the cathode, lanthanm strontium manganite (LSM) and lanthanum strontium cobalt ferrite (LSCF) compositions are widely used [15]. For the interconnection, electron resistance should be minimized to prevent voltage losses. Metals conduct well. However, due to the high operating temperature alloys are used to withstand the high temperature. Therefore, inconel types stainless steel are widely used [15].

2.1.2 Feasibility

Today's SOFC-systems use hydrocarbon fuels to provide for the hydrogen [27]. However, the feasibility of ammonia fuel in SOFCs has been showed by numerous experiments.

According to Cinti et al. [28], Wojcik et al. [29] were the first to conduct experiments with an SOFC fueled by ammonia in 2003. Wojcik et al. [29] conducted experiments with a tubular SOFC, consisting of a YSZ electrolyte. The operating temperatures were between 800 and 1000 °C. For comparison, hydrogen experiments were conducted. The anode was different in three experiments: silver, silver with an iron catalyst and platinum. For the first experiment, hydrogen has a significant higher voltage than ammonia. Indicating that ammonia is relatively inactive on silver. When adding the iron catalyst, ammonia voltage was close to hydrogen voltage. Also for the platinum, ammonia and hydrogen voltages were similar, as seen in Figure 10.

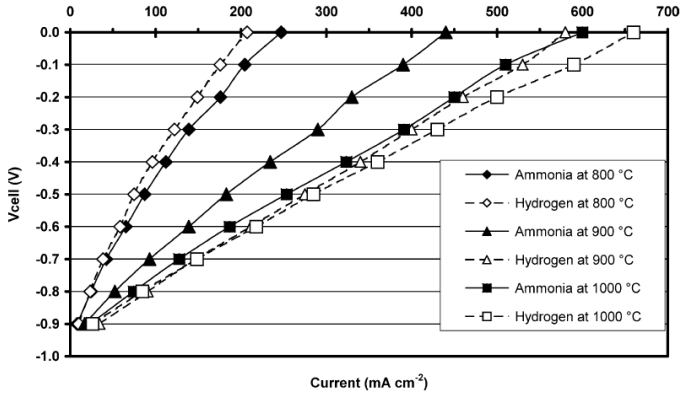

Figure 10: *Polarization curves ammonia fueled solid oxide fuel cell with a platinum anode at 800, 900 and 1000 °C by Wojcik et al. [29].*

Figure 10 indicates a better ammonia performance compared to hydrogen at 800 °C. This phenomena is not explained by Wocjik et al. [29]. A reason could be the cooling effect of ammonia cracking, leading to a better thermal stability [13].

Fuerte et al. [9] conducted experiments with a commercial microtubular SOFC. The electrolyte consisted of YSZ, the anode was a cermet of nickel and YSZ and the cathode was LSM based. Fuerte et al. [9] used the cheaper nickel cermet in contrast to the silver/platinum used by Wojcik et al. [29]. The anodic feed, initially 100% hydrogen, was completely, but gradually, replaced by ammonia. The cathode was exposed to atmospheric air. The operating temperature was 700 °C. Figure 11 gives the polarization curves of the experiments.

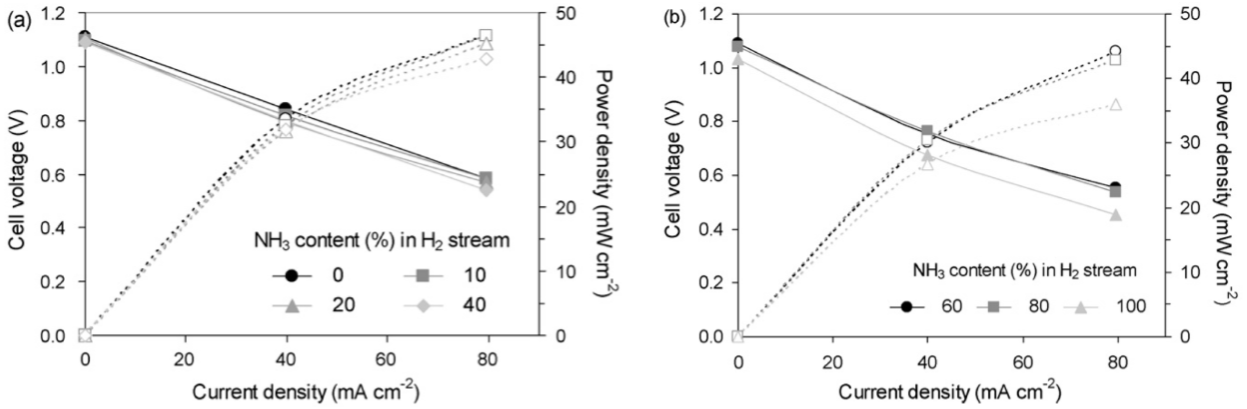

Figure 11: *Voltage and power density as function of the current density from experiments by Fuerte et al. [9].*

Figure 11 shows that replacing ammonia by hydrogen slightly decreases the cell performance. Fuerte et al. [9] explain this phenomena by the lower partial pressure of hydrogen due to co-production of nitrogen when ammonia is cracked.

In 2019, the University of Perugia conducted experiments with an ammonia fueled SOFC in collaboration with Proton Ventures. The information from the experiments has been obtained through internal communication. The SOFC was a planar anode supported cell, consisting of a cermet of nickel and YSZ. The electrolyte consisted of YSZ and the cathode of a bi-layer of gadolinium-doped ceria (GDC) & LSCF. Hydrogen experiments were conducted as reference.

First, the voltage decay over time was measured at a constant furnace temperature of 750 °C. It was found that the voltage decay for both ammonia and hydrogen were similar, 1.4% and 1.5% per 100h respectively at a current density of 1025 mA/cm^2. For ammonia this results in 12.5 mV/100h. Already in 2009, the Solid State Energy Conversion Alliance (SSECA) reported achieved degradation of 1.7 and 2.6 %/1000h [30]. Therefore, the degradation in the experiment of Perugia can be considered as excessively. During the experiment, neither nitrogen oxides (NO_x) nor ammonia were detected in the off-gasses, with a detection limit of 50 ppm.

Secondly, polarization curves for pure hydrogen, nominal hydrogen and ammonia were measured at a constant furnace temperature of 750 °C. Nominal hydrogen refers to an equivalent mix of hydrogen and nitrogen when ammonia would completely crack according to Equation 1. The polarization curves are given in Figure 12.

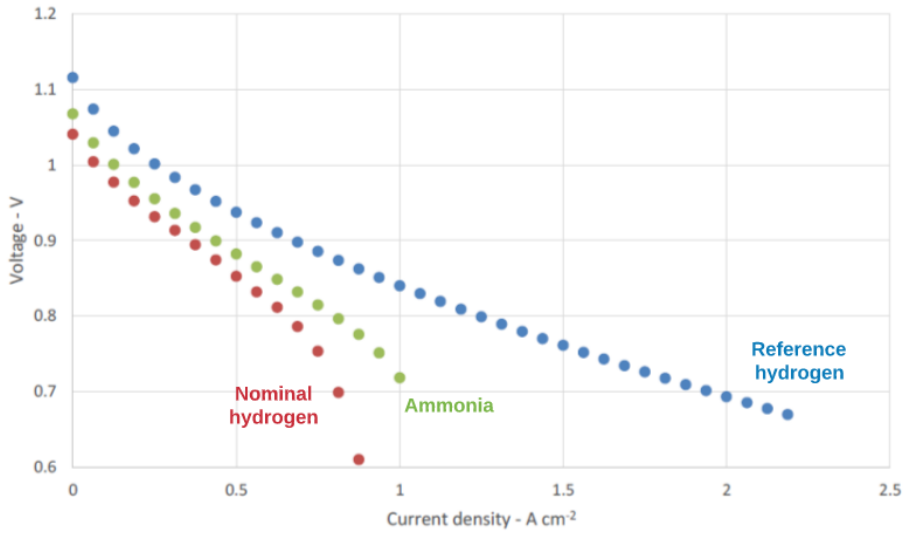

Figure 12: *Polarization curves measured by the University of Perugia.*

Figure 12 shows that the performance ammonia is lower than pure hydrogen. Explained by to the lower partial pressure of hydrogen in the ammonia case. No explanation was given for the observed improved performance of ammonia as compared to nominal hydrogen. A reason could be the better thermal stability, owing to the cooling effect when ammonia is cracked [13].

Numerous experiments with ammonia fueled SOFCs are conducted. However, there is a lot of ambiguity regarding the performance of ammonia. Some studies report a decreased performance explained by the lower partial pressure of hydrogen. Other experiments report an increased performance of ammonia compared to hydrogen. One reason could be a better thermal stability, owing to the cooling effect when ammonia is cracked. However, the experiments have in common to have shown the feasibility of ammonia as a fuel for the SOFC.

2.1.3 Emissions

Undesired gas emissions in the maritime sector are carbon dioxides, sulphur oxides (SO_x) and NO_x. In an combustion engine, these emissions are emitted when burning HFO, which contains traces of sulphur. Because ammonia does not contain any carbon or sulphur, these emissions are eliminated. NO_x, however, can still be formed due to the high operating temperature of the SOFC.

The oxidation of nitrogen to NO_x is described by the Zel'dovich mechanism [31]. This mechanism is essentially given by Equation 5.

$$\begin{aligned} N_2 + O &\rightleftharpoons NO + N \\ N + O_2 &\rightleftharpoons NO + O \\ Overall : N_2 + O_2 &\rightleftharpoons 2NO \end{aligned} \tag{5}$$

The first reaction is rate-determining. The rate constant k for the first reaction is given in Equation 6 [31].

$$k = 1.44E13 \cdot T^{0.3} \cdot \exp \frac{-75286081}{R \cdot T} \tag{6}$$

where T is the temperature and R is the universal gas constant.

The rate constant is plotted as a function of temperature in Figure 13. The common operating temperatures of the SOFC (800 °C) and the ICE (1500 °C) are also indicated in Figure 13.

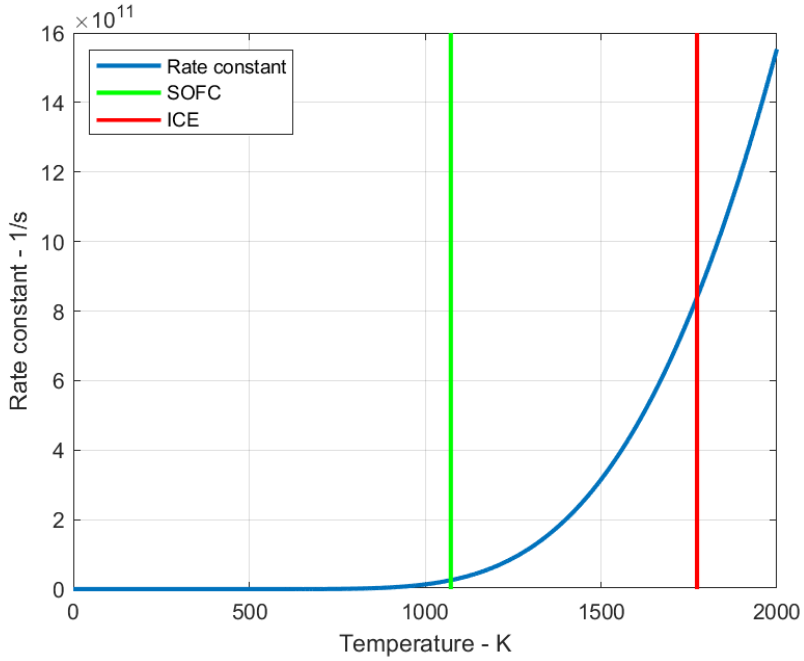

Figure 13: *Rate constant of the rate determining reaction in the formation of nitrogen oxide as function of temperature.*

Figure 13 shows that the rate constant at the operating temperature of the SOFC is small, in contrast to the value at the operating temperature for ICE. Multiple studies confirm the absence of NO_x formation in SOFC [21, 25]. Also, as discussed in section 2.1.2, no NO_x formation was detected in the experiments of the university of Perugia up to a detection limit of 50 ppm.

2.2 Ammonia Propulsion Studies

2.2.1 Study Proton Ventures

As discussed in Chapter 1, Proton Ventures has studied the efficiency of the ICE, PEMFC, SOFC and steam engine using process simulations. The simulations were focused on a medium size ship with a rated power output of 8 MW. The ship operates at full load and steady-state. Ammonia is stored as a liquid at 1 atm and -33 °C. The results of this study have been obtained through internal communication.

Internal Combustion Engine

It is expected by Proton Ventures that ammonia can be used in an ICE with minor adjustments. The combustion of ammonia is given in Equation 7.

$$4NH_3 + 3O_2 \rightarrow 2N_2 + 6H_2O \tag{7}$$

Equation 7 gives the stoichiometric combustion of ammonia. In practice, excess air is used as the oxidant. This leads, in the operating temperature domain of the ICE as in Figure 13, lead to the formation of NO_x.

Stored, liquefied ammonia is compressed and heated in a heat exchanger by the exhaust gases until vapor state. The ICE is modelled by piston compression, combustion, according to Equation 7, and piston expansion. A turbocharger and intercooler are used to boost the efficiency of the system. The turbocharger is fed by a second turbine.

Proton Exchange Membrane Fuel Cell

The PEMFC uses hydrogen for the electrochemical reaction to produce electricity. Therefore, ammonia needs to be cracked into its constituent components. This ammonia cracking has to be done externally due to insufficient temperature in the PEMFC.

Stored, liquefied ammonia is heated in a heat exchanger by the outlet of the external cracker. The cracker is assumed to reach a conversion of 100% at 900 °C. The cracked mixture has to be converted to pure hydrogen for the PEMFC. The separation of nitrogen in the mixture happens at an elevated pressure of 5 bar, achieved by a compressor, and 450 °C, achieved by a heat exchanger. After purification, part of the hydrogen is entering the PEMFC and the remaining part is used in a afterburner. The heat from the afterburner is used to compensate for the endothermic cracking of ammonia. The operating temperature of the PEMFC is 65 °C. This temperature is achieved by a cooler after the heat exchanger.

Solid Oxide Fuel Cell

The SOFC propulsion system as modelled by Proton Ventures in shown in Figure 14.

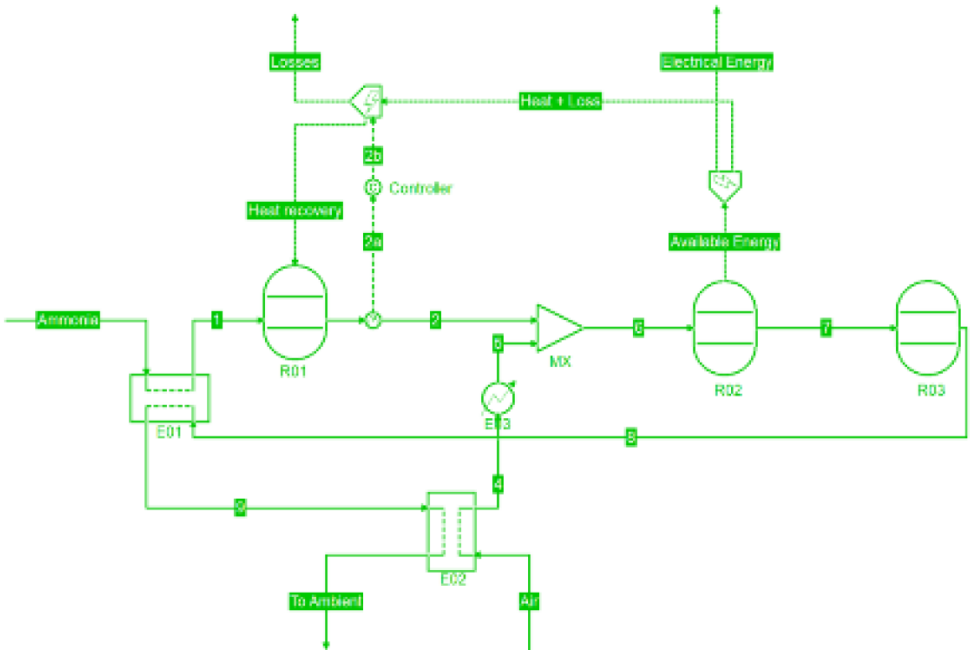

Figure 14: *Solid oxide fuel cell propulsion system model by Proton Ventures.*

Stored, liquefied ammonia is heated in heat exchanger E01 by the exhaust gases. The SOFC, operating at 650 °C, is modelled by two reactors: R01 carries out the cracking of ammonia and R02 carries out the HOR. To prevent starvation of the anode, 20% excess ammonia (equal to a single-pass fuel utilization of 83.3 %) is used. Ammonia is assumed to crack completely. Air is supplied with an air-to-fuel ratio of 3 and heated in heat exchanger E02 by the exhaust gases. The remaining preheating of the air stream during operation is done by electrical heater E03. The unreacted hydrogen is burned in afterburner R03.

Steam Engine

A steam engine uses the heat from the combustion of ammonia with air, as in Equation 7. Stored, liquefied ammonia is directly mixed with air and burned. The heat is used to evaporate water. The water vapor passes a turbine to produce work. The turbine's exhaust water vapor is condensed and compressed to close the cycle.

Main Conclusions Study Proton Ventures

The ammonia consumption required to produce 8MW shaft power was obtained by simulation of the investigated propulsion systems. The efficiency η of each propulsion system was calculated by Equation 8.

$$\eta = \frac{8\ MW}{\dot{m}_{NH_3} \cdot LHV_{NH3}} \tag{8}$$

where $\dot{m}$ is the mass flow.

The ammonia consumption and calculated efficiency for each propulsion system are given in Table 4. The table also lists estimated values for the system's weight and volume.

Table 4: *Ammonia consumption, efficiency, weight and volume for the different propulsion system studied by Proton Ventures.*

Propulsion system	$\dot{m}_{NH3}$ [kg/h]	η [%]	Mass [kg]	Volume [L]
Internal combustion engine	3500	43.0	158	786
Proton exchange membrane fuel cell	5480	28.0	613	1404
Solid oxide fuel cell	2875	53.0		
Steam engine	9877	15.0	1058	2890

The reported equipment sizes exclude auxiliary equipment, such as heat exchangers, compressors, turbines, the condenser for the steam engine and the external cracker for the PEMFC system. The weight and volume estimations of the SOFC-system were not specified.

The steam engine has a very low efficiency due to major heat loses in the condenser. The PEMFC-system has a major disadvantage in the requirement for the removal of nitrogen after external cracking of ammonia. The ICE has a high efficiency and low investment cost. However NO_x formation may be significant owing to high operating temperature. The SOFC-system is identified as the most promising technology because of the high efficiency. Also, no external equipment is needed for cracking of ammonia or purification of hydrogen. Furthermore, the operating temperature is significantly lower compared to the ICE, thereby reducing or even eliminating NO_x emissions.

2.2.2 Solid Oxide Fuel Cell Systems in Literature

In general, only few studies on SOFC-systems fueled by ammonia have been reported in literature.

Dekker [25] reports experiments with an ammonia fueled SOFC. No significant cell voltage differences were observed between pure hydrogen, an equivalent mixture of hydrogen and nitrogen and pure ammonia. Also, ammonia cracking at 800 °C was found to have 99.996% conversion. Furthermore, the cell voltage degradation rate was found to be no more than 0.96%/1000h, which is in line with the targets of the SSECA [30].

Figure 15-A displays a process scheme for an ammonia fueled SOFC-system suggested by Dekker [25]. The anode off-gas is used to preheat the ammonia. The anode off-gas and cathode off-gas are mixed and burned in an afterburner to consume the unreacted hydrogen. The exhaust gas from the afterburner is used to preheat the air feed.

Process simulations performed by Dekker [25] indicate the air heat exchanger as the major component. The size of this heat exchanger can be halved by using the configuration as in Figure 15-B. In this configuration part of the air is preheated by the heat exchanger and the remaining part is preheated by the cathode off-gas between two stacks.

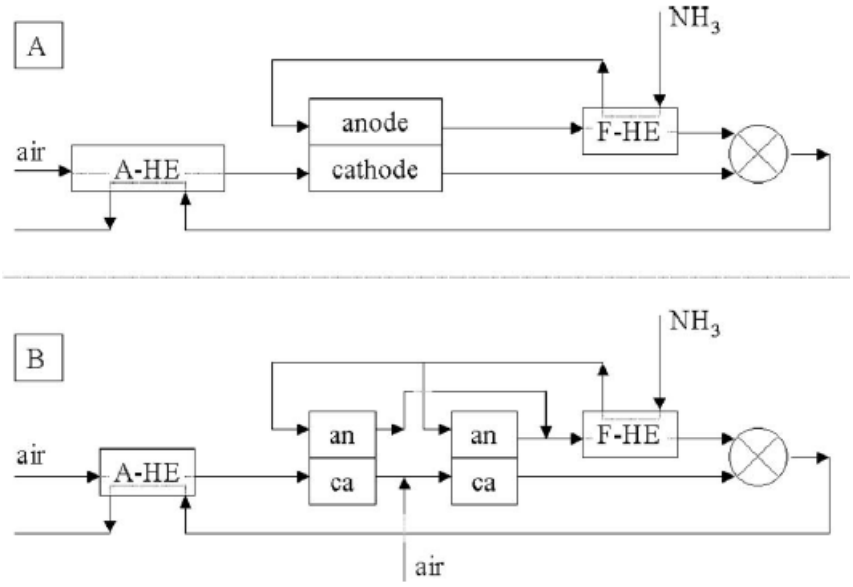

Figure 15: *SOFC-system (A) and suggested configuration for decreasing the air heat exchanger (B) by Dekker [25].*

Farhad et al. [23] modelled a 100 W portable SOFC-system fueled by ammonia, as shown in Figure 16. Liquid ammonia and water are stored under pressure. Ammonia, water and air are preheated in a heat exchanger by the exhaust gas from the catalytic afterburner. In the heat exchanger the temperature is increased, leading already to cracking of ammonia. The remaining ammonia is cracked in the anode.

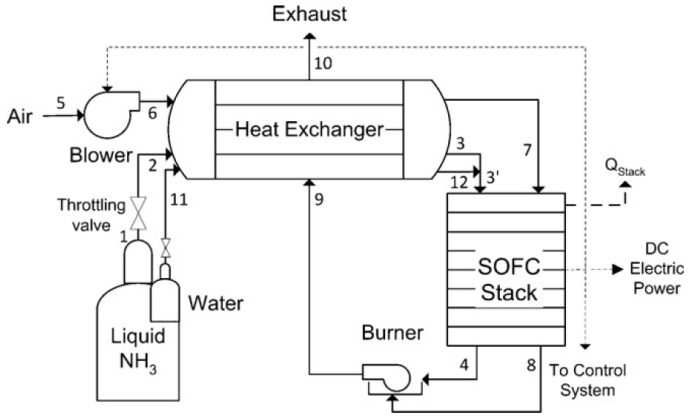

Figure 16: *Solid oxide fuel cell system fueled by ammonia by Farhad et al. [23].*

The computer model was used by Farhad et al. [23] to analyze the proposed SOFC-system. It was found that the number of cells needed to generate 100 W decreases with decreasing cell voltage. Also, the number of cells decreases for decreasing single pass fuel utilization U_f. Decreasing the number of cells decreases the volume of the SOFC stack. However, efficiency was found to decrease with decreasing voltage and decreasing U_f. This reduces the operation time with a fixed 0.8 L ammonia tank and fixed power output of 100 W.

Besides the sensitivity regarding the number of cells and U_f, the amount of air required to cool the system was also investigated by Farhad et al. [23]. Increasing cell voltage and decreasing the U_f leads to a decrease in air flow. Reducing the air flow leads to a smaller size of the heat exchanger, catalytic afterburner and air blower.

Based on the sensitivity analysis, a cell voltage of 0.73 V and a U_f of 0.80 were selected by Fahrad et al. [23]. These system parameters resulted in an efficiency of 41.1% based on the LHV of ammonia. Figure 17 displays the results of an exergy analysis for the SOFC-system. The exergy efficiency, defined as the useful electricity compared to the total exergy entering the system, accounts for 35.4%. The SOFC stack has the largest contribution to the exergy losses, accounting for 26.6%.

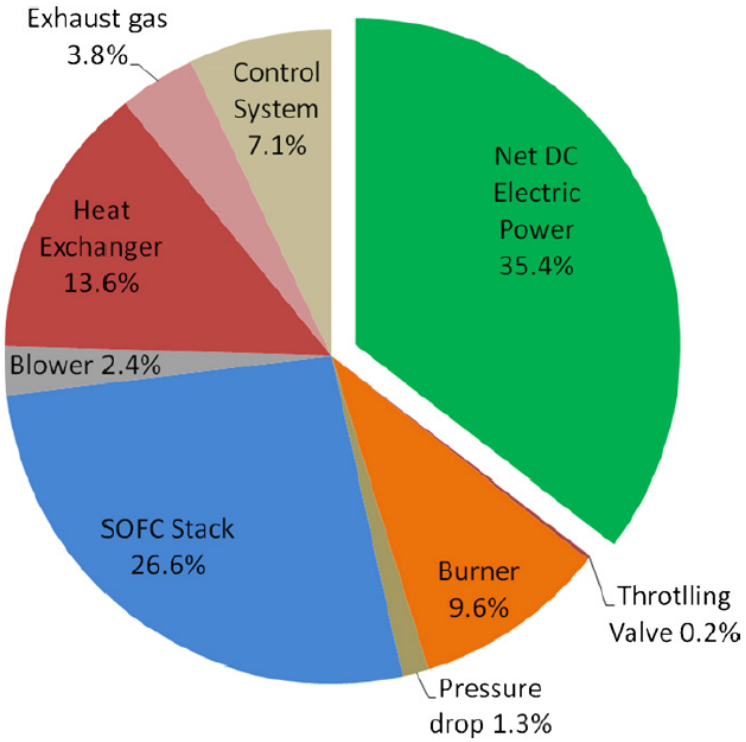

Figure 17: *Exergy distribution in the solid oxide fuel cell model by Farhad et al. [23].*

Cinti et al. [13] were the first to show the advantages of heat balancing when ammonia is used as fuel in both experiments as modelling. For the experiment, the temperature was measured at both the inlet and outlet of the anode and cathode. Three cases were studied: Pure hydrogen, hydrogen-nitrogen mixture and pure ammonia. When using ammonia, the temperature of the anode was found to be lower, owing to the effect of endothermic cracking. This effect lowers the average cell temperature and the difference in temperature between the anode and cathode. Both effects are expected to enhance the thermal stability of the SOFC stack and reduce thermal stress. Besides temperature measurements, polarization curves were obtained, which were used to develop a 0-dimensional thermodynamic SOFC-system model.

A schematic of this SOFC-system model is shown in Figure 18. Four heat exchangers were used: Two for preheating the ammonia and two for preheating the air. HE-2 and H2-3 reduce the off-gas temperature to 330 °C, which is the maximum inlet temperature of the catalytic afterburner. The maximum outlet temperature for the catalytic afterburner is 900 °C.

Inlet temperatures for the anode and cathode were set to 700 °C and outlet temperatures to 800 °C, leading to a mean operating temperature of 750 °C. Heat losses from the SOFC stack to the surroundings were modelled as 10% of the SOFC stack electrical outlet power. A total pressure loss of 100 mbar was assumed for the cathode gas line.

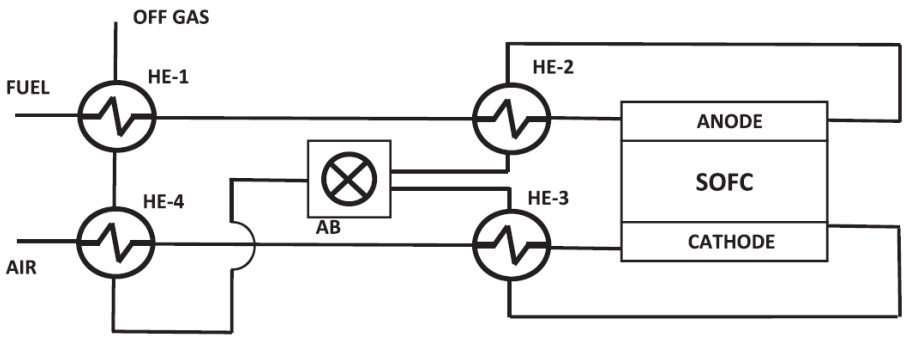

Figure 18: *Schematic of the SOFC-system model by Cinti et al. [13].*

Cinti et al. [13] found that internal endothermic cracking of ammonia reduces the required air cooling, resulting in a reduction in air power blower consumption. The system efficiency based on the lower heating value of ammonia was reported to increase by a value in the range of 3 - 5% compared to an equivalent mix of hydrogen and nitrogen [13].

2.3 Summary

Although the ambiguity regarding the performance of ammonia fueled SOFCs compared to hydrogen, its feasibility was demonstrated by various experiments performed on laboratory scale. Ammonia was shown to decompose readily into nitrogen and hydrogen at moderate temperature and low pressure. This endothermic cracking reaction has been proven to reduce the air cooling demand. Yet, the air heat exchanger remains a dominant unit operation. The voltage decay of ammonia fueled SOFCs are similar to the more widely studied hydrogen fueled SOFCs. Furthermore, despite the high operation temperature of the SOFC, NO_x formation has not been observed.

3 Methodology

In this Chapter, the methodology for modelling the ammonia fueled SOFC propulsion system will be discussed. First, modelling of the SOFC will be discussed in section 3.1. Second, in section 3.2, the SOFC will be expended to the a SOFC-system: Adding the unit operations and the electrical circuit. Also, an overview of the system parameters will be given. Section 3.3 defines the system cell efficiency, system efficiency and exergy efficiency. A summary of the chapter is given in section 3.4.

3.1 Modelling of the Solid Oxide Fuel Cell

To model the SOFC-system, mass, energy, and charge balances have to be solved. These balances could be solved by writing algorithms in e.g. Python or MATLAB. Chemical process simulators such as Cycle-Tempo and Aspen Plus may be used as an alternative. Aspen Plus is used by Proton Ventures and therefore selected as the modelling tool. Aspen Plus is used extensively in industry and academia for steady-state and dynamic simulation, process design, performance modelling and optimization.

Aspen Plus is a 0-dimensional chemical process simulator. 0-dimensional indicates that variable parameters are only calculated at the inlet and outlet based on the fixed internal parameters. In an SOFC, the oxidation reaction as in Equation 2 takes place at the anode and the reduction reaction as in Equation 3 takes place at the cathode. However, Aspen Plus does not accommodate electrochemical reactions. Therefore, the electrochemical reactions should be modelled by using the unit operations available in Aspen Plus.

The cathode will be modelled with a separator module, directing part of the oxygen form the air to the anode. This stream represents the oxygen-ion flow through the electrolyte. The anode will be composed of two modules. A RGibbs module and a REquil module. The RGibss module represents the internal cracking of ammonia, as in Equation 1, by minimizing the Gibbs free energy of the mixture. The required inputs for the RGibbs module, the reaction temperature and pressure, define the cracking conversion. The REquil module represents the HOR Equation as in Equation 4. The required input for the REquil module is the conversion of the reaction. Excel will be coupled to Aspen Plus to incorporate the electrochemical phenomena, which will be based on theoretical cell voltage calculations. Values from the widely cited paper of Aguiar et al. [26] will be used. The dimensions of the SOFC model are given in Table 5.

Table 5: *Dimensions used for the solid oxide fuel cell [26].*

Dimension	Symbol	Value	Unit
Cell length	L_{cell}	0.1	m
Cell width	W_{cell}	0.1	m
Fuel channel height	τ_{fc}	1	mm
Air channel height	τ_{ac}	1	mm
Anode thickness	τ_{a}	500	μm
Cathode thickness	τ_{c}	50	μm
Electrolyte thickness	τ_{el}	20	μm
Interconnection thickness	τ_{int}	500	μm

As mentioned, the unit operations in Aspen Plus are 0-dimensional. The inlet and outlet temperature will be defined by the maximum allowable temperature gradient over the cell and the reaction temperature in the SOFC. To avoid thermal stress, the maximum allowable temperature gradient between inlet and outlet is set at 100 °C [32]. The reaction temperature is set at 800 °C, in order to be consistent with the electrochemical phenomena in the research of Aguiar et al. [26]. Combining the maximum temperature gradient and reaction temperature results in an inlet temperature of 750 °C and an outlet temperature of 850 °C. Heaters will be included to account for the temeprature changes. The temperature characteristics of the SOFC were discussed in section 2.1.1. Figure 8 showed little difference in the outlet temperature. Although Aguiar et al. [26] used internal methane reforming instead of infernal ammonia cracking, both reactions are endothermic and result in cooling. Therefore, it is assumed to model the ammonia fueled SOFC with equal outlet temperatures for the anode and cathode.

3.2 Modelling of the Solid Oxide Fuel Cell System

3.2.1 System Configuration

The SOFC stack is fuelled by ammonia and air. Ammonia is stored as a liquid at 20 bar and ambient temperature. A valve reduces the pressure in the ammonia storage tank to the operational pressure of the SOFC stack. Also, the valve controls the ammonia feed flow rate. An air blower is used to provide the required air feed flow rate. The ammonia and air are preheated to avoid thermal stress in the SOFC stack with an anodic and cathodic heat exchanger respectively. The anode off-gas and cathode off-gas are split to achieve a recirculation r_a and r_c respectively. A cathodic and anodic blower are used to compensate pressure losses in the recirculation loops. The anode recirculation stream is mixed with the ammonia feed and the cathode recirculation stream is mixed with the air feed. The non-recirculated anode off-gas and cathode off-gas are mixed and combusted in an afterburner to consume the unreacted hydrogen. The exhaust heat is used for the anodic and cathodic heat exchanger subsequently. The air stream is much larger than the ammonia stream, because of the excess air needed to cool the SOFC stack. Therefore, the heat duty of the cathodic heat exchanger is larger than the anodic heat exchanger. By preheating the ammonia feed first, the temperature of the exhaust stream from drops only little, securing a sufficient temperature pinch for the cathodic heat exchanger. The schematic of the SOFC propulsion system is shown in Figure 19.

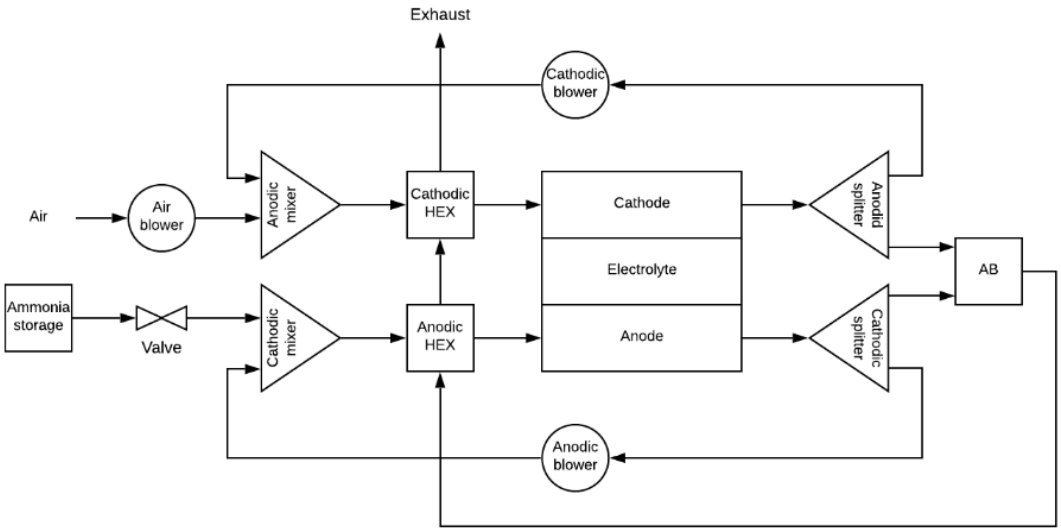

Figure 19: *Schematic of the SOFC propulsion system. HEX = heat exchanger. AB = afterburner*

3.2.2 Electrical Circuit

To propel the vessel, electricity from the SOFC stack should be converted to mechanical shaft power. This conversion is established with an electromotor.

As discussed in section 1.2, the SOFC is unpractical for transient operations. Therefore, the SOFC is operated continuously at steady-state. The power supply of the SOFC stack should be matched with the power consumption of the shaft. In contrast to the SOFC stack power, the power consumption of the vessel is variable due to its mobility. A battery module is used to match the steady-state power supply of the SOFC stack to the variable power demand of the shaft by compensating temporarily imbalances.

The SOFC stack must supply the required energy for the vessel. The vessel is in service for 8h per day with an assumed shaft power of 25 kW, resulting in a energy demand of 200 kWh. Therefore, the SOFC stack has to generate 200 kWh / 24 h = 8.33 kW of mean shaft power $\bar{P}_{shaft}$. However, due losses in the circuit, losses in the battery module and power consumption of the blowers, the stack power is larger than 8.33 kW.

When the vessel is not in service, the power of the SOFC stack is used to charge the battery module. During service, the power of the SOFC stack is directly used by the electromotor. The remaining power is supplied by the battery module. The energy storage in the battery module is unchanged after one day: All energy is generated by the SOFC stack. This is graphically shown by Figure 20.

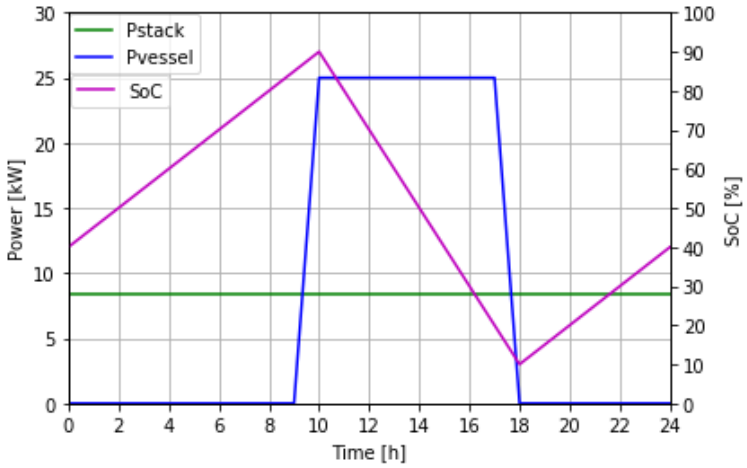

Figure 20: *Left y-axis: Power pattern solid oxide fuel cell stack and vessel. Right y-axis: State-of-Charge battery module.*

The State-of-Charge (SoC) limits of a battery are complex and depend on the rate of discharge, rate of charge, temperature, voltage, etc. Values used for the SoC limits, as seen in Figure 20, are between 10 and 90 % [33].

The electricity of the SOFC stack has two pathways to reach the electromotor: Either direct, or indirect via the battery module. For the direct pathway, direct current (DC) from the SOFC stack is converted to alternating current (AC) for the electromotor with an inverter. For the indirect pathway, the DC of the SOFC stack is matched with the DC input of the battery module with a converter. The DC from the battery module is converted to AC for the electromotor with an inverter.

The blowers to generate the air feed flow and to compensate the losses in the recirculating loops are powered by the SOFC stack as well. The blowers operate 24h a day, just as the SOFC stack. A converter matches the DC from the SOFC stack with DC for the blowers. The electricity distribution scheme during service is shown in Figure 21, whereas the electricity distribution when the vessel is not in service is shown in Figure 22.

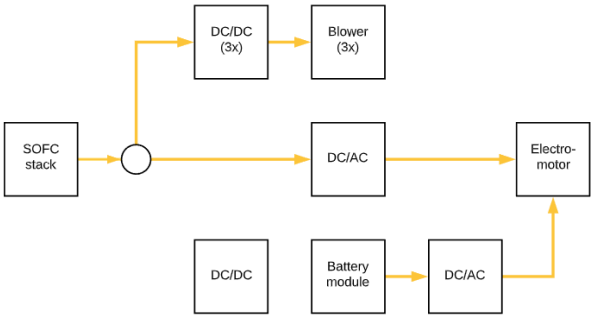

Figure 21: *Electricity distribution when the vessel is in service.*

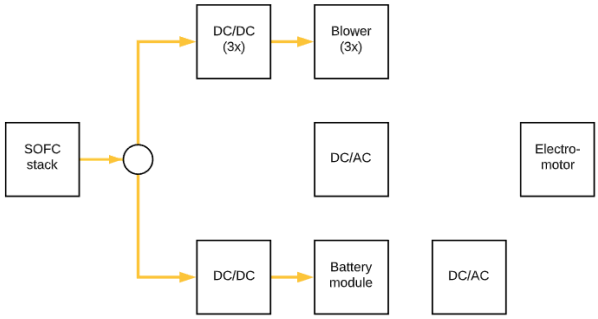

Figure 22: *Electricity distribution when the vessel is not in service.*

Each pathway has a different efficiency. The overall efficiency of the electrical circuit η_{cir} is calculated by Equation 9.

$$\eta_{cir} = \frac{1}{3} \cdot \eta_{direct} + \frac{2}{3} \cdot \eta_{indirect} \tag{9}$$

$$\eta_{direct} = \eta_{inv} \cdot \eta_{em}$$

$$\eta_{indirect} = \eta_{conv} \cdot \eta_{bm} \cdot \eta_{inv} \cdot \eta_{em}$$

where *inv* denotes the inverter, *em* denotes the electromotor, *bm* denotes the battery module and *conv* denotes the converter. The 1/3 term follows from the service time ratio: 8h/24h. The 2/3 term is follows from the time ratio when the vessel is not in service: 16h/24h.

As mentioned, the shaft power must equal 8.33 kW. This power and the power for the blowers have to be supplied by the SOFC stack. This results in a steady-state SOFC stack power calculated by Equation 10.

$$P_{stack} = \frac{P_{shaft}}{\eta_{cir}} + \frac{P_{blower,air} + P_{blower,a} + P_{blower,c}}{\eta_{blower} \cdot \eta_{conv}} \tag{10}$$

$$P_{blower} = \Delta p_{blower} \cdot \dot{V}_{blower}$$

where $\dot{V}$ is the volumetric flow rate.

Pressure drops of 90 mbar for the air blower and 30 mbar for the recirculation loops are used [13]. Efficiencies used for the components in the electrical circuit are listed in Table 6.

Table 6: *Efficiencies of the electrical components.*

Component	Efficiency [%]
Inverter	99 [34]
Electromotor	97 [35]
Converter	99 [34]
Battery module	97 [36]
Blower	75 [13]

3.2.3 System parameters

The SOFC-system contains variable and fixed parameters. A set of variable system parameters will be selected in order to conduct a sensitivity study with respect to the efficiency, weight and volume of the SOFC-system. Insight obtained from the sensitivity will be used to set the final variable system parameters.

The first parameter to study is the number of cells $\#_{cells}$ in the stack. The mean shaft power output is fixed. By changing the number of cells in the stack the power density is changed. The power density is the product of voltage and current density and can be seen as the operating point of the SOFC. Second the single-pass fuel utilization will be studied. By increasing the U_f more ammonia is used to produce electricity. The third parameter to study is the cathode off-gas recirculation rate r_c. When the cathode rericulation stream mixes with the air feed, the temperature of the mixtures increases before entering the cathodic heat exchanger. Therefore, it is expected that the size of the cathodic heat exchanger is decreased. The final parameter to study is the anode off-gas recirculation rate r_a. By recirculating the anode off-gas, the overall fuel utilization will increase. Expected is that this will increase the system efficiency.

For each variable system parameter, the value range will be set for the sensitivity analysis. As mentioned, the number of cells determines the operating point of the SOFC. Therefore, the number of cells will be varied to meet the 0.70 - 0.80 V operating range of the SOFC [17]. In practice, the U_f has a maximum value of 90 % in order to avoid voltage drop and nickel oxidation at the anode [37]. The cathode off-gas recirculation range will cover 0 % to a yet unknown limiting value. The same applies for the anode off-gas recirculation range. Table 7 gives an overview of the system parameters selected for the sensitivity study and the main fixed system parameters.

Table 7: *Sensitivity study system parameters and main fixed system parameters.*

Sensitivity study parameters	Symbol	Range
Number of cells in the stack	$\#_{cells}$	Translated to 0.70 - 0.80 V
Single pass fuel utilization	U_f	limiting value - 90 %
Cathode off-gas recirculation rate	r_c	0 % - limiting value
Anode off-gas recirculation rate	r_a	0 % - limiting value
Main fixed system paramters	**Symbol**	**Value**
Operating temperature	T_{stack}	800 °C
Inlet temperature feeds	T_i	750 °C
Outlet temperature feed	T_e	850 °C
Operating pressure	p_{stack}	1 bar
Mean shaft power	P_{shaft}	8.33 kW

3.3 Definitions

3.3.1 Efficiency

One of the objectives of the research reported in this MSc thesis is to predict the efficiency the SOFC-system fueled by sustainable synthesized ammonia. Efficiency can be defined in numerous ways. To compare different propulsion systems, the efficiency based on the LHV of the fuel is commonly used. The LHV is the enthalpy change of combustion at 25 °C and 1 bar. The efficiency based on the LHV for the SOFC-system is defined as in Equation 11.

$$\eta_{system} = \frac{P_{shaft}}{\dot{n}_{NH_3} \cdot M_{NH_3} \cdot LHV_{NH_3}} \tag{11}$$

where $\dot{n}$ is the molar flow and M is the molar mass.

The performance of the individual cells influences the system efficiency. A higher cell efficiency results in a lower ammonia consumption, thereby increasing the system efficiency. The cell efficiency is the cell power over the enthalpy of reaction in the cell as in Equation 12.

$$\eta_{cell} = \frac{P_{cell}}{\dot{n}_{H_2,cell} \cdot \Delta h_{HOR}} \tag{12}$$

where Δ_{HOR} is the enthalpy of reaction as in Equation 4 based on the reaction temperature and pressure of the cell.

3.3.2 Exergy

To analyze the energy potential of a system, an exergy analysis is carried out. An exergy analysis identifies the exergy losses in a system. Exergy is the maximum theoretical work that can be obtained in a reversible system when using the environment as a reservoir for heat and matter.

Specific exergy of a stream e is the summation of thermal-mechanical exergy and chemical exergy. The specific thermo-mechanical exergy is calculated by Equation 13.

$$e_{tm} = (h - h_o) - T_o \cdot (s - s_o) \tag{13}$$

where subscript tm denotes thermo-mechnaical, subscript o denotes standard conditions and s is the specific entropy.

Just like thermo-mechanical exergy, chemical exergy is dependent on temperature and pressure, as well as composition. Specific chemical exergy e_{ch} is calculated by Equation 14.

$$e_{ch} = e_{ch,o} + R \cdot T \cdot \ln(a_j) \tag{14}$$

where $e_{ch,o}$ is the standard specific chemical exergy of a pure component and a_j is the activity of species j.

The activity is given by Equation 68 in Appendix A. For ideal gas mixtures, the fugacity coefficient equals 1. Using Raoult's law for the pressure relation, the activity is written as in Equation 15.

$$a_j = y_J \frac{p}{p_o} \tag{15}$$

where y_j is the molar fraction and p_o is the standard pressure of 1 bar.

The standard chemical exergy of the substances applicable for the SOFC-system are given in Table 8.

Table 8: *Standard chemical exergy of the substances applicable for the SOFC-system [38].*

Substance	$e_{ch,o}$ $[\frac{kJ}{mol}]$
NH_3	337.9
H_2	236.1
N_2	0.72
O_2	3.97
H_2O	9.49

With the chemical exergy of a stream, the exergy balance for an open system can be compiled as in Equation 16.

$$\frac{d(e \cdot n)}{dt} = \sum e_i \cdot \dot{n}_i - \sum e_e \cdot \dot{n}_e + \dot{Q} \cdot (1 - \frac{T_o}{T_b}) - \dot{W} - \dot{e}_d \cdot n \tag{16}$$

where n is the number of moles, t is time, subscript i denotes inlet, subscript e denotes outlet, $\dot{Q}$ is the heat transfer across the boundary of the system, subscript b denotes the boundary of the system, $\dot{W}$ is the work per time unit, and subscript d denotes destruction.

Equation 16 can be used to calculate the exergy destruction of a control volume. Exergy destruction should be minimized the maximize the energy potential. The exergy efficiency is defined as the power output over the exergy entering the SOFC-system as in Equation 17.

$$\eta_{exergy} = \frac{P_{shaft}}{(e_{NH_3} \cdot \dot{n}_{NH_3} + e_{air} \cdot \dot{n}_{air})} \tag{17}$$

3.4 Summary

Process simulation has been selected as main modelling tool for the case study. The following variable system parameters have been selected for the sensitivity study:

- Number of cells in the stack
- Single-pass fuel utilization
- Cathode off-gas recirculation rate
- Anode off-gas recirculation rate

A reaction temperature of 800 °C and reaction of 1 bar was selected. A battery module is used to compensate for temporarily imbalances between power supply and power demand. Two efficiency expressions have been defined for interpretation of the results: A system efficiency based on the LHV of ammonia and an cell efficiency based on the enthalpy of reaction of the HOR.

4 Modelling of the Solid Oxide Fuel Cell Propulsion System

In the chapter 3, the methodology to model the SOFC-system was discussed. This chapter compiles the SOFC-system model. Section 4.1 start with the SOFC model: the unit operations, energy balance and charge balance. Section 4.2 continues on the complete model of the SOFC-system, including the iterative solving method applied to solve the energy and charge balance. A summary is given in section 4.3.

4.1 Modelling of the Solid Oxide Fuel Cell

4.1.1 Unit Operations

As discussed in section 3.1 the SOFC model will be compiled of a separator, a RGibbs reactor and a REquil module. The separator, labelled as cathode, simulates the cathode of the SOFC. Part of the oxygen from the air feed will be separated and directed to the anode. This represents the oxygen-ion flow through the electrolyte. The RGibbs module, labelled as cracker, represents the internal cracking of ammonia. In the RGibbs module, the ammonia conversion takes places to reach equilibrium at the reaction temperature and pressure, as governed by minimizing the Gibbs free energy of the mixture. The cracker operates isothermal. The REquil module, labelled as HOR, represents the HOR, which is also isothermal in the model. The energy required for isothermal operation of the cracker and HOR module is calculated by the process simulator. Figure 23 displays the simulation model developed for the SOFC.

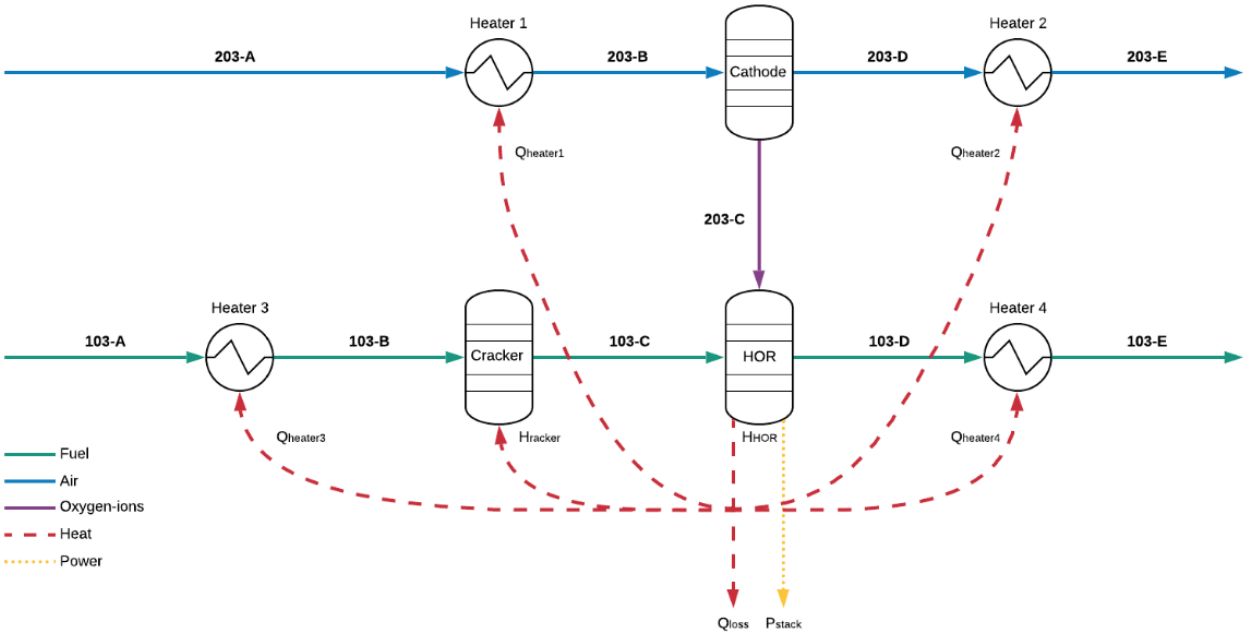

Figure 23: *Solid oxide fuel cell model.*

Heaters are implemented to obtain the desired values for the temperatures in the model. The cathode inlet air of 750 °C is heated to the reaction temperature of 800 °C by Heater 1. The air passes the cathode, after which the stream is heated to the assumed outlet temperature of 850 °C by Heater 2. The ammonia feed stream is heated to the reaction temperature by Heater 3, passes the cracker and HOR, after which the stream is heated to the outlet temperature by Heater 4.

The anode produces energy because of the exothermic HOR. This energy is divided into SOFC stack power and heat production. The efficiency of the SOFC determines the amount of SOFC stack power. The heat is directed to all unit operations in the model that demand heat to close the energy balance: The cracker and the four heaters.

4.1.2 Energy Balance

The energy balance for an open system is given in Equation 18.

$$\frac{dE}{dt} = \dot{Q} - \dot{W} + \sum h_i \cdot \dot{m}_i - \sum h_e \cdot \dot{m}_e + h_{source} \cdot \dot{n} \tag{18}$$

where E is the energy and h_{source} is the specific enthalpy of reaction from a source.

The energy balance of the SOFC model, derived from Equation 18, is given by Equation 19. The derivation can be found in Appendix E.

$$P_{stack} = -h_{HOR} \cdot \dot{n}_{HOR} - h_{cracker} \cdot \dot{n}_{cracker} - \dot{Q}_{air} - \dot{Q}_{NH_3} - \dot{Q}_{loss} \tag{19}$$
$$\dot{Q}_{air} = \dot{Q}_{heater1} + \dot{Q}_{heater2}$$
$$\dot{Q}_{NH_3} = \dot{Q}_{heater3} + \dot{Q}_{heater4}$$

where h_{HOR} is the specific enthalpy of reaction as in Equation 4 but at the reaction conditions, $h_{cracker}$ is the enthalpy of reaction as in Equation 1 but at the reaction conditions, $\dot{Q}_{air}$ is the heat required to heat up the cathode gas, $\dot{Q}_{ammonia}$ is the heat required to heat up the anode gas and $\dot{Q}_{loss}$ are the heat losses to the environment.

Heat Losses

Heat losses from the SOFC stack to the surroundings can be significant. There are three mechanisms for heat transfer: conduction, radiation and convection. Conduction applies for the bottom of the SOFC stack, which is in closed contact to the ship. It is assumed that this face is properly insulated, neglecting heat losses by conduction. It is assumed that the outside of the SOFC is properly coated to minimize radiation losses by minimizing the emissivity coefficient. Also, radiation is minimal due to the relatively low outside temperature of the SOFC stack compared to the surroundings. Therefore, only convection is responsible for heat loss.

It is assumed that the SOFC stack is located under the deck of the vessel. This leads to heat loss by natural convection only. Natural convection for vertical walls and horizontal walls is different, as in Equation 20.

$$\dot{Q}_{loss} = \dot{Q}_{top} + \dot{Q}_{sides} \tag{20}$$

The heat losses from the top are given by Equation 21 and heat losses from the side walls are given by Equation 22.

$$\dot{Q}_{top} = \bar{\lambda}_{top} \cdot (L_{stack} \cdot W_{stack}) \cdot (T_{wall} - T_{amb}) \tag{21}$$

$$\dot{Q}_{sides} = \bar{\lambda}_{side} \cdot (2 \cdot W_{stack} \cdot H_{stack} + 2 \cdot L_{stack} \cdot H_{stack}) \cdot (T_{wall} - T_{amb}) \tag{22}$$

where λ is the heat transfer coefficient, H is height of the stack and subscript $_{amb}$ denotes ambient. For safety reasons, an upper limit of 50 °C for the wall temperature T_{wall} is selected, achieved by proper insulation of the SOFC stack.

The heat transfer coefficient is related to the dimensionless Nusselt number Nu, as in Equation 23.

$$\lambda = Nu \cdot \frac{\kappa}{L} \tag{23}$$

where κ is the thermal conductivity and L is the characteristic length.

For natural convection, correlations for the Nusselt number are based on the Rayleigh number. For the top wall, the correlation of Churchill et al. [39] is used as in Equation 93 in Appendix E. For the side walls, the correlation of McAdams [40] is used as in Equation 94 in Appendix E.

The SOFC stack operates at an assumed uniform temperature of 800 °C. In order to obtain the desired wall temperature, insulation material is applied. Heat loss by natural convection equals heat conduction through the insulation material. This leads to the calculation of the insulation thickness τ_{in} as in Equation 24.

$$\tau_{in} = \frac{\dot{Q}}{\kappa_{gw} \cdot (T_{stack} - T_{wall})} \tag{24}$$

where subscript gw denotes the selected insulation material glass wool with a thermal conductivity of 0.04 W/m/K [41].

When all cells are placed after each other, the length of the SOFC stack is large compared to the SOFC stack width and SOFC stack height. Heat losses and insulation material can be minimized by changing the stacking of the cells into a cube. The width, height and length of the SOFC stack are given by Equations 25 until 27 respectively.

$$W_{stack} = W_{cell} \cdot \#_{cells,width} + 2 \cdot \tau_{in,top} \tag{25}$$

$$H_{stack} = L_{cell} \cdot \#_{cells,height} + 2 \cdot \tau_{in,side} \tag{26}$$

$$L_{stack} = \tau_{cell} \cdot \#_{cells,length} + \tau_{int} + 2 \cdot \tau_{in,side} \tag{27}$$

where τ_{cell} is the cell thickness consisting of the air channel, cathode, electrolyte, anode, fuel channel and interconnection.

4.1.3 Charge Balance

A polarization curve is a plot of the current density i versus system potential ϕ. The polarization curve is described by the reversible cell voltage ϕ_{rev} minus the voltage losses. The voltage losses consist of:

- Activation losses - ϕ_{act}
- Fuel crossover and internal current losses
- Ohmic losses - ϕ_{ohm}
- Diffusion losses - ϕ_{diff}

where subscript act denotes activation and subscript $diff$ denotes diffusion.

Fuel crossover is diffusion of fuel through the electrolyte from the anode to the cathode without being electrochemically reacted. Internal currents are electrons travelling through the electrolyte. Fuel crossover and internal currents are equivalent: one hydrogen molecule crossing from the anode to the cathode results in a loss of two electrons, whereas the crossing of two electrons from the cathode to the anode results in a loss of one hydrogen molecule. As discussed in 1.2, sealing is an issue in SOFCs, leading to leakages. Therefore, fuel crossover can be significant. However, in literature this loss mechanism is omitted [26].

Equation 28 [42] represents the general form of the polarization curve, where fuel crossover and internal currents are not taken into account.

$$\phi_{cell} = \phi_{rev} - \phi_{act,c} - \phi_{act,a} - \phi_{ohm} - \phi_{diff,c} - \phi_{diff,a} \tag{28}$$

Reversible Cell Voltage

The reversible cell voltage, is the cell voltage at electrochemical equilibrium. E.g. the forward and backward reactions as in Equations 2 and 3 are in equilibrium. The reversible cell voltage is described by the Nernst Equation 67 [42], discussed in Appendix A. The Nernst Equation includes the activity of the species, which depends on the fugacity and the partial pressure. When ideal gasses are assumed the fugacity coefficient equals 1. Ideal gasses are assumed for low pressures and high temperatures, as in the case of the SOFC. The partial pressure is the product of the molar fraction and the absolute pressure. Implementing this into the Nernst Equation 67 in Appendix A results into an expression for the equilibrium potential as given by Equation 29.

$$\phi_{rev} = \phi^{\circ}_{rev} - \frac{R \cdot T_{stack}}{\mu \cdot F} \ln(\frac{y_{H_2O}}{y_{H_2} \cdot y_{O_2}^{0.5}}) + \frac{R \cdot T_{stack}}{2 \cdot \mu \cdot F} \ln(\frac{p_{stack}}{p_o}) \tag{29}$$

where ϕ°_{rev} is the standard reversible cell voltage at equilibrium, $\mu = 2$ is the number of electrons per mole hydrogen, F is Faraday's constant and p_o is the standard pressure of 1 bar.

Equation 29 shows the influence of the molar concentrations on the reversible cell voltage. The lowest concentration along the electrode determines the reversible cell voltage. Because the 0-dimensional model, the concentration at the outlet is used. The reversible cell voltage can also be calculated with the difference in specific Gibbs free energy Δg, as in Equation 30 [42]. The derivation can be found in Appendix A. This approach avoids using the outlet concentrations of the species.

$$\phi_{rev} = -\frac{\Delta g}{\mu \cdot F} \tag{30}$$

Activation Losses

For the activation losses, the Butler - Erday-Grúz - Volmer (BE-GV) Equation 31 [42], derived in Appendix A, is used.

$$i = i_o[exp(\frac{\alpha_a \cdot F}{R \cdot T_{stack}} \ \phi_{act}) - exp(-\frac{\alpha_c \cdot F}{R \cdot T_{stack}} \ \phi_{act})] \tag{31}$$

where i_o is the exchange current density and α is the transfer coefficient.

The main assumptions employed in the BE-GV Equation are:

1. The backward and the forward half-cell reaction occur at the same electrode
2. Charge transfer is across a two-phase interface
3. Charge transfer is limited by a single rate-determining step

The first assumption is met when both the anodic and cathodic half-cell reactions are taken into account. This results in an overpotential on the anodic and the cathode. According to Kendall et al. [43], SOFCs tend to comply with assumptions 2 and 3. Figure 24 gives a schematic representation of the BE-GV Equation 31.

The transfer coefficient is dependent on the symmetry factor, which has a typical value of 0.5. This makes the BE-GV Equation 31 symmetric and allows it to be rewritten explicitly for the activation losses as given by Equation 32. The derivation can be found in Appendix D.

$$\phi_{act} = \frac{R \cdot T_{stack}}{\alpha \cdot F} \sinh^{-1}(\frac{i}{2i_o}) \tag{32}$$

The exchange current density is dependent on the activity of the species and intrinsic electrocatalytic properties of the electrode material. The exchange current density is computed by Equation 33 [26].

$$\bar{i}_{o,j} = \frac{R \cdot T_{stack}}{\mu \cdot F} \cdot b_j \exp(-\frac{E_{act,j}}{R \cdot T_{stack}}) \tag{33}$$

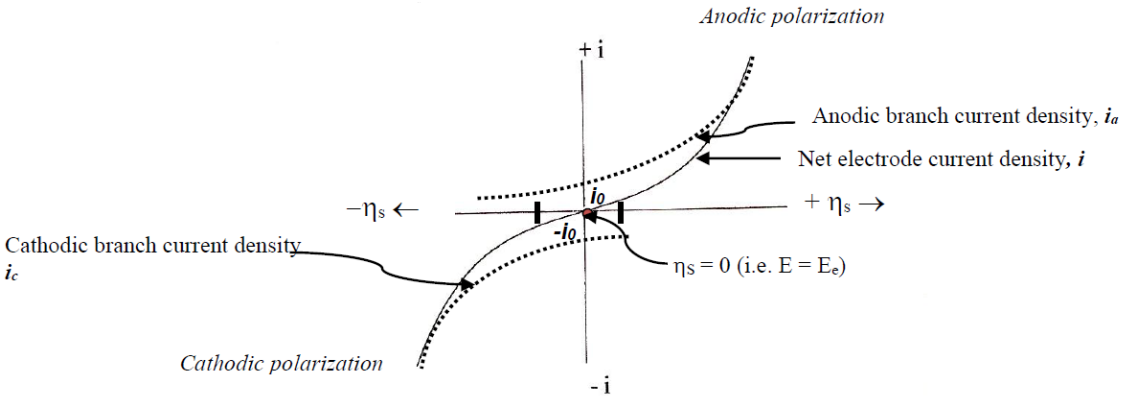

Figure 24: *Schematic representation of the Butler - Erday-Grúz - Vomer equation [42].*

Table 9: *Pre-exponential factor and activation energy [26].*

	Anode	Cathode
b $[\Omega^{-1}m^{-2}]$	6.54E11	2.35E11
E [kJ/mol]	140	137

where b_j is the pre-exponential factor and $E_{act,j}$ is the activation energy. The values are given in Table 9.

Ohmic losses

Ohmic losses in the SOFC are more significant than in other types of fuel cells [15]. Ohmic losses consist of losses caused by electron transport through the external circuit and by ion transport in the PEN structure. The latter dominates the ohmic losses. Ohmic losses are given by Equation 34 [42], derived in Appendix A.

$$\phi_{ohm} = i \cdot \epsilon_{cell} \tag{34}$$

where ϵ is the ohmic resistance.

The ohmic resistance of the cell consists of the resistances of the anode, electrolyte and cathode in series as in Equation 35. The resistance of the external circuit is small compared to the PEN structure [15] and is therefore neglected.

$$\epsilon_{cell} = \epsilon_a + \epsilon_{el} + \epsilon_c = \frac{\tau_a}{\sigma_a} + \frac{\tau_{el}}{\sigma_{el}} + \frac{\tau_c}{\sigma_c} \tag{35}$$

where σ is the conductivity of which the values are given in Table 10. The conductivity of the ceramic electrolyte is strongly dependend on temperature.

Table 10: *Conductivity of the anode, electrolyte and cathode [26].*

	Anode	Electrolyte	Cathode
σ $[\Omega^{-1}m^{-1}]$	80E3	33.4E3 exp $\frac{-10.3E-3}{T_{stack}}$	8.4E3

Diffusion Losses

When hydrogen and oxygen react at the anode and cathode interface respectively, their local molar concentration decreases due to diffusion resistance from the bulk to the interface. This local concentration decrease leads to a reduced electrode potential. Figure 25 gives a schematic of the concentration profiles.

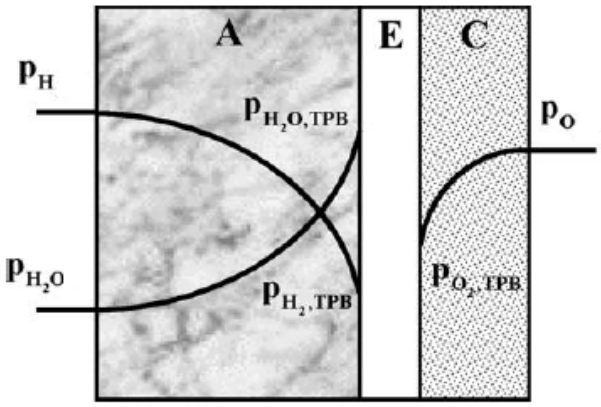

Figure 25: *Schematic concentration profile [26]. TPB = Triple Phase Boundary.*

For the diffusion losses, Equation 36 [42], derived in Appendix A, is used.

$$\phi_{diff} = -\frac{R \cdot T}{\mu \cdot F} \sum S_j \ln(\frac{a_{TPB,j}}{a_j}) \tag{36}$$

where S is the stoichiometric coefficient and subscript TPB denotes the triple phase boundary.

Equation 36 is applied to both the cathode and anode. Assuming ideal gasses and using Raoult's law for the partial pressure relation results in Equation 37 and 38 for the cathode and anode respectively.

$$\phi_{diff,c} = \frac{R \cdot T_{stack}}{2\mu \cdot F} \ln(\frac{y_{TPB,O_2}}{y_{O_2}}) \tag{37}$$

$$\phi_{diff,a} = \frac{R \cdot T_{stack}}{\mu \cdot F} \ln(\frac{y_{TPB,H_2} \cdot y_{H_2O}}{y_{H_2} \cdot y_{TPB,H_2O}}) \tag{38}$$

The molar fractions at the surface are calculated with Equations 39 untill 41 [26].

$$y_{TPB,O_2} = y_{O_2} \exp(\frac{R \cdot T_{stack} \cdot \tau_c}{2\mu \cdot F \cdot D_c \cdot p_{stack}} \ i) \tag{39}$$

$$y_{TPB,H_2} = y_{H_2} - \frac{R \cdot T_{stack} \cdot \tau_a}{\mu \cdot F \cdot D_a \cdot p_{stack}} \ i \tag{40}$$

$$y_{TPB,H_2O} = y_{H_2O} + \frac{R \cdot T_{stack} \cdot \tau_a}{\mu \cdot F \cdot D_a \cdot p_{stack}} \ i \tag{41}$$

where D is the molecular diffusion coefficient.

The molecular diffusion coefficient consist of bulk diffusion and Knudsen diffusion. Bulk diffusion is molecule-molecule interaction. When the free path length becomes too small, molecule-wall interactions become important and are known as Knudsen diffusion. The molecular diffusion coefficient depends on the porosity and tortuosity of the electrode material and therefore depends on the design and materials of the SOFC. Constant assumed diffusion coefficients of 3.66E-5 $\frac{m^2}{s}$ and 1.37E-5 $\frac{m^2}{s}$ for the anode and cathode respectively are used [26].

Polarization Curve

A plot of the polarization curve for the SOFC is provided in Figure 26. The power density of a cell is the product of the voltage and current density and is shown in Figure 27. Also included is the efficiency of the cell based on the reversible cell voltage, which is 100% at zero current density.

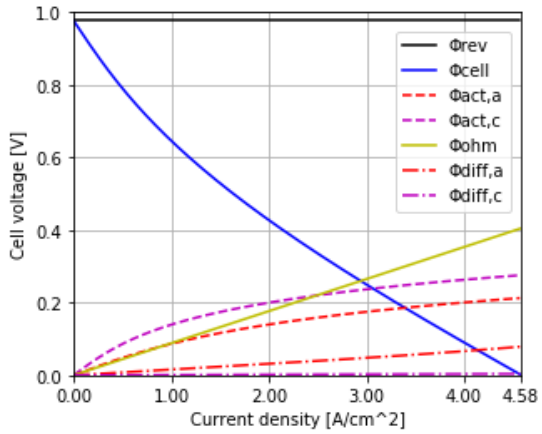

Figure 26: *Polarization curve solid oxide fuel cell.*

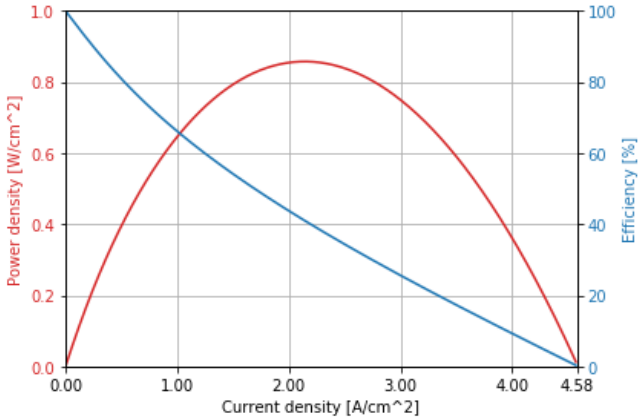

Figure 27: *Power density and efficiency as function of current density.*

4.2 Modelling of the Solid Oxide Fuel Cell Propulsion System

4.2.1 Building Blocks

Figure 28 displays the complete SOFC-system. Ammonia is stored as a liquid at 20 bar and ambient temperature. The valve reduces the pressure to the operation pressure of the SOFC stack and controls the feed flow rate. The ammonia is mixed with the anode off-gas recirculation stream and preheated to 750 °C before entering the SOFC stack in the anodic heat exchanger. The air feed flow rate is established by the air blower. The air feed is mixed with the cathode off-gas recirculation stream and preheated to 750 °C in the cathodic heat exchanger. The non-recirculated streams are mixed and combusted in the afterburner. The exhaust heat is used in the anodic and cathodic heat exchanger respectively. The produced SOFC stack power is used to supply the blowers, the remaining power is guided through the electrical circuit and converted to mechanical shaft power in the electromotor. The *Solid oxide fuel cell stack* block contains the SOFC model as in Figure 23. For the weight and volume of the SOFC-system, the main components are investigated: ammonia storage system, anodic heat exchanger, cathodic heat exchanger, SOFC stack and battery module.

Storage Tank

Ammonia is stored as a liquid at 20 bar and ambient temperature. Due to the elevated pressure, a spherical steel ammonia storage tank is used. The storage in terms of weight m and volume V consists of the ammonia fuel and steel wall. The daily ammonia volume is calculated by Equation 42.

$$V_{NH_3} = \frac{m_{NH_3}}{\rho_{NH_3}} = \frac{\dot{n}_{NH_3} \cdot M_{NH_3} \cdot 24h}{\rho_{NH_3}} \tag{42}$$

where ρ_{NH_3} is the density of liquid ammonia.

The thickness of the spherical steel wall to withstand the pressure is calculated by Equation 43.

$$\tau_{wall} = \frac{FoS \cdot p_{storage,max} \cdot d_{inner}}{\psi_{steel}} \tag{43}$$

where d_{inner} is the inner diameter of the spherical tank and ψ_{steel} is yield strength of steel with a value of 310 MPa [44]. On hot days the ambient temperature increases, leading to an increase in storage pressure. A maximum ambient temperature of 45 °C is taken, at which ammonia is liquid at 17.8 bar. The factor-of-safety (FoS) range for pressurized vessels is 3.5 - 6 [45], a value of 5 is used.

The wall thickness is added to the inner diameter of the tank (Equation 99 Appendix E) to calculate the total storage volume (Equation 100 Appendix E). The weight of the steel wall (Equation 101 Appendix E) is added to the weight of the ammonia to obtain the total weight of the storage.

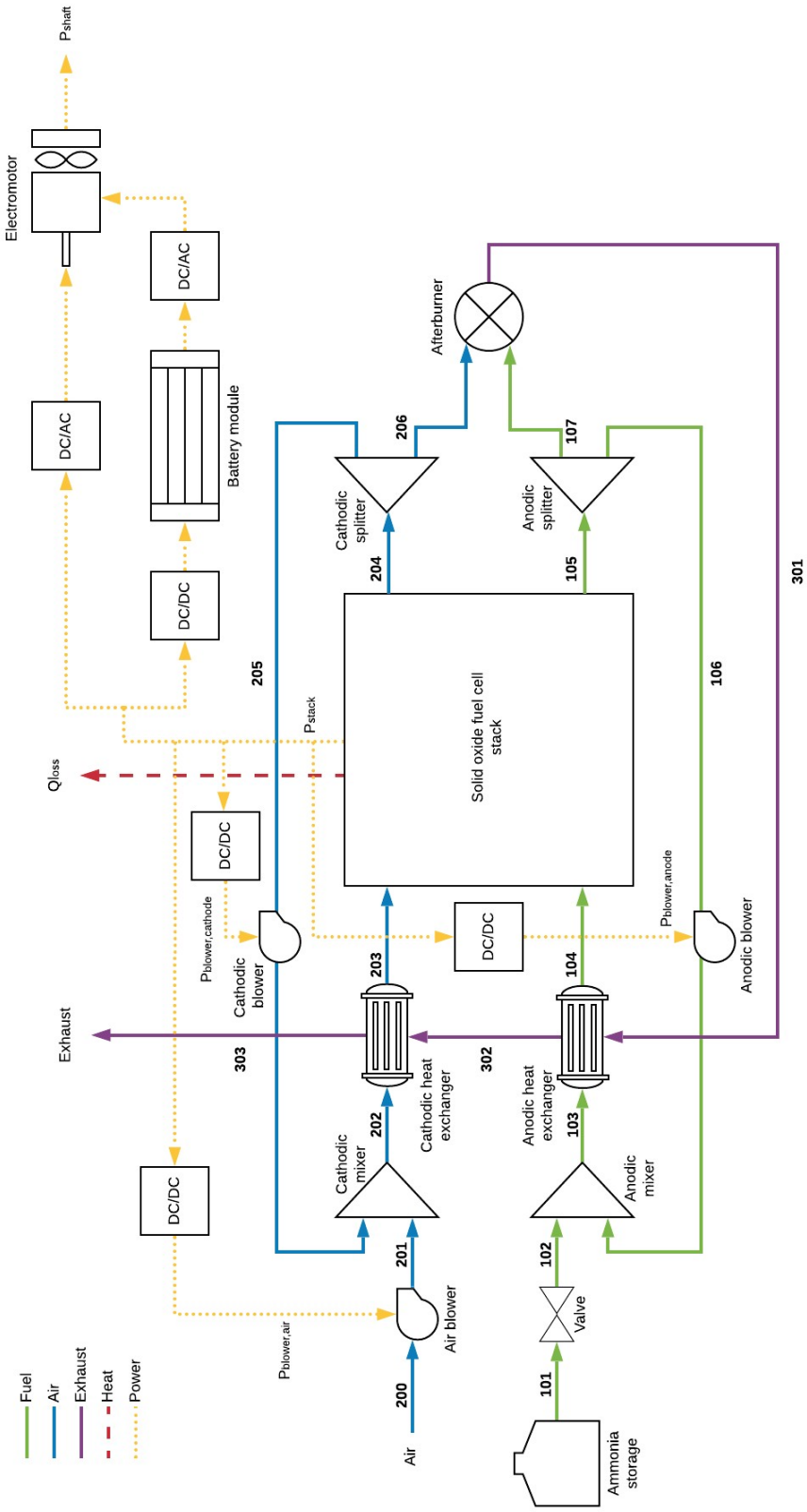

Figure 28: *Solid oxide fuel cell system model.*

Heat Exchangers

The heat exchanger need to preheat stream 202 and 103 to 750 °C. The air stream is much larger than the ammonia stream, because of the excess air needed to cool the SOFC stack. Therefore, the heat duty of the cathodic heat exchanger is larger than the anodic heat exchanger. By preheating the ammonia feed first, the temperature of the exhaust stream from the afterburner drops only little, securing a sufficient temperature pinch for the cathodic heat exchanger. In order to calculate the weight and volume of the heat exchangers, the required surface area A is calculated by Equation 44.

$$A = \frac{\dot{Q}_{duty}}{\lambda \cdot LMTD} \tag{44}$$
$$LMTD = \frac{(T1 - t2) - (T2 - t1)}{ln(\frac{T1-t2}{T2-t1})}$$

where LMTD is the logarithmic mean temperature difference, T1 is the hot side inlet temperature, T2 is the hot side outlet temperature, t1 is the cold side inlet temperature and t2 is the cold side outlet temperature.

The heat duty and heat transfer coefficient are calculated by the process simulator. Dimensions for the tube inner diameter, tube outer diameter and tube pitch from Towler et al. [46] are used. The length of the anodic and cathodic heat exchanger are selected by the process simulator. Table 11 gives an overview of the used heat exchanger parameters.

Dimension	Value	Unit
$d_{tube,inner}$	0.0191 [46]	m
$d_{tube,outer}$	0.0238 [46]	m
L_{pitch}	0.0298 [46]	m
$K1$	0.319 [46]	-
$n1$	2.142 [46]	-
L_a	100	cm
L_c	300	cm
λ_a	2.3	$W/m^2/K$
λ_c	8.8	$W/m^2/K$

Table 11: *Parameters anodic and cathodic heat exchanger.*

The required number of tubes to obtain the heat transfer surface area is calculated by Equation 102. With the number of tubes the bundle diameter and outer diameter of the shell are calculated by Equation 103 and 104 respectively. With the dimensions, the weight and volume of the heat exchanger are calculated by Equation 105 and 106 respectively. Al Equations can be found in Appendix E. Due to the high temperature, incoloy 625 alloy with a density of 8440 kg/m^3 is used as heat exchanger material [47].

Solid Oxide Fuel Cell Stack

The volume of the SOFC stack is calculated by Equation 45 and follows from the width, height and length of the SOFC stack as in Equations 25, 26 and 27 respectively.

$$V_{SOFC} = W_{SOFC} \cdot H_{SOFC} \cdot L_{SOFC} \tag{45}$$

The weight of the SOFC stack is calculated by Equation 46 and is composed of the weight of its components: insulation material, PEN structure, interconnection material. These individual weights are calculated in Equation 107, 108 and Equation 109 in Appendix E respectively.

$$m_{stack} = m_{gw} + m_{PEN} + m_{int} \tag{46}$$

A density of 25 kg/m^3 for glass wool [48], 5600 kg/m^3 for the PEN structure [26] and 8440 kg/m^3 for the incoloy 625 interconnection are used [47].

Splitters
The anode and cathode off-gas streams are recirculated according to Equation 47 and 48 respectively.

$$r_a = \frac{\dot{m}_{106}}{\dot{m}_{105}} \tag{47}$$

$$r_c = \frac{\dot{m}_{205}}{\dot{m}_{204}} \tag{48}$$

where the numbers indicate the streams according to Figure 28.

Battery module
The required capacity of the battery module is calculated according to Equation 49. A gravimetric energy density of 212 Wh/kg and a volumetric energy density of 344 Wh/L are used [36] to calculate the weight and volume of the battery module.

$$E_{bm} = \frac{P_{stack} \cdot \eta_{con} \cdot \eta_{bm}^{0.5} \cdot 16\ h}{0.8} \tag{49}$$

where subscript $_{bm}$ denotes battery module and the 0.8 is related to the maximum allowable SoC.

Exergy Losses
The exergy loss of each component is calculated by using the exergy balance in Equation 16, resulting in Equations 50 until 58. The storage tank and splitters do not have exergy destruction.

$$e_{loss,valve} = e_{101} - e_{102} \tag{50}$$

$$e_{loss,mixer,a} = e_{102} + e_{106} - e_{103} \tag{51}$$

$$e_{loss,hex,a} = e_{103} + e_{301} - e_{104} - e_{302} \tag{52}$$

$$e_{loss,blower} = P_{blower} \tag{53}$$

$$e_{loss,mixer,c} = e_{201} + e_{205} - e_{202} \tag{54}$$

$$e_{loss,hex,c} = e_{202} + e_{302} - e_{203} - e_{303} \tag{55}$$

$$e_{loss,stack} = e_{104} + e_{203} - e_{105} - e_{204} - P_{stack} + \dot{Q}_{loss} \cdot (1 - \frac{T_{amb}}{T_{wall}}) \tag{56}$$

$$e_{loss,afterburner} = e_{107} + e_{206} - e_{301} \tag{57}$$

$$e_{loss,circuit} = P_{stack} \cdot (1 - \eta_{cir}) \tag{58}$$

where subscript *hex* denotes heat exchanger and the numbers indicate the streams as in Figure 28.

4.2.2 Coupling of the Energy and Charge Balance

The desired shaft power is fixed and the ammonia and air feed flow rate need to be calculated. Because the polarization curve is an implicit function, an iterative method is used to solve the model. An initial guess for the ammonia feed flow rate is made. The ammonia passes the cracker and an equilibrium is formed based on the reaction temperature and pressure. With the hydrogen flow rate and the fuel utilization U_f the flow rate of oxygen-ions is calculated by Equation 59.

$$\dot{n}_{O^{2-}} = U_f \cdot \dot{n}_{H_2} \tag{59}$$

Using Faraday's law [42], the current density is calculated by Equation 60.

$$i = \frac{\dot{n}_{O^{2-}} \cdot \mu \cdot F}{\#_{cells} \cdot A_{cell}} \tag{60}$$

With the current density, the cell voltage is calculated by Equation 28. The cells are stacked in series. Therefore the current is equal in all cells and the SOFC stack voltage is sum of the voltage of the cells. The product of the SOFC stack voltage and current gives the electrical SOFC stack power output as in Equation 61.

$$P_{stack} = \phi_{stack} \cdot I = (\phi_{cell} \cdot \#_{cells}) \cdot (i \cdot A_{cell}) \tag{61}$$

where I represents the current.

The SOFC stack power is used in the energy balance Equation 19. The only remaining unknown left is the cooling requirement $\dot{Q}_{air}$. Rearranging Equation 19 for the cooling requirement leads to Equation 62.

$$\dot{Q}_{air} = -H_{HOR} - H_{cracker} - \dot{Q}_{NH_3} - \dot{Q}_{loss} - P_{stack} \tag{62}$$

The air feed flow rate is iterated until Equation 62 is satisfied.

With the energy and charge balance satisfied, the SOFC stack power as calculated by Equation 61 must be equal to the desired SOFC stack power calculated by Equation 10. When these values are not equal, the ammonia feed flow rate is changed and the iteration starts again. The steps are repeated until the desired SOFC stack power is reached. The iteration scheme is shown in Figure 29.

4.3 Summary

This chapter discusses the simulation model compiled for the SOFC-system. The model employs a iterative method to solve the coupled energy and charge balance. The model solves the charge balance of the SOFC stack using theoretical equations for the activation losses, ohmic losses and diffusion losses. The resulting SOFC stack power is used to calculate the cooling demand, which, in turn, establishes the required air feed flow. This chapter also discusses methods used to determine the weight and volume of the main components of the SOFC-system and the procedure for determination of the exergy losses from each component.

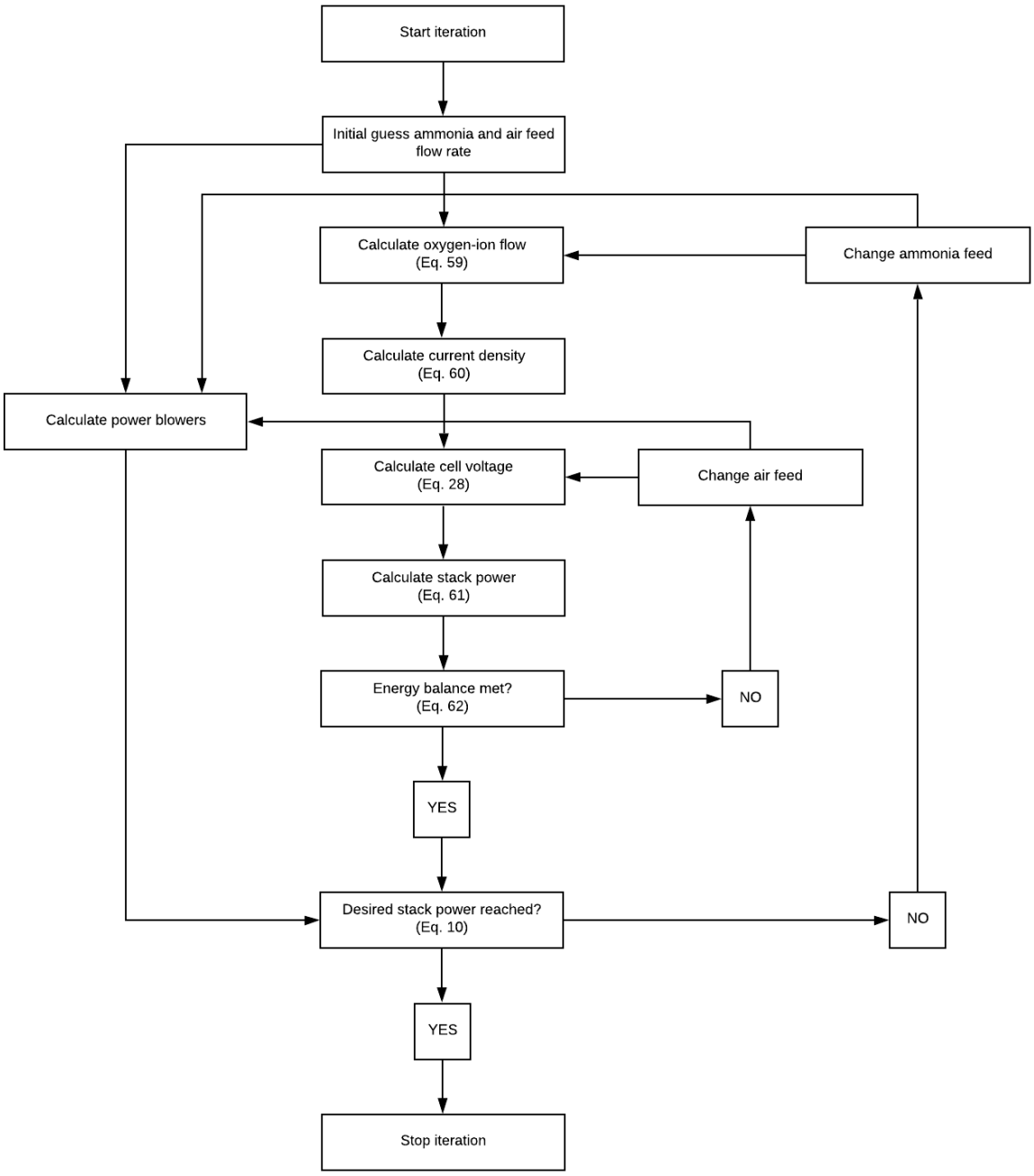

Figure 29: *Iteration scheme to calculate the desired SOFC stack power.*

5 Results & Discussion

This chapter starts with the characteristics of the SOFC-system based on the initial set sensitivity study parameters in section 5.1. Section 5.2 discusses the sensitivity analysis with the model as described in chapter 4. Section 5.3 selects the final SOFC-system sensitivity parameters with the insights obtained. A summary of the chapter is given in section 5.4.

5.1 Initial Solid Oxide Fuel Cell System

The number of cells is initially set at 210 cells to obtain a working voltage of approximately 0.75 V. Which is the mean in the operating voltage range for the SOFC as seen in Table 3. The single-pass fuel utilization is set at 80 %, which is a common selected value [23]. The r_c and r_a are set to 0 %. The system's efficiency, equipment weight and equipment volume following from the initial SOFC-system parameters are shown in Table 12

Table 12: *System efficiency, weight of the equipment and volume of the equipment for the initial solid-oxide fuel cell system.*

System efficiency		49.1 %
Weight	Storage	157 kg
	Stack	63 kg
	Battery module	657 kg
	Cathodic heat exchanger	460 kg
	Anodic heat exchanger	102 kg
	System	1439 kg
Volume	Storage	123 L
	Stack	463 L
	Battery module	406 L
	Cathodic heat exchanger	267 L
	Anodic heat exchanger	58 L
	System	1317 L

The weight and volume of the battery module account for 45.7 % and 30.9 % respectively compared to the total SOFC-system weight and volume. Changing the SOFC-system parameters has no effect on the weight and volume of the battery module, as the battery module properties only depend on the circuit's efficiency and required power output for the case study, which are constant. Furthermore, the weight of the cathodic heat exchanger is dominant, as well as the volume of the SOFC stack. Caused by the insulation material.

An exergy analysis is performed to investigate the exergy losses of the initial SOFC-system. The exergy flow diagram of the initial SOFC-system is shown in Figure 30.

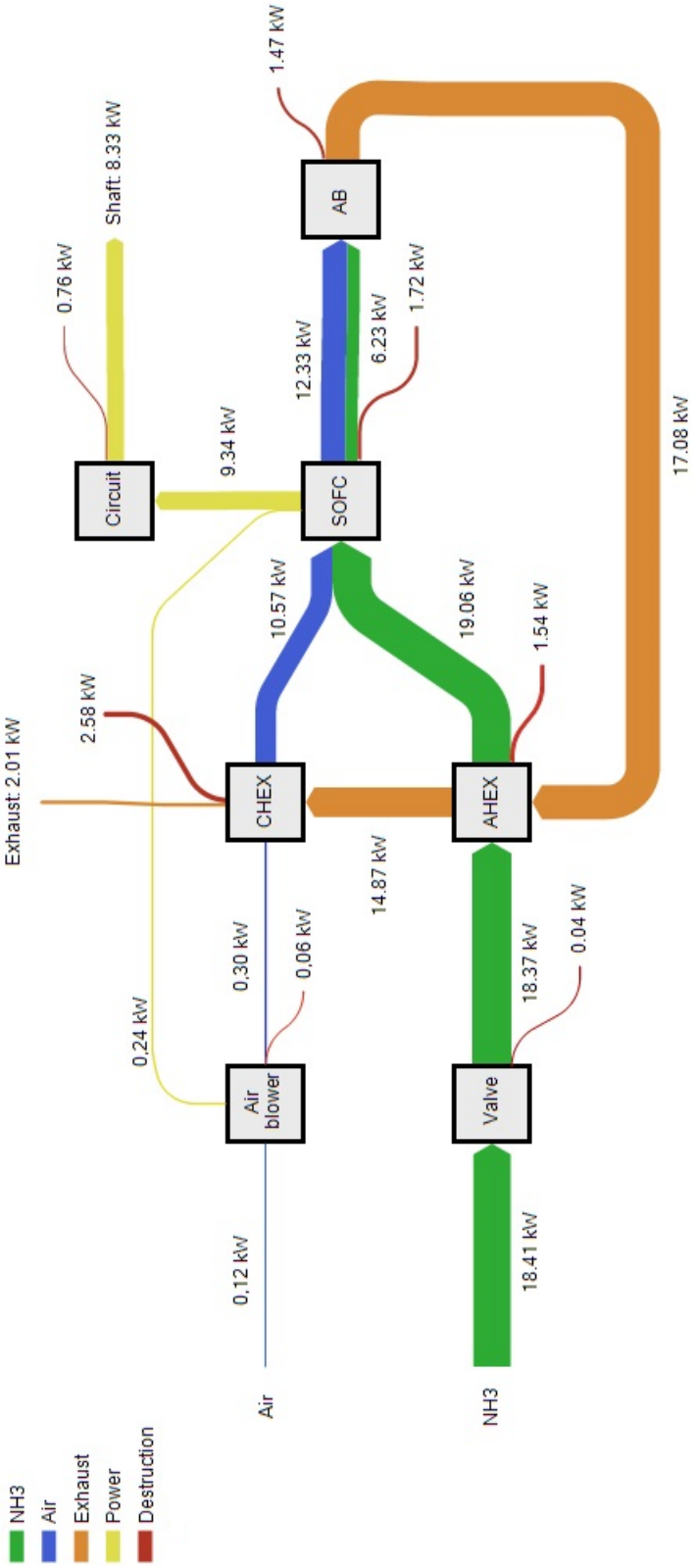

Figure 30: *Exergy flow diagram initial solid oxide fuel cell system. CHEX = cahtodic heat exchanger, AHEX = anodic heat exchanger, SOFC = solid oxide fuel cell and AB = afterburner.*

The useful exergy is 8.33 kW shaft work. The total exergy loss of the system is 10.18 kW. Resulting in an exergy efficiency of 45.0 %. The cathodic heat exchanger is the main loss mechanism, responsible for 25.3 % of the exergy losses. Figure 31 gives an overview of the exergy distribution of the initial SOFC-system.

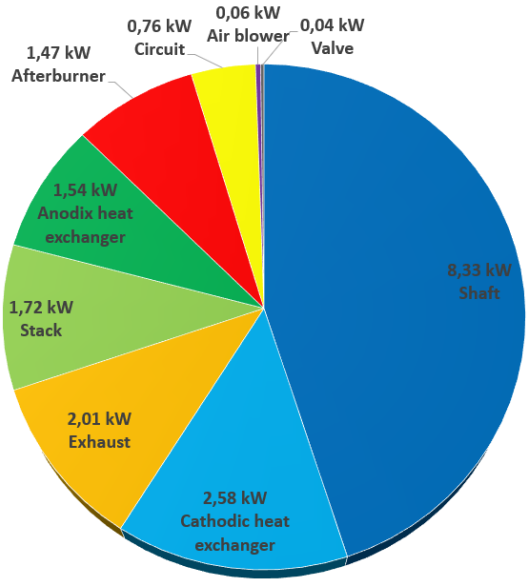

Figure 31: *Exergy distribution initial solid oxide fuel cell system.*

5.2 Sensitivity Analysis

A sensitivity analysis regarding the selected SOFC-system parameters is performed in order to gain insight in the effect on the system efficiency, equipment weight and equipment volume.

5.2.1 Number of Cells

As discussed in section 3.2 the number of cells in the stack determines the working point of each cell at fixed shaft power. The effect of the number of cells on the current density and cell voltage is shown in Figure 32. The consequence is a change in cell efficiency as seen in Figure 33.

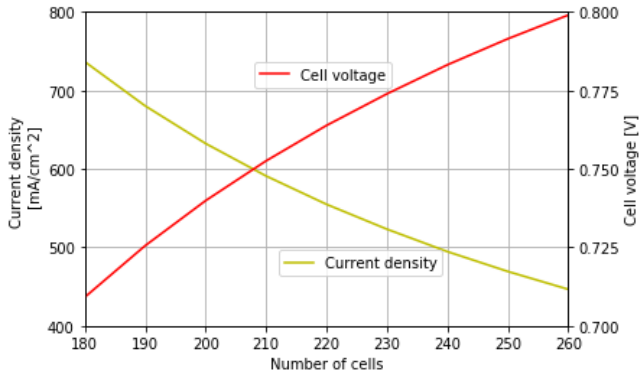

Figure 32: *Power density, current density and cell voltage as function of number of cells at U_f = 80 %, r_c = 0 % and r_a = 0 %.*

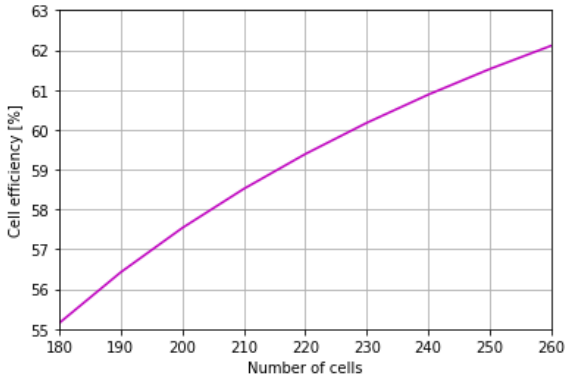

Figure 33: *Cell efficiency as function of number of cells at U_f = 80 %, r_c = 0 % and r_a = 0 %.*

Increasing the number of cells leads to a lower current density for the same shaft power. Operating at a lower current density decreases the activation and ohmic voltage losses as seen in Equation 32 and 34 respectively. Diffusion voltage losses also decrease, but are not significant in the operating current density range of the SOFC as seen in Figure 26. The lower voltage losses result into a higher operating cell voltage as seen in Figure 32, thereby increasing the cell efficiency, as seen in Figure 33.

When the cell operates more efficiently, less ammonia is needed to generate the required shaft power. Also, less heat is produced, leading to a decrease in air feed flow rate. The ammonia feed flow rate and air feed flow rate are plotted in Figure 34. The lower ammonia feed flow rate leads to a higher system efficiency, as seen in Figure 35.

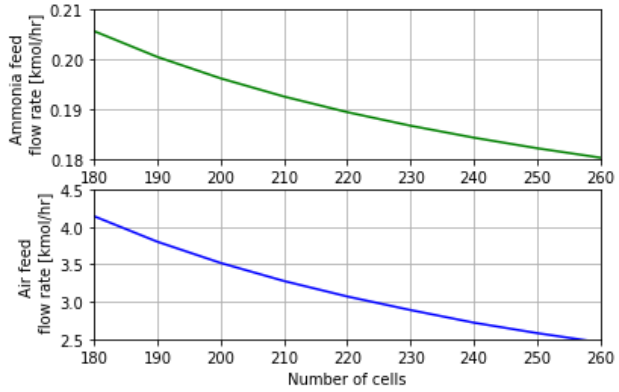

Figure 34: *Ammonia and air feed flow rate as function of number of cells at U_f = 80 %, r_c = 0 % and r_a = 0 %.*

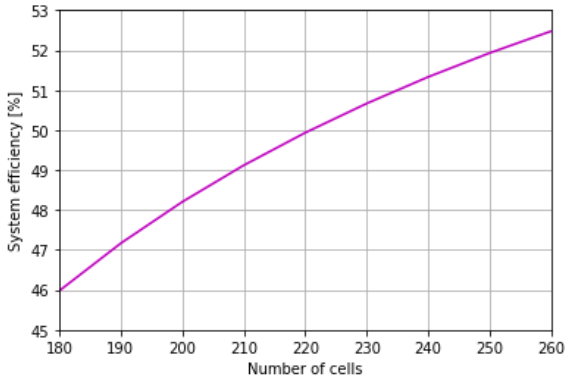

Figure 35: *System efficiency as function of number of cells at U_f = 80 %, r_c = 0 % and r_a = 0 %.*

Figure 34 shows a significant reduction in the air feed flow rate, over the selected number of cell range, whereas the cell efficiency only increases moderately. This is explained by the fact that the total decrease in heat production is translated to the air feed flow rate. Figure 66 in Appendix D visualizes this reduction with the energy distribution in the SOFC stack.

The combined changes in the number of cells, ammonia feed flow rate, air feed flow rate and system efficiency affect the size of the equipment, as shown in Figure 36 and 37 respectively.

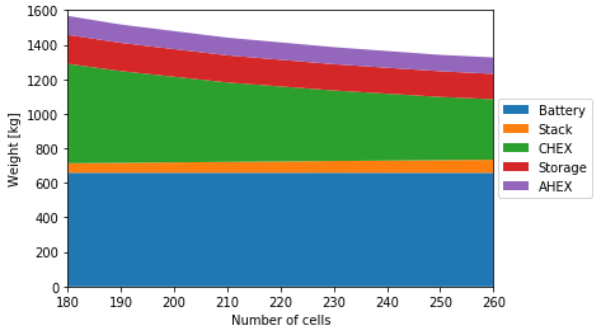

Figure 36: *Equipment weight as function of number of cells at U_f = 80 %, r_c = 0 % and r_a = 0 %.*

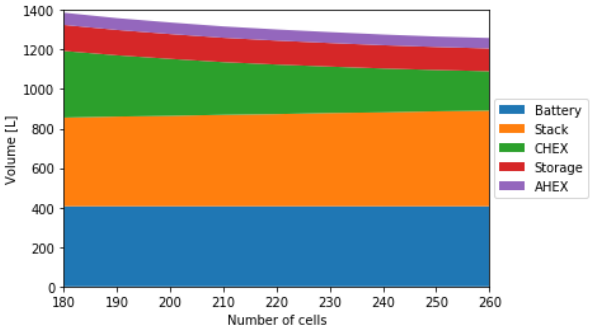

Figure 37: *Equipment volume as function of number of cells at U_f = 80 %, r_c = 0 % and r_a = 0 %.*

The stack size increases, due to the increase in number of cells. The storage size decreases owing to the higher system efficiency, reducing the ammonia consumption. Both the cathodic and anodic heat exchanger decrease in size, owing to the lower heat duty caused by the reduction in flow rates. The net effect of the increasing number of cells is a reduction in weight and volume of the SOFC-system.

5.2.2 Single-pass Fuel Utilization

The single-pass fuel utilization U_f is the amount of fuel reacted when passing the anode. Increasing the single-pass fuel utilization affects the mean hydrogen concentration in the fuel channel as seen in Figure 38.

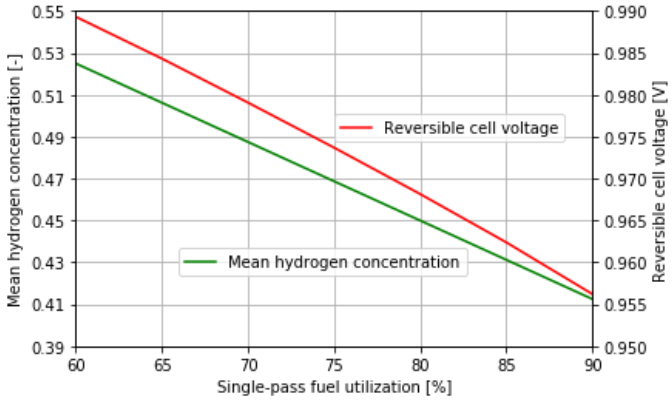

Figure 38: *Mean hydrogen concentration and reversible cell voltage as function of single-pass fuel utilization at* $\#_{cells} = 210$, $r_c = 0$ % *and* $r_a = 0$ %.

When the single-pass fuel utilization increases, more hydrogen reacts and its concentration decreases as seen in Figure 38. The decrease in hydrogen concentration leads to a lower reversible cell voltage according to the Nernst Equation 29 and higher anodic diffusion losses according to Equations 38 and 40. However, anodic diffusion losses are negligible in the operating current density range of the cell, as seen in Figure 26. The reduction in reversible cell voltage leads to a lower operating cell voltage. Therefore, the current density is increased maintain the required shaft power, as seen in Figure 39. The increase in current density increases the activation and ohmic voltage losses as seen in Equation 32 and 34 respectively. Diffusion voltage losses also increase, but are not significant in the operating current density range of the SOFC as seen in Figure 26. The higher voltage losses result in a lower cell efficiency, as plotted in Figure 40.

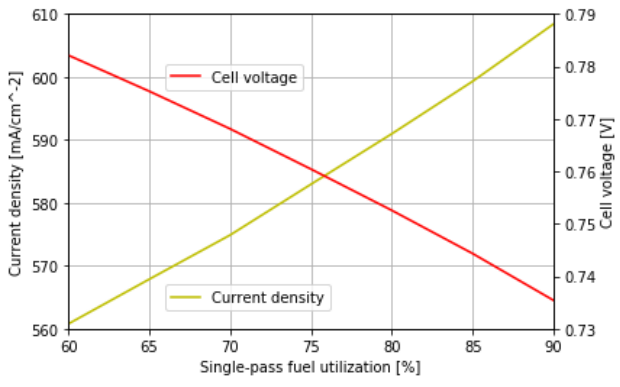

Figure 39: *Current density and cell voltage as function of single-pass fuel utilization at* $\#_{cells} = 210$, $r_c = 0$ % *and* $r_a = 0$ %.

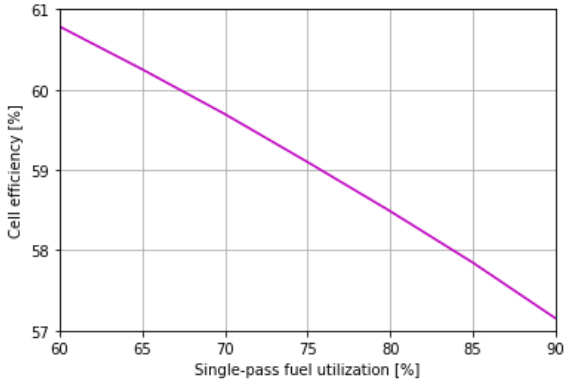

Figure 40: *Cell efficiency as function of single-pass fuel utilization at* $\#_{cells} = 210$, $r_c = 0$ % *and* $r_a = 0$ %.

The decrease in cell efficiency leads to more heat production. Therefore, the air cooling demand increases, as shown by the increase in air feed flow rate in Figure 41. The air feed flow rate rate increases in more extend than the decrease in cell efficiency, which is explained by the energy distribution in the SOFC stack in Figure 67 in Appendix D. However, the ammonia feed flow rate shows a decreasing trend, indicating that the single-pass fuel utilization has a stronger effect than the associated decrease in cell efficiency. The result is an increase in system efficiency, as shown by Figure 42.

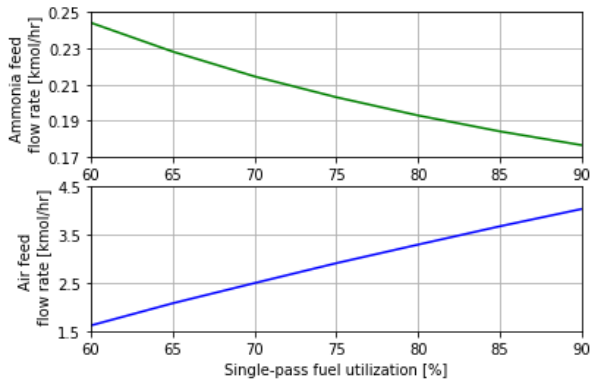

Figure 41: *Ammonia and air feed flow rateas function of single-pass fuel utilization at* $\#_{cells}$ *= 210,* r_c *= 0 % and* r_a *= 0 %.*

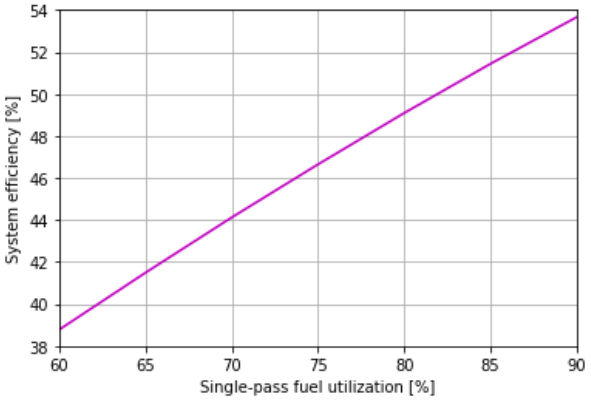

Figure 42: *System efficiency as function of single-pass fuel utilization at* $\#_{cells}$ *= 210,* r_c *= 0 % and* r_a *= 0 %.*

The decrease in ammonia feed flow rate leads to a decrease in storage size. However, the size of the cathodic heat exchanger is significantly increased due to a lower LMTD caused by the lower exhaust temperature. The SOFC-system weight and volume as function of single-pass fuel utilization are shown in Figure 43 and 44 respectively.

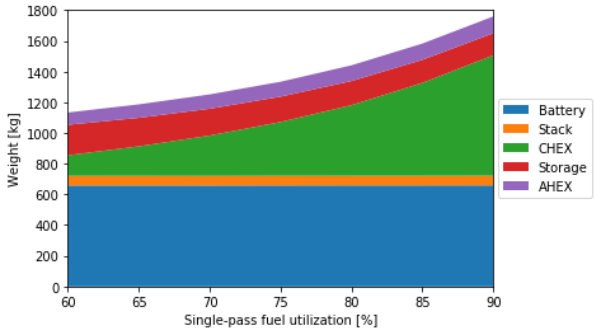

Figure 43: *Equipment weight as function of single-pass fuel utilization at* $\#_{cells}$ *= 210,* r_c *= 0 % and* r_a *= 0 %. CHEX = cathodic heat exchanger. AHEX = anodic heat exchanger.*

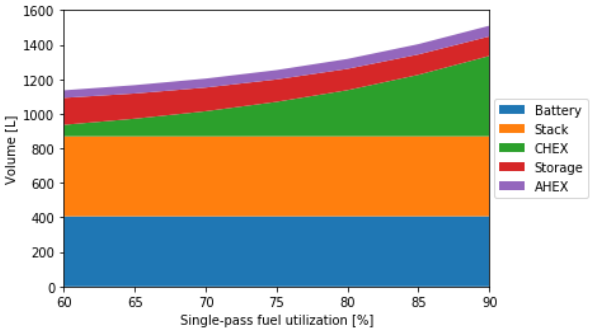

Figure 44: *Equipment volume as function of single-pass fuel utilization at* $\#_{cells}$ *= 210,* r_c *= 0 % and* r_a *= 0 %. CHEX = cathodic heat exchanger. AHEX = anodic heat exchanger.*

The 60 % lower limit of the single-pass fuel utilization is caused by insufficient oxygen for the afterburner. Because more hydrogen is burned instead of electrochemically converted.

5.2.3 Cathode Off-gas Recirculation

When air passes the cathode, oxygen is consumed and its concentration decreases. By recirculating part of the cathode off-gas, the inlet oxygen concentration is decreased. The result is a decrease in mean oxygen concentration at the cathode as seen in Figure 45. The consequence is a increase in the single-pass oxygen utilization. However, the change is minor, because the air feed is in excess to cool the SOFC stack. Therefore, there are neither significant changes in the cell nor system efficiency, as seen in Figure 46.

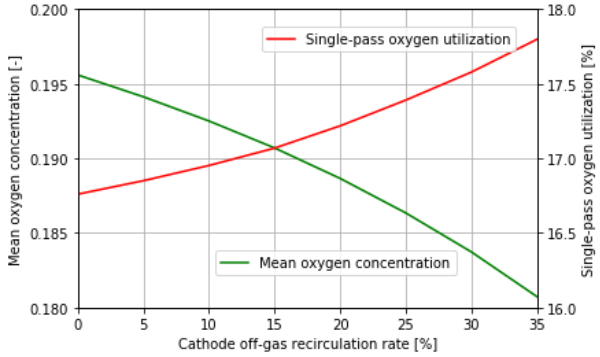

Figure 45: *Mean oxygen concentration as function of cathode off-gas recirculation rate at* $\#_{cells}$ *= 210,* U_f *= 80 % and* r_a *= 0 %.*

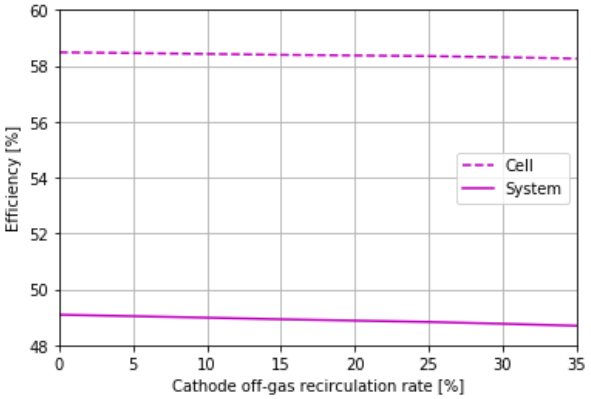

Figure 46: *Cell and system efficiency as function of cathode off-gas recirculation rate at* $\#_{cells}$ *= 210,* U_f *= 80 % and* r_a *= 0 %.*

The expected advantage of cathode off-gas recirculation was to reduce the size of the cathodic heat exchanger by preheating the air feed with part of the cathode off-gas. This reduces the heat duty as seen in Figure 68 in Appendix D. However, the LMTD decreases more significantly, thereby increasing the required heat transfer area, as seen in Figure 69 in Appendix D. The net effect is an increase in cathodic heat exchanger size. Leading to an increase in SOFC-system size, as shown in Figure 47 and 48.

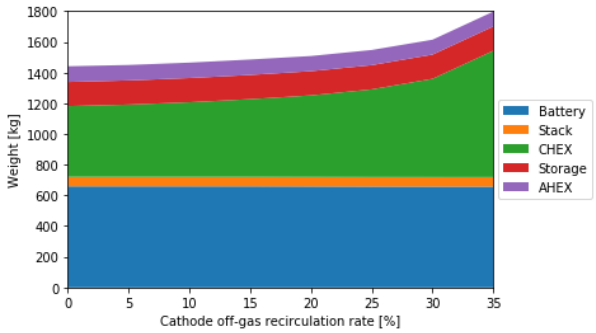

Figure 47: *Equipment weight as function of cathode off-gas rericulation rate at* $\#_{cells}$ *= 210,* U_f *= 80 % and* r_a *= 0 %.*

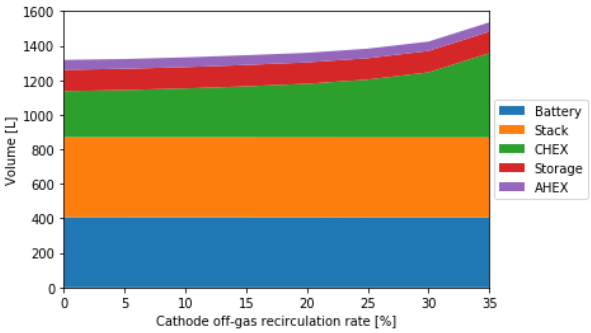

Figure 48: *Equipment volume as function of cathode off-gas rericulation rate at* $\#_{cells}$ *= 210,* U_f *= 80 % and* r_a *= 0 %.*

The 25 °air feed is preheated before the cahtodic heat exchanger by mixing with part of the 850 °cathode off-gas. By increasing the cathode off-gas recirculation, the temperature of the cold side cathodic heat exchanger inlet temperature increases. This is shown in Figure 49. Also plotted is the hot side cathode heat exchanger outlet temperature. This cross-current heat exchanger is determined to have a minimum pinch temperature of 10 °C. Beyond a cathode off-gas recirculation of 35 %, this pinch temperature is not sustained. Therefore, this is the limiting value.

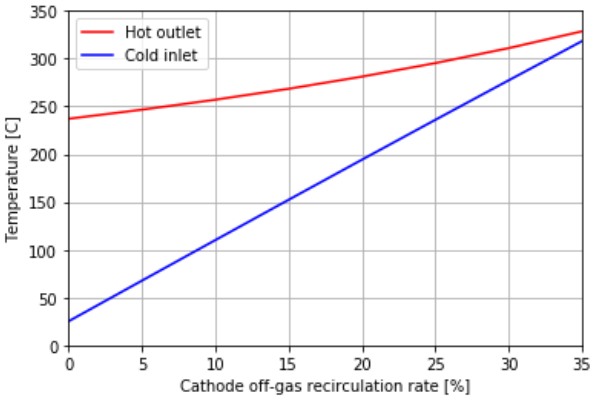

Figure 49: *Pinch temperature cathodic heat exchanger as function of cathode off-gas recirculation rate at* $\#_{cells} = 210$, $U_f = 80$ % *and* $r_c = 0$ %

5.2.4 Anode Off-gas Recirculation

By recirculating part of the anode off-gas, the overall fuel utilization is increased, as demonstrated in Figure 50. However, this anode off-gas has a lower hydrogen concentration due to hydrogen consumption. Therefore, the inlet hydrogen concentration is decreased. Resulting in a decrease in mean hydrogen concentration as seen in Figure 51. A lower hydrogen concentration leads to a lower reversible cell voltage as dictated by the Nernst Equation 29.

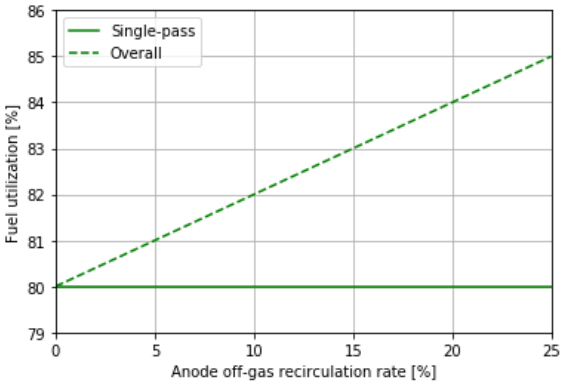

Figure 50: *Single-pass and overall fuel utilization as function of anode off-gas recirculation rate at* $\#_{cells} = 210$, $U_f = 80$ % *and* $r_c = 0$ %.

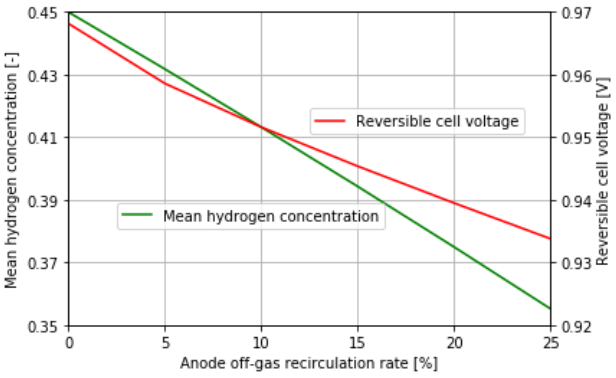

Figure 51: *Mean hydrogen concentration and reversible cell voltage as function of anode off-gas recirculation at* $\#_{cells} = 210$, $U_f = 80$ % *and* $r_c = 0$ %.

The lower reversible cell voltage leads to a decrease in cell voltage as seen in Figure 52. To maintain the required shaft power, the current density is increased. However, a higher current density leads to higher activation and ohmic losses as dedicated by Equation 32 and 34 respectively. Diffusion voltage losses also increase, but are not significant in the operating current density range of the SOFC as seen in Figure 26. The higher voltage losses lead to a decrease in cell efficiency, as shown in Figure 53.

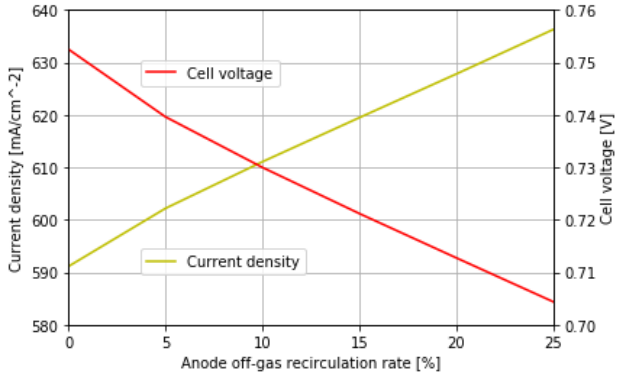

Figure 52: *Current density and cell voltage as function of anode off-gas recirculation rate at $\#_{cells}$ = 210, U_f = 80 % and r_c = 0 %.*

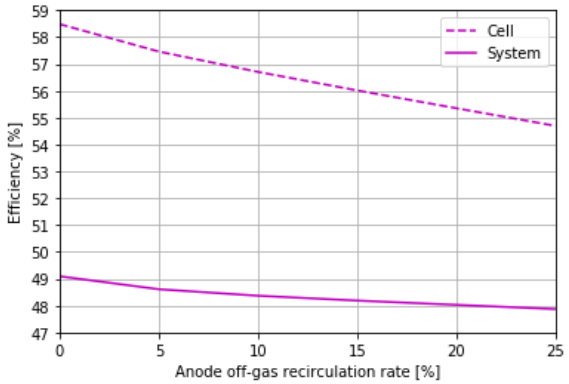

Figure 53: *Cell and system efficiency as function of anode off-gas recirculation at $\#_{cells}$ = 210, U_f = 80 % and r_c = 0 %.*

The upper limit of the anode off-gas recirculation rate is reached when the cell voltage is still above the minimum in the selected range: 0.70 V. Figure 53 shows also the system's efficiency. Although more fuel is utilized, the system's efficiency is decreasing. Caused by a more dominant decrease in cell efficiency.

Due to the decrease in cell efficiency, more heat is produced. Therefore, more cooling is required and the air feed flow rate is increased. This results in an increased heat duty for the cathodic heat exchanger, thereby increasing its weight and volume. The effect is an increase in weight and volume of the SOFC-system, as seen in Figure 54 and 55 respectively.

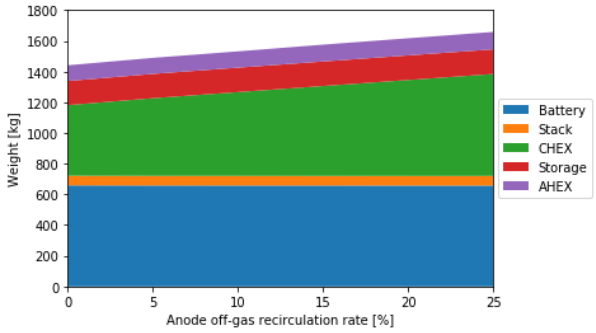

Figure 54: *Equipment weight as function of anode off-gas recirculation rate at $\#_{cells}$ = 210, U_f = 80 % and r_c = 0 %.*

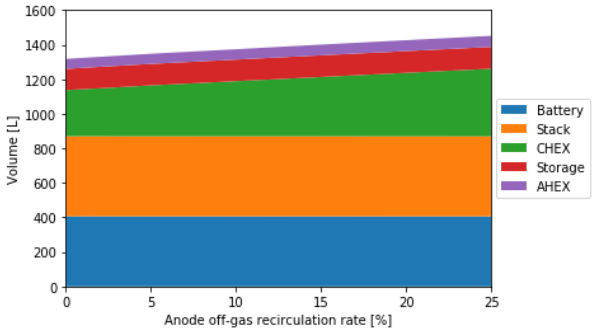

Figure 55: *Equipment volume as function of anode off-gas recirculation rate at $\#_{cells}$ = 210, U_f = 80 % and r_c = 0 %.*

5.3 Final Solid Oxide Fuel Cell System

Final values for the system parameters are selected by insight gained from the sensitivity analysis. The final system parameters are given in Table 13, together with the initial system parameters.

The number of cells in the stack is set to obtain a cell voltage of approximately 0.80 V, which is the upper limit in the operating voltage range of the SOFC as seen in Table 3. Increasing the number of cells in the stack increases the efficiency, decreases the weight and decrease the volume of the SOFC-system. The final value for the single-pass fuel utilization is set at 70 %. This is a trade-off between efficiency and sizing of the components. Chosen is to decrease the weight and volume of the SOFC-system at the cost of a lower efficiency. Values below 70 % fuel utilization still reduce the size of the SOFC-system, but only minor. While the system efficiency will drop significantly. Cathode off-gas recirculation and anode off-gas recirculation are

Table 13: *Final sensitivity system parameters.*

Operating parameter	Initial value	Final value
$\#_{cells}$	210	240
U_f	80 %	70 %
r_c	0 %	0 %
r_a	0 %	0 %

not beneficial for the SOFC-system as in this model. Neither to increase the system efficiency, nor to decrease the size. The calculated values for the equipment weight and equipment volume for the final SOFC-system compared to the initial SOFC-system are shown in Figure 56 and 57 respectively.

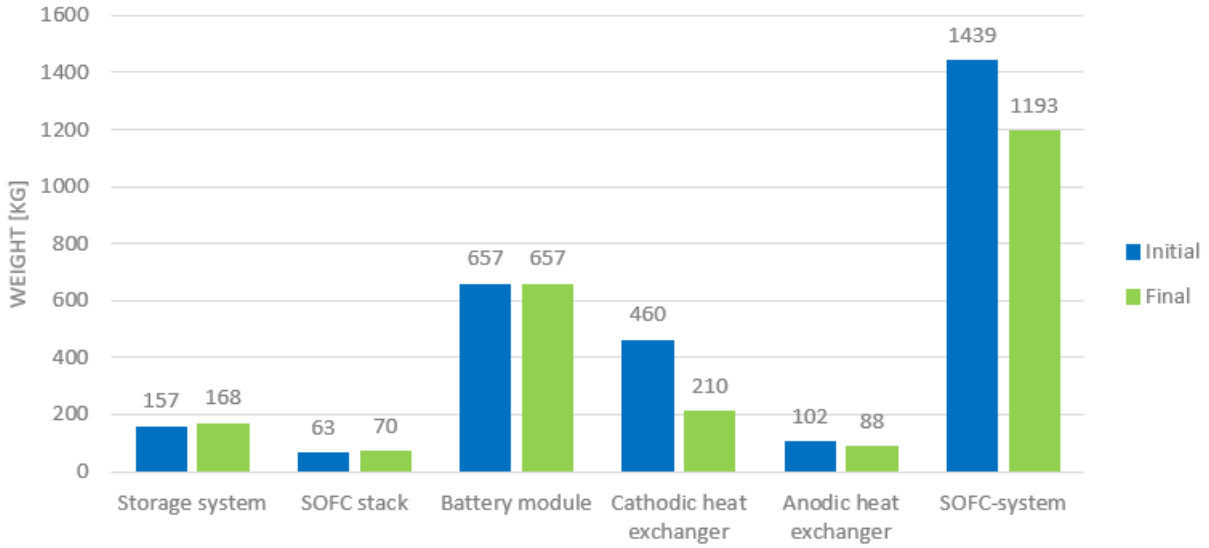

Figure 56: *Equipment weight and system weight of the initial and final solid oxide fuel cell system.*

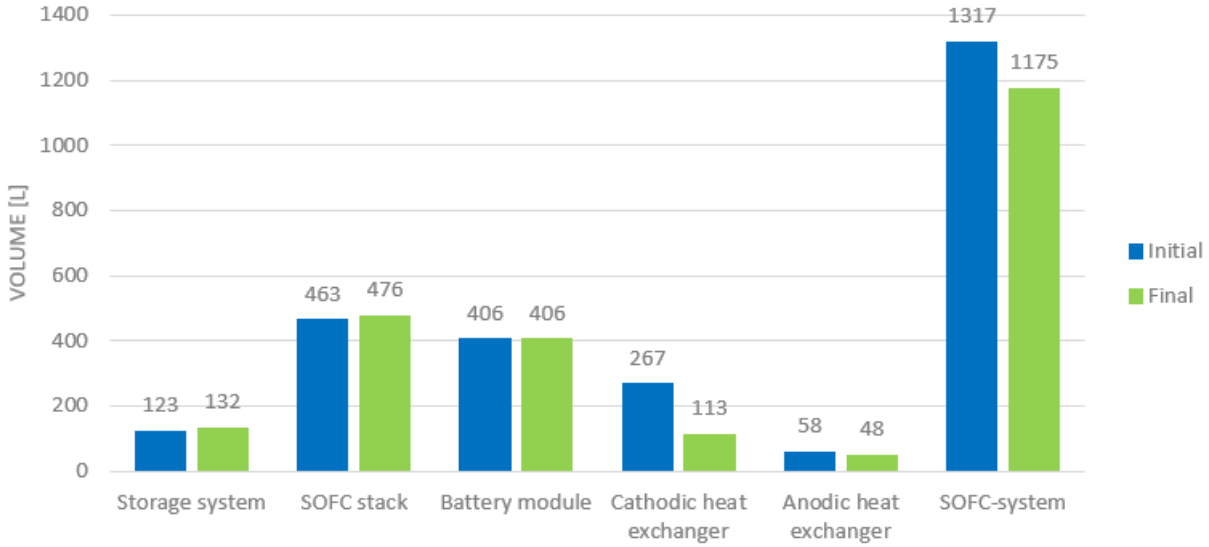

Figure 57: *Equipment volume and system volume of the initial and final solid oxide fuel cell system.*

The system efficiency decreased by 3.1 % point: From 49.1 % to 46.0 %. The lower efficiency results in an increase of ammonia consumption. Resulting in a slight increase in storage system. The increased number of cells leads to a increase in SOFC stack weight and volume. However, the total SOFC-system is reduced is size. Mainly caused by the improvement of the cathodic heat exchanger size: 250 kg reduction in weight and 154 L reduction in volume. The total system weight and volume reduced by 246 kg (-17.1 %) and 142 L (-10.8 %).

The battery module is unchanged and remains a dominant component in the final SOFC-system. Accounting for 55.1 % in weight and 34.6 % in volume. The SOFC stack volume is also a major part of the SOFC-system. Accounting for 40.5 %. A stream table of the final SOFC-system is shown in Figure 65 in Appendix C.

An exergy analysis was also performed for the final SOFC-system. The exergy flow diagram of the final SOFC-system is shown in Figure 60.

The total exergy loss of the system is 11.35 kW. Resulting in an exergy efficiency of 42.3 %. The exhaust stream is the main loss mechanism, responsible for 28.5 % of the exergy losses. The exergy losses in the components of the final SOFC-system are shown in Figure 59.

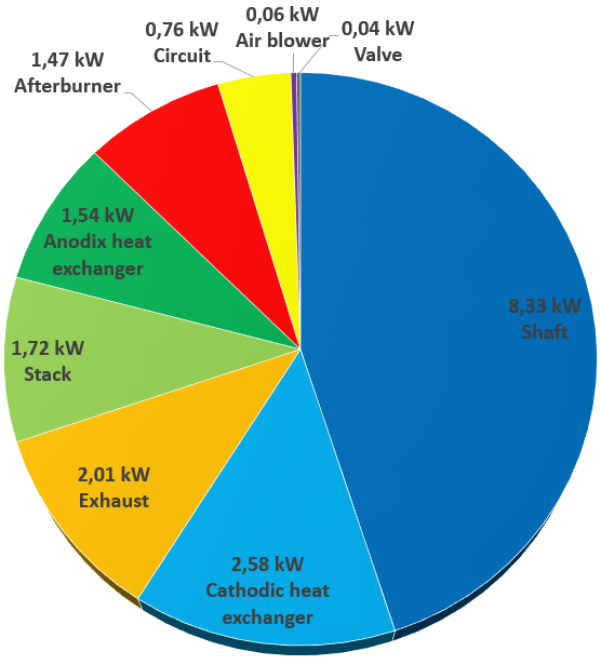

Figure 58: *Exergy distribution initial solid oxide fuel cell system.*

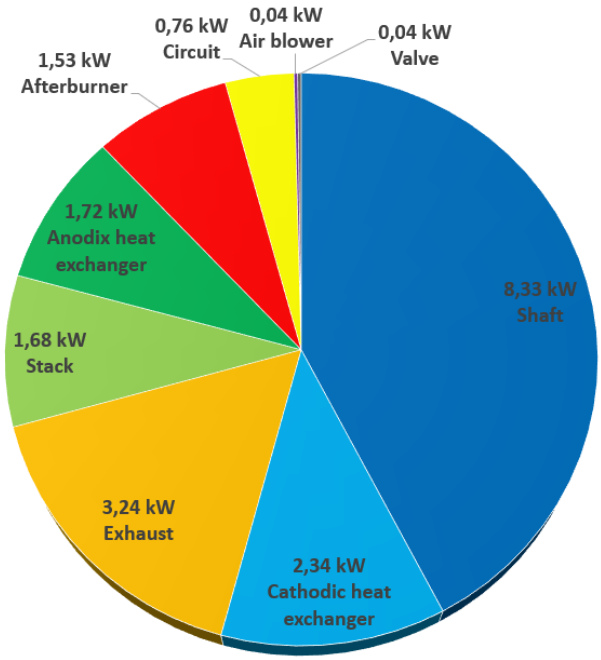

Figure 59: *Exergy distribution final solid oxide fuel cell system.*

The exergy loss in the SOFC stack is slightly reduced owing the the increased cell efficiency. All other components, except for the air blower and valve, have more exergy losses than the initial SOFC-system. This is caused by the increased temperature of the exhaust stream of the afterburner, established to reduce the size of the anodic and cathodic heat exchanger. The air blower exergy loss is decreased owing to a reduction in air feed flow rate.

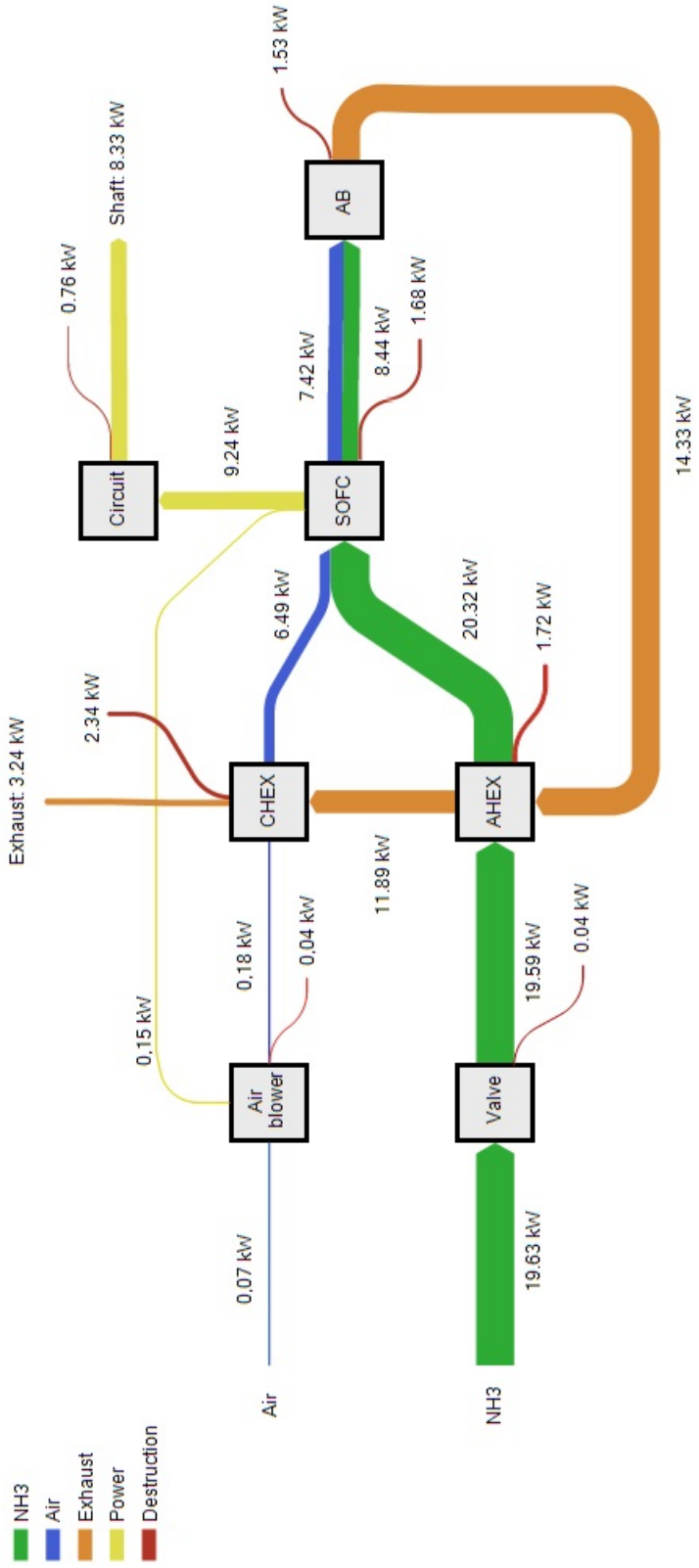

Figure 60: *Exergy flow diagram final solid oxide fuel cell system. CHEX = cahtodic heat exchanger, AHEX = anodic heat exchanger, SOFC = solid oxide fuel cell and AB = afterburner.*

5.4 Summary

A sensitivity analysis regarding the selected system parameters of the SOFC-system was performed. The insights from this sensitivity analysis are:

- An increase in the number of cells in the stack increases the system efficiency and reduces the sizes of the storage, anodic heat exchanger and cathodic heat exchanger at the cost of an increase in size of the SOFC stack. The net effect is a decrease in the SOFC-system size
- An increase of the single-pass fuel utilization reduces the cell efficiency but increases the system efficiency. The size of the storage is reduced at the cost of an increase in size of the cathodic and anodic heat exchanger. The net effect is a decrease in the SOFC-system size
- An increase of the cathode off-gas recirculation increases the size of the cathodic heat exchanger. Caused by a decrease in LMTD, dominating the decrease in heat duty. The net effect is a increase in the SOFC-system size
- An increase of the anode off-gas recirculation reduces the cell efficiency, dominating the increase in overall fuel utilization. This leads to an decrease in system efficiency. Resulting in an increase of the size of the cathodic heat exchanger. The net effect is a increase in the SOFC-system size

The final system parameters yield the following results to the main system performance indicators:

- Decrease system efficiency from 49.1 % to 46.0 %
- Decrease in weight of the system by 17.1 % to 1193 kg
- Decrease in volume of the system by 10.8 % to 1175 L
- The SOFC stack is the biggest component in volume, accounting for 40.5 %
- Battery module is the biggest component in weight and second biggest component in volume, accounting for 55.1 % and 34.6 % respectively
- Decrease exergy efficiency from 45.0 % to 42.3 %

6 Conclusion & Recommendations

The objective of the research work in this MSc thesis is to investigate the technical viability of a sustainable SOFC propulsion system fueled by ammonia. Technical viability is defined in this MSc thesis by weight and volume of the SOFC-system, whereas sustainability is determined by efficiency and emissions. The selected case study is a vessel from the Watertaxi Rotterdam company with an assumed shaft power of 25 kW.

A model was compiled capable of calculating the efficiency, weight of the equipment and volume of the equipment. The model accounts for activation losses, ohmic losses and diffusion losses within the SOFC.

The questions to be answered are:

- **What are the components of the SOFC propulsion system?**

The main component of the system is the SOFC stack. The SOFC stack has an assumed uniform operating temperature of 800 °C. To avoid thermal stress, the air and ammonia feed flow are preheated by a cathodic and anodic heat exchanger respectively, using the heat from the exhaust gas. An afterburner is used to burn the unreacted hydrogen, thereby increasing the temperature of the exhaust gas. Ammonia is stored as a liquid at a pressure of 20 bar at ambient temperature. A valve is used to obtain the desired ammonia feed flow rate and to reduce the pressure to the operating pressure of the SOFC stack. An air blower is used to generate the air feed flow rate. A battery module is used to compensate for temporarily imbalances between power demand and power supply. An electromotor converts electricity to mechanical shaft power. DC/DC converters and a DC/AC inverter are integrated in the electrical circuit to match the voltage and current of the electrical components.

- **Which system parameters influence the system's efficiency, equipment weight and equipment volume?**

The system parameters studied in this MSc thesis are the number of cells in the SOFC stack, single-pass fuel utilization, cathode off-gas recirculation rate and anode off-gas recirculation rate.

- **What are the optimal system parameters for the SOFC propulsion system?**

Optimisation of the SOFC-system was not possible, due to the trade-off between efficiency and size of the SOFC-system. The final system parameters are set by insight gained from the sensitivity study: 240 cells in the stack, which is the limit to stay below the upper limit of the cell working voltage of 0.8 V, 70 % single-pass fuel utilization, which is based on a trade-off between efficiency and size of the SOFC-system, 0 % cathode off-gas recirculation and 0 % anode off-gas recirculation.

Increasing the number of cells has the logical result of increasing the SOFC stack size, However, a higher cell and system efficiency is obtained. Resulting in a decrease in weight and volume of the SOFC-system, owing to a decrease in ammonia storage, cathodic heat exchanger size and anodic heat exchanger size.

Increasing the single-pass fuel utilization leads to a decrease in cell efficiency, but to an increase in system efficiency, owing to more utilization of the ammonia. This lowers the size of the ammonia storage. However, the size of the cathodic and anodic heat exchanger are found to increase significantly, mainly due to a lower LMTD in the heat exchanger caused by a significant lower exhaust temperature. The overall effect is an increase in weight and volume of the SOFC-system.

Recirculation of the cathode off-gas has no significant effect on the cell and system efficiency presented in this work: The decrease is minimal, owing to a the fact that the oxygen concentration is not significantly changed because air is in excess to cool the SOFC stack. The weight and volume of the SOFC-system are found to increase, due to an increase in weight and volume of the cathodic heat exchanger caused by a lower LMTD.

Recirculation the anode off-gas increases the overall fuel utilization, but decreases cell efficiency. The net effect is a decrease in system efficiency. Resulting in an increase in ammonia storage. Furthermore, the size of the anodic heat exchanger increases due to a lower LMTD.

- **What decrease in GHG reduction can be achieved?**

The diesel engine system in selected case study emits 58.7 ton carbon dioxide on a yearly basis. Furthermore, nitrogen oxide emissions could be significant due to the high operating temperature of the engine. The ammonia fueled SOFC-system does not emit any carbon dioxide. Also, NO_x emissions are negligible owing to the low operating temperature.

- **What are the most important exergy loss mechanisms in the SOFC propulsion system?**

The exergy efficiency of the SOFC-system is 42.3 %. The exhaust gas is the main exergy loss mechanism, accounting for 27.6 %. The exhaust gas is followed by the cathodic (20.6 %) and anodic heat exchanger (15.2 %) respectively. For all three loss mechanisms, the high exhaust temperature causes the significant exergy losses. The high exhaust temperature is necessary to reduce the weight and volume of the cathodic and anodic heat exchanger.

Main conclusion

The SOFC-system compared to the current diesel engine system is compared below:

Propulsion system	Weight [kg] system + fuel	Volume [L] system + fuel	Efficiency [%]	CO_2 $[\frac{ton_{CO_2}}{year}]$	NO_x
Diesel engine	278	434	35.0	58.7	significant
Solid oxide fuel cell	1199	1175	46.0	0.0	negligible

The efficiency of the SOFC-system is 11.0 % point higher than the current diesel engine system. Also, the SOFC-system fueled by sustainable synthesized ammonia has the potential of zero carbon dioxide emission. Furthermore, NO_x emissions are negligible in comparison to the diesel engine system. However, the weight and volume of the SOFC-system are significantly larger, caused by the dominant size of the battery module, needed for compensating for temporarily imbalances between power demand and power supply. The cathodic heat exchanger also remains a significant component in therms of weight and volume.

The large volume and high weight of the SOFC-system render the system to be unattractive for application on an inland vessel of the size of the selected case study with a daily tank frequency with respect to the current technology of batteries. Larger sized vessels could be better suited for installation of the SOFC-system:

- The more continuous operation schedules of larger vessels may allow for significant reduction or elimination of battery capacity requirements
- Large sized vessels may allow for more tolerance regarding heavy and bulky equipment
- The more efficient SOFC-system reduces the fuel consumption, which could be significant for large vessels unable to refuel on a daily basis

Recommendations

From this MSc thesis, learning's and recommendations for further research are draw.

1-dimensional SOFC model

The electrochemical behavior of SOFCs is not constant over the length of the electrode, therefore it is recommended to expand the current 0-dimensional model into a 1-dimensional model to improve the accuracy. For example, temperature, molar concentration, cell voltage and current density, etc. all vary over the length of the electrode, affecting the cell performance.

Heat exchanger design
Designing of heat exchanges is complex. The sizing of the cathodic and anodic heat exchanger is done with a constant value of the heat transfer coefficient obtained from Aspen Plus. In practice, the heat transfer coefficient varies based on the flow rates among other parameters. To increase the accuracy of the heat exchanger sizing, a more precise calculation method for designing the heat exchanger should be implemented.

Cathodic heat exchanger configuration
In the current SOFC-system model, the cathodic heat exchanger is located after the cathodic mixer. The limit of cathode off-gas recirculation rate is therefore limited by the pinch temperature. But more important, the size of the cathodic heat exchanger increases due to a significant decrease in LMTD. By placing the cathodic heat exchanger before the cathodic mixer, the LMTD is unaffected. Hence, cathode off-gas recirculation in this configuration could reduce the size of the cathodic heat exchanger by mixing with air feed flow, owing to a reduction in heat duty. A disadvantage of this configuration would be the challenge to control the inlet temperature.

CHP application
To make use of the SOFC potential, the high exhaust temperature of the SOFC-system could be used: Application of a bottoming cycle could be investigated to improve the efficiency of the SOFC-system by utilization of the high temperature exhaust in a turbine. Another option is to use the exhaust heat for heating purposes. For the small inland vessel, heating of the cabin during cold days could be established. For large vessels, heating of the rooms, cooking and other heat applications could be established.

Dynamic power pattern
In order to design for the right energy and power demand, a power pattern of the case study selected should be obtained. This power pattern leads to a more accurate model, battery module sizing and required SOFC stack power.

Application: Large vessels
As mentioned, the small, mobile inland vessel selected for the case study is unattractive for the SOFC-system due the the large sized battery module necessary to compensate for temporarily imbalances between power demand and power generation. Larger sized vessels could be more practical to the SOFC-system owing to the more continuous operation, thereby reducing or eliminating the battery module capacity. Also, larger sized vessels could be more tolerant for larger sized equipment.

Selecting the system parameters for the SOFC-system is different for the large vessels compared to the small inland vessel. The inland vessel is able to refuel on a daily basis. However, larger vessels are not able to refuel for longer periods of time. Therefore, efficiency plays a more important role for large vessels to reduce storage size. However, increasing the efficiency goes at the cost of larger heat exchangers.

Economical viability
There is not only a trade-off between size of the SOFC-system and efficiency, but also on the cost. As cost analysis was not an objective of this MSc thesis, completion of a cost analysis in future research is recommended to investigate the business model of the SOFC propulsion system. When performing a cost analysis, lifetime of the SOFC-system or its components is important to study o account for depreciation. Also, efficiency could play a role to reduce the cost of the ammonia consumption.

Safety
Besides studies relating to technical or economical viability, safety is an important issue to tackle. Pure ammonia is toxic and corrosive and must be handled according to.

References

[1] B. Roy X. Mao D. Rutherford N. Olmer, B. Comer. Greenhouse Gas Emissions from Global Shipping, 2013-2015. Technical report, 2017.

[2] DNV GL. Maritime Forecast to 2050. Technical report, 2019.

[3] The Engineering Toolbox. Ammonia - Thermophysical Properties. https://www.engineeringtoolbox.com/ammonia-d_1413.html. Accesed at 2020-02-25.

[4] Pubchem. Ammonia (Compound). https://pubchem.ncbi.nlm.nih.gov/compound/Ammonia. Accesed at 2020-02-25.

[5] Hideaki Kobayashi, Akihiro Hayakawa, K. D.Kunkuma A. Somarathne, and Ekenechukwu C. Okafor. Science and technology of ammonia combustion. *Proceedings of the Combustion Institute*, 2019.

[6] The Engineering Toolbox. Ammonia - Vapour Pressure at gas-liquid equilibrium. https://www.engineeringtoolbox.com/ammonia-pressure-temperature-d_361.html. Accesed at 2020-02-25.

[7] Pubchem. Hydrogen (Compound). https://pubchem.ncbi.nlm.nih.gov/compound/Hydrogen. Accesed at 2020-02-25.

[8] Massimiliano Cimenti and Josephine M. Hill. Direct utilization of liquid fuels in SOFC for portable applications: Challenges for the selection of alternative anodes, 2009.

[9] A. Fuerte, R. X. Valenzuela, M. J. Escudero, and L. Daza. Ammonia as efficient fuel for SOFC. *Journal of Power Sources*, 2009.

[10] Ahmed Afif, Nikdalila Radenahmad, Quentin Cheok, Shahriar Shams, Jung H. Kim, and Abul K. Azad. Ammonia-fed fuel cells: A comprehensive review, 2016.

[11] Jeffrey Ralph Bartels. *A feasibility study of implementing an Ammonia Economy*. PhD thesis, 2008.

[12] Nguyen Q. Minh. Solid oxide fuel cell technology - Features and applications, 2004.

[13] G. Cinti, G. Discepoli, E. Sisani, and U. Desideri. SOFC operating with ammonia: Stack test and system analysis. *International Journal of Hydrogen Energy*, 2016.

[14] DLR. Hybrid Power Plant. https://www.dlr.de/vt/en/desktopdefault.aspx/tabid-9006/18909_read-15119. Accesed at 2020-01-08.

[15] James Larminie and Andrew Dicks. *Fuel cell systems explained: Second edition*. 2013.

[16] S. P.S. Badwal, S. Giddey, C. Munnings, and A. Kulkarni. Review of progress in high temperature solid oxide fuel cells, 2014.

[17] Muneeb Irshad, Khurram Siraj, Rizwan Raza, Anwar Ali, Pankaj Tiwari, Bin Zhu, Asia Rafique, Amjad Ali, Muhammad Kaleem Ullah, and Arslan Usman. A brief description of high temperature solid oxide fuel cell's operation, materials, design, fabrication technologies and performance, 2016.

[18] Alumax. Maas taxi Rotterdam. https://alumaxboats.nl/nl/werkboten/specials/watertaxi-rotterdam/. Accesed at 2020-03-03.

[19] The Engineering Toolbox. Fuels - Higher and Lower Calorific Values. https://www.engineeringtoolbox.com/fuels-higher-calorific-values-d_169.html. Accesed at 2020-02-26.

[20] H.H.J. Vreuls. The Netherlands: list of fuels and standard CO2 emission factors. Technical report, SenterNovem, 2004.

[21] J. Staniforth and R. M. Ormerod. Clean destruction of waste ammonia with consummate production of electrical power within a solid oxide fuel cell system. *Green Chemistry*, 5:606–609, 2003.

[22] V. Hacker and K. Kordesch. Ammonia crackers. In *Handbook of Fuel Cells*. 2010.

[23] Siamak Farhad and Feridun Hamdullahpur. Conceptual design of a novel ammonia-fuelled portable solid oxide fuel cell system. *Journal of Power Sources*, 2010.

[24] Meng Ni. Thermo-electrochemical modeling of ammonia-fueled solid oxide fuel cells considering ammonia thermal decomposition in the anode. *International Journal of Hydrogen Energy*, 2011.

[25] N. J. J. Dekker and G. Rietveld. Highly Efficient Conversion of Ammonia in Electricity by Solid Oxide Fuel Cells. *Journal of Fuel Cell Science and Technology*, 2006.

[26] P. Aguiar, C. S. Adjiman, and N. P. Brandon. Anode-supported intermediate temperature direct internal reforming solid oxide fuel cell. I: Model-based steady-state performance. *Journal of Power Sources*, 2004.

[27] Robert J. Kee, Huayang Zhu, and David G. Goodwin. Solid-oxide fuel cells with hydrocarbon fuels. *Proceedings of the Combustion Institute*, 2005.

[28] G. Cinti, U. Desideri, D. Penchini, and G. Discepoli. Experimental Analysis of SOFC Fuelled by Ammonia. *Fuel Cells*, 14:221–230, 2014.

[29] Adam Wojcik, Hugh Middleton, Ioannis Damopoulos, and Jan Van Herle. Ammonia as a fuel in solid oxide fuel cells. In *Journal of Power Sources*, 2003.

[30] Office of Fossil Energy. Fuel Cell Stacks Still Going Strong After 5000 Hours. https://www.energy.gov/fe/articles/fuel-cell-stacks-still-going-strong-after-5000-hours, Data Accesed: 12-03-2020, 2009.

[31] Yakov BorisovichHG Zeldovich. Oxidation of Nitrogen in Combustion and Explosions. In *Selected Works of Yakov Borisovich Zeldovich, Volume I*. 2015.

[32] Christopher H Wendel. *Design and analysis of reversible solid oxide cell systems for electrical energy storage*. PhD thesis, 2015.

[33] A. Ghazel M. Murnane. A Closer Look at State of Charge and State of Health Estimation Techniques for Batteries. https://www.analog.com/media/en/technical-documentation/technical-articles/A-Closer-Look-at-State-Of-Charge-and-State-Health-Estimation-Techniques-....pdf, Accesed at 10-03-2020.

[34] ARADEX. DC/DC converters for batteries, super-caps and fuel cells. page 8, 2018.

[35] MAN. Diesel-electric Drives. https://marine.mandieselturbo.com/docs/librariesprovider6/marine-broschures/diesel-electric-drives-guideline.pdf, 2018.

[36] C. Morris. Tesla Vehicle Efficiency Leads Industry Thanks To Tesla Vehicle Design Culture. https://cleantechnica.com/2019/10/05/tesla-vehicle-efficiency-leads-industry-thanks-to-tesla-vehicle-design-culture/.

[37] Danylo Oryshchyn, Nor Farida Harun, David Tucker, Kenneth M. Bryden, and Lawrence Shadle. Fuel utilization effects on system efficiency in solid oxide fuel cell gas turbine hybrid systems. *Applied Energy*, 2018.

[38] J. Szargut. *Exergy Method*. Southampton, 2005.

[39] Stuart W. Churchill and Humbert H.S. Chu. Correlating equations for laminar and turbulent free convection from a vertical plate. *International Journal of Heat and Mass Transfer*, 1975.

[40] W. H. McAdams. *Heat transmission*. McGraw-Hill, 3rd ed. edition, 1954.

[41] The Engineering Toolbox. Thermal Conductivity of Selected Materials and Gases. https://www.engineeringtoolbox.com/thermal-conductivity-d_429.html. Accesed at 2020-02-27.

[42] Dr. E. Gyenge. Fuel Cells and Electrochemical Engineering. Technical report, 2019.

[43] Kevin Kendall and Michaela Kendall. *High-Temperature Solid Oxide Fuel Cells for the 21st Century: Fundamentals, Design and Applications: Second Edition*. 2015.

[44] The Engineering Toolbox. Young Modulus. https://www.engineeringtoolbox.com/young-modulus-d_417.html. Accesed at 2020-03-04.

[45] The Engineering Toolbox. Factors of Safety. https://www.engineeringtoolbox.com/factors-safety-fos-d_1624.html, 09-03-2020.

[46] R. Sinnot G. Towler. *Chemical Engineering Design*. Elsevier, second edi edition, 2013.

[47] PCC Company. High Performance Nickel Alloys. https://www.specialmetals.com/assets/smc/documents/pcc-8064-sm-alloy-handbook-v04.pdf, Accesed at 09-03-2020.

[48] The Engineering Toolbox. Density of Selected Solids. https://www.engineeringtoolbox.com/density-solids-d_1265.html. Accesed at 2020-02-27.

Appendix A: Fuel Cell Thermodynamics

A fuel cell is an device that electrochemically converts chemical energy into electrical energy. This conversion is established by a redox-reaction: At the anode the oxidation reaction takes place and at the cathode the reduction reaction takes place.

Gibbs Free Energy

Fuel cell's deliver power spontaneously. Therefore, the standard Gibbs free energy of the cell must be negative. The standard Gibbs free energy G, calculated by Equation 63 [42], of the cell is maximal amount of work that can be extracted.

$$\Delta G^{\circ}_{cell,T} = \Delta G^{\circ}_{oxidation,T} + \Delta G^{\circ}_{reduction,T} < 0 \tag{63}$$

The used convention is to write electrons on the left hand side of the reaction. For a fuel cell, the anode delivers the electrons and the cathode consumes the electrons. Therefore, equation 63 can therefore be written by Equation 64.

$$\Delta G^{\circ}_{cell,T} = \Delta G^{\circ}_{c,T} - \Delta G^{\circ}_{a,T} < 0 \tag{64}$$

The Gibbs free energy is dependent on temperature. To take this into account, Equation 65 [42] is used.

$$\frac{\partial \Delta g^{\circ}_{cell,T}}{\partial T} = -\Delta s^{\circ}_{cell}(T) \tag{65}$$

When the cell is in electrochemical equilibrium, no net flow of electrons is present: The rates of the oxidation and reduction reactions are equal. The electrochemical equilibrium is reached when the Gibbs free energy of the ionic conductor and electronic conductor are equal, as in Equation 66 [42].

$$\Delta g^{\circ}_{cell,T} = -\mu \cdot F \cdot \phi^{\circ}_{cell,T} \tag{66}$$

Activity of Species

In non-ideal conditions the activity of species is $\neq 1$. The Gibbs free energy can then be calculated with the Nernst Equation 67 [42].

$$\phi_{cell,T} = \phi^{\circ}_{cell,T} - \frac{R \cdot T}{\mu \cdot F}\, ln\ \Pi a_j^{S_j} \tag{67}$$

The activity of a gas species can be calculated with Equation 68 [42].

$$a_{gas} = f_{gas}\ \frac{p_{gas}}{p^{\circ}} \tag{68}$$

where f_{gas} is the fugacity coefficient of the gass, p_g is the partial pressure of the gas and p° is the reference pressure of 1 bar.

Faraday's Law

The correlation between electrical current and consumption/production of species is Faraday's constant: F = 96,485 C/mol. Faraday's law, given by Equation 69 [42], states that an electrochemical transformation with one electron and 100 % current efficiency $\phi_{current}$ involves Faraday's constant as a charge.

$$-\frac{\dot{n}_j}{S_j} = \frac{I}{\mu \cdot F} \tag{69}$$

By convention the cathodic current is negative and the anodic current is positive.

Voltage Loss Mechanisms

There are four types of voltage loss mechanisms in a fuel cell: activation losses, fuel crossover and internal current losses, ohmic losses and diffusion losses. Since fuel crossover and internal current losses are negligible in SOFCs [15], these will not be discussed.

Activation Losses

Activation losses indicate the slowness of the reactions taking place on the surface of the electrode. The chemical reaction for transferring electrons to and from the electrode need a proportion of the voltage. The rate of electrode reaction was described in Faraday's Equation. This rate of reaction is the balance of cathodic and anodic reaction. Therefore, Faraday's law can be rewritten as in Equation 70 [42].

$$\frac{i}{n \cdot F} = r = \overleftarrow{r_a} - \overrightarrow{r_c} = k_a \cdot a_{red} - k_c \cdot a_{ox} \tag{70}$$

So far the influence of the electrode potential has not been taken into account. This influence can be introduced based on the Arrhenius Equation 71 [42].

$$k = A \cdot \exp(-\frac{\Delta G^*}{R \cdot T}) \tag{71}$$

where A is a pre-exponential factor which depends on the frequency and probability of molecular collisions and hence depend on temperature and ΔG^* is the free energy of activation.

At the standard potential, the rates in cathodic and anodic directions are equal, the net current is zero, hence the free energies of activation should be equal. For the SOFC, the cathodic reaction is favored, while the anodic reaction is inhibited. The fraction of the energy input which goes into lowering the activation energy of the cathodic reaction is given by the symmetry factor β. Using this factor in combination with Equation 30 gives Equations 72 and 73 for the cahtodic and anodic reaction respectively.

$$\Delta G_c^* = \Delta G_c^{*,0} + \beta \cdot n \cdot F(E - E^0) \tag{72}$$

$$\Delta G_a^* = \Delta G_a^{*,0} - (1 - \beta) \cdot n \cdot F(E - E^0) \tag{73}$$

Inserting Equation 72 and 73 in the Arrhenius Equation 71 leads to Equations 74 and 75.

$$k_c = k^0 \cdot \exp - \frac{\beta \cdot n \cdot F(E - E^0)}{R \cdot T} \tag{74}$$

$$k_a = k^0 \cdot \exp \frac{(1 - \beta)\ n \cdot F(E - E^0)}{R \cdot T} \tag{75}$$

where k^0 is the standard heterogeneous rate constant. It is exclusively dependent on the intrinsic electrocatalytic properties of the electrode material. Fast electrode kinetics is typically characterised by $k^0 \sim 10^{-2}$ - 10^{-1} m $\cdot$ s^{-1}, while sluggish electrode kinetics is characterised by $k^0 \sim 10^{-}11$ m $\cdot$ $s^{-}1$ [42].

Inserting Equations 74 and 75 into Equation 70 gives a general expression between the current density and the activation overpotential as in Equation 76.

$$i = n \cdot F \cdot k^0 [a_{red} \cdot \exp(\frac{(1 - \beta) \cdot n \cdot F(E - E^0)}{R \cdot T}) - a_{ox} \cdot \exp(-\frac{\beta \cdot n \cdot F(E - E^0}{R \cdot T})] \tag{76}$$

At equilibrium potential the rates of the forward and backward reactions are equal, hence the anodic current is equal to the absolute value of the cathodic current and defined as the exchange current density. The exchange current density is at zero current density. However, this does not impose there is no activity. The higher the value of the exchange current density, the more active the electrode is. By increasing the current density, the reaction is simply shifted in the preferred direction. Substituting these effects in Equation 76 results in Equation 77.

$$i_o = n \cdot F \cdot k^0 \cdot a_{red} \cdot \exp(\frac{(1-\beta)\ n \cdot F\ (E_e - E^0)}{R \cdot T}) = n \cdot F \cdot k^0 \cdot a_{ox} \cdot \exp(-\frac{\beta \cdot n \cdot F\ (E_e - E^0)}{R \cdot T}) \quad (77)$$

Substituting Equation 77 in Equation 76, noting that cell potential minus the equilibrium potential equals the activation overpotential since exclusively charge transfer related effects are considered and introducing the charge transfer coefficient as the product of the symmetry factor and the number of electrons involved results in the Butler - Erdey-Grúz - Volmer Equation 31.

$$i = i_o[exp(\frac{\alpha_a \cdot F}{R \cdot T}\ \phi_{act}) - exp(-\frac{\alpha_c \cdot F}{R \cdot T}\ \phi_{act})] \quad (31)$$

Equation 31 gives the impression that an increasing temperature raises the activation overpotential. However, raising the temperature raises the exchange current density with a multiple. Therefore, key to lower the activation overpotential is actually by increasing the exchange current density.

A schematic of the reversible cell voltage minus the activation losses is given in Figure 61.

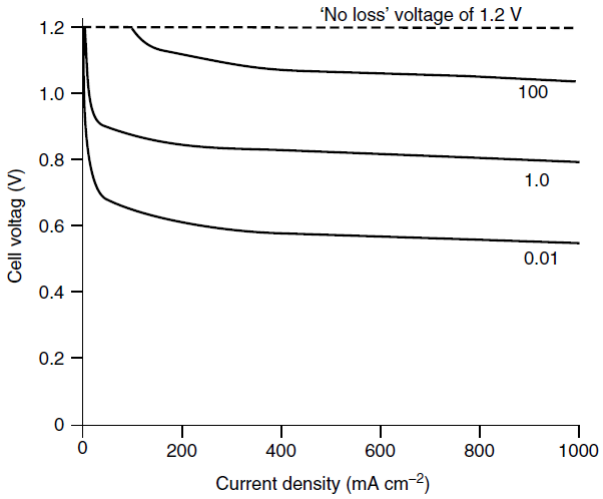

Figure 61: *Effect activation losses on reversible cell voltage [15].*

Ohmic Losses

Ohmic losses are important in all types of fuel cells, especially for SOFCs [15]. Ohmic losses involve both resistance of electrons through the conducting material as well as the resistance of ions through the electrolyte. The mass transport of ions through the electrolyte happens in three ways;

- Diffusion - induced by a concentration gradient
- Migration - induced by a potential gradient
- Advection - bulk electrolyte flow

Mass transport of ions results in an ionic current. This ionic current must be equal to the current in the external circuit. The ionic current is given in Equation 78 [42].

$$\overrightarrow{i} = z \cdot F \cdot \overrightarrow{N} \quad (78)$$

For an SOFC the advection term is not present due the solid electrolyte. Assuming the concentration is equal over the length of the electrolyte, only migration is responsible for mass transport. This migration term is given in Equation 79 [42].

$$\overrightarrow{N} = -z \cdot \tilde{u} \cdot F \cdot C \, \frac{d\phi}{dx} \tag{79}$$

where $\tilde{u}$ is the ionic electrochemical mobility and ϕ is the electrostatic potential.

Combining Equation 78 and 79 results in Equation 80. Also known as Ohm's law.

$$\overrightarrow{i} = z^2 \cdot \tilde{u} \cdot F^2 \cdot C \, \frac{\Delta\phi_{ohm}}{\tau} = \kappa \, \frac{\Delta\phi_{ohm}}{\tau} \tag{80}$$

where κ is the electrolyte specific conductivity and τ is the thickness of the electrolyte.

Rewriting for the ohmic losses and knowing that the ionic current is equal to the current through the external circuit results in Equation 34.

$$\phi_{ohm} = i \, \frac{\tau}{\kappa} = i \cdot \epsilon \tag{34}$$

Diffusion Losses

Mass transfer losses or concentration losses are losses due to insufficient supply of reactant. The overpotential associated to it, the diffusion overpotential, is a measure of the resistance of the porous electrode of the transport of species to or from the electrochemical sites.
Figure 62 gives a schematic of the diffusion overpotential.

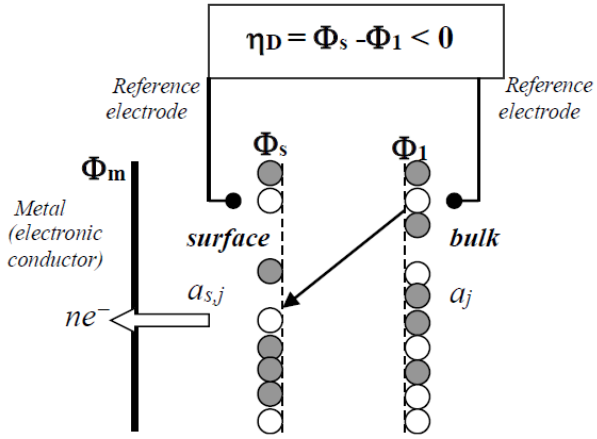

Figure 62: *Schematic of diffusion overpotential. The diffusion overpotential losses are defined as the difference in surface potential minus bulk potential.*

As shown in Figure 62, the diffusion overpotential is defined as the difference between the bulk and the surface potential as in Equation 81.

$$\phi_d = \phi_s - \phi_1 \tag{81}$$

The potential in the bulk and at the surface, Equations 82 and 83, are expressed by combining Equations 30 and 67.

$$\phi_1 = -\frac{\Delta G_o + R \cdot T \ \ln(\Pi a_{s,j}^{s_j})}{n \cdot F} \tag{82}$$

$$\phi_s = -\frac{\Delta G_o + R \cdot T \ \ln(\Pi a_{j}^{s_j})}{n \cdot F} \tag{83}$$

Inserting Equations 82 and 83 in Equation 81, results in the diffusion overpotential in Equation 36.

$$\phi_d = -\frac{R \cdot T}{n \cdot F} \ln(\Pi \frac{a_{s,j}}{a_j}^{s_j}) = -\frac{R \cdot T}{n \cdot F} \sum s_j \ln(\frac{a_{s,j}}{a_j}) \tag{36}$$

Figure 63 gives a schematic polarization curve including the concentration losses, together with the already found activation losses, fuel crossover and ohmic losses.

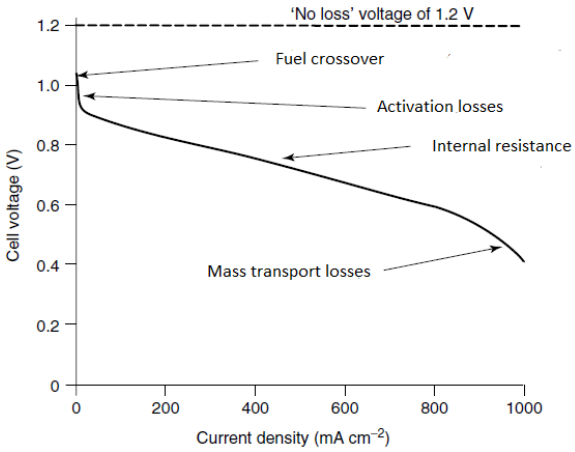

Figure 63: *Schematic of a polarization curve including fuel crossover, activation losses, ohmic losses and mass transport losses.*

Appendix B: Aspen Model and Stream Table Final Solid Oxide Fuel Cell System

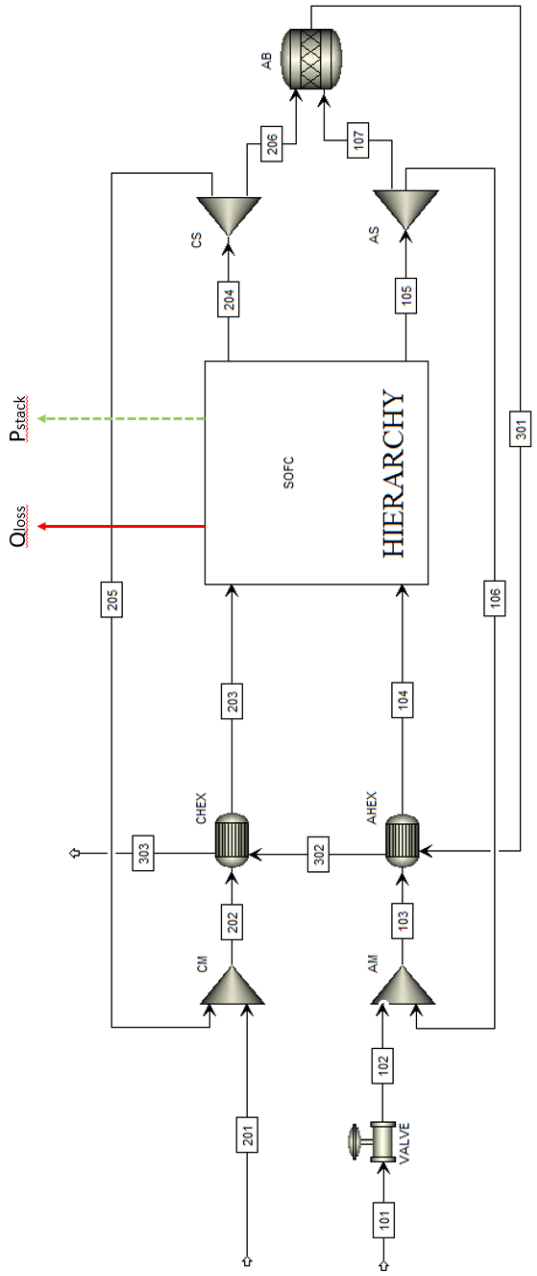

Figure 64: *Aspen model solid oxide fuel cell system.*

Heat and Material Balance Table

Stream ID		101	102	103	104	105	106	107	201	202	203	204	205	206	301	302	303
Temperature	C	25,0	-33,0	-33,0	750,0	850,0		850,0	25,0	235,0	750,0	850,0	850,0	850,0	967,8	851,7	256,7
Pressure	bar	20,000	1,013	1,013	1,013	1,013		1,013	1,013	1,013	1,013	1,013	1,013	1,013	1,013	1,013	1,013
Vapor Frac		0,000	0,196	0,196	1,000	1,000		1,000	1,000	1,000	1,000	1,000	1,000	1,000	1,000	1,000	1,000
Mole Flow	kmol/hr	0,171	0,171	0,171	0,171	0,342	0,000	0,342	2,108	2,774	2,774	2,665	0,666	1,998	2,322	2,322	2,322
Mass Flow	kg/hr	2,916	2,916	2,916	2,916	6,409	0,000	6,409	60,803	79,907	79,907	76,415	19,104	57,311	63,720	63,720	63,720
Volume Flow	cum/hr	0,005	0,653	0,653	14,378	31,561	0,000	31,561	51,533	115,676	232,928	245,629	61,407	184,221	236,455	214,336	100,945
Enthalpy	Gcal/hr	-0,003	-0,003	-0,003	> -0,001	-0,010		-0,010	> -0,001	0,004	0,015	0,016	0,004	0,012	0,002	> -0,001	-0,011
Mole Flow	kmol/hr																
WATER						0,218		0,218							0,257	0,257	0,257
HYDROGEN						0,039		0,039									
NITROGEN						0,086		0,086	1,665	2,220	2,220	2,220	0,555	1,665	1,751	1,751	1,751
AMMONIA		0,171	0,171	0,171	0,171	< 0,001		< 0,001							< 0,001	< 0,001	< 0,001
OXYGEN									0,443	0,554	0,554	0,445	0,111	0,333	0,314	0,314	0,314

Figure 65: *Stream table final solid oxide fuel cell system.*

Appendix C: Final Solid Oxide Fuel Cell System Specifications

Table 14: *Storage system.*

Weight	167.6 kg	
	Ammonia	84.1 kg
	Steel	83.5 kg
Volume	132 L	
d_{tank}	0.631 m	
d_{wall}	8.81 mm	
T_{max}	45 °C	
FoS	5	
ρ_{steel}	7800 kg/m^3	

Table 15: *Solid oxide fuel cell stack.*

Weight	70.5 kg	
	PEN	8.1 kg
	Interconnections	50.7 kg
	Insulation	11.7 kg
Volume	476 L	
	L	0.82 m
	W	0.83 m
	H	0.70 m
Power	9.24 kW	
Efficiency	62.0 %	
Number of cells	240	
Cell area	0.01 m^2	
Cell voltage	0.798 V	
Stack voltage	191.5 V	
Current density	4820 A/m^2	
Ammonia consumption	3.50 kg/h	
Air feed flow rate	58.5 kg/h	
Heat loss	5.3 %	
Fuel utilization	70 %	
Oxygen utilization	25.5 %	
T_{stack}	800 °C	
T_{wall}	50 °C	
p_{stack}	1 bar	

Table 16: *Battery module.*

Capacity	139.6 kWh
Energy density	212 Wh/kg
	344 Wh/L
Weight	657 kg
Volume	406 L

Table 17: *Anodic heat exchanger.*

Flow	Spec	Inlet	Outlet	Unit
Ammonia	Temperature	-33.0	750.0	°C
	Vapor fraction	0.196	1.00	-
	Volume flow	0.79	17.3	$\frac{m^3}{hr}$
	Mass flow	3.50		$\frac{kg}{hr}$
	Density	4.43	0.20	$\frac{kg}{m^3}$
Exhaust	Temperature	1133.8	995.4	°C
	Vapor fraction	1.00	1.00	-
	Volume flow	262.6	236.7	$\frac{m^3}{hr}$
	Mass flow	61.7		$\frac{kg}{hr}$
	Density	0.23	0.26	$\frac{kg}{m^3}$
Design	Duty	3149 W		
	Heat transfer coefficient	2.3 W/m^2/K		
	LMTD	654.0 °C		
	Required heat transfer area	2.09 m^2		
Design	Material	Incoloy 625		
	Configuration	One shell, one tube pass		
	Hot stream	Shell side		
	Tube pattern	3D-triangular		
	Number of tubes	32		
	Tube inner diameter	1.91 cm		
	Tube outer diameter	2.38 cm		
	Tube pitch	2.98 cm		
	Tube length	100 cm		
	Shell inner diameter	23.4 cm		
	Shell outer diameter	24.8 cm		
Size	Volume	48,4 L		
	Tube weight	42.7 kg		
	Shell weight	44.8 kg		
	Weight	87.5 kg		

Table 18: *Cathodic heat exchanger.*

Flow	Spec	Inlet	Outlet	Unit
Air	Temperature	25.0	750.0	°C
	Vapor fraction	1.00	1.00	-
	Volume flow	49.3	169.4	$\frac{m^3}{hr}$
	Mass flow	58.2		$\frac{kg}{hr}$
	Density	1.18	0.34	$\frac{kg}{m^3}$
Exhaust	Temperature	995.4	406.2	°C
	Vapor fraction	1.00	1.00	-
	Volume flow	236.7	126.8	$\frac{m^3}{hr}$
	Mass flow	61.7		$\frac{kg}{hr}$
	Density	0.26	0.49	$\frac{kg}{m^3}$
Design	Duty	12605 W		
	Heat transfer coefficient	8.8 $W/m^2/K$		
	LMTD	308.3 °C		
	Required heat transfer area	4.65 m^2		
Design	Material	Incoloy 625		
	Configuration	One shell, one tube pass		
	Hot stream	Shell side		
	Tube pattern	3D-triangular		
	Number of tubes	23		
	Tube inner diameter	1.91 cm		
	Tube outer diameter	2.38 cm		
	Tube length	300 cm		
	Shell inner diameter	20.5 cm		
	Shell outer diameter	21.9 cm		
Size	Volume	113 L		
	Tube weight	92.2 kg		
	Shell weight	118.1 kg		
	Weight	210.2 kg		

Appendix D: Additional Figures

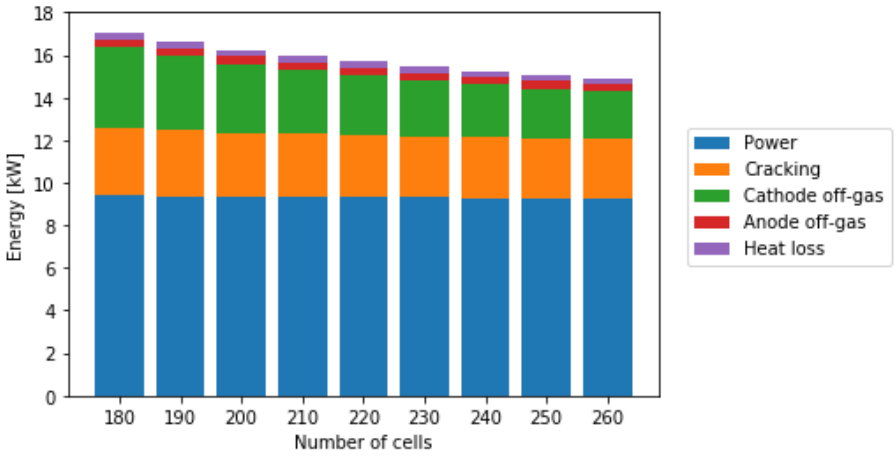

Figure 66: *Energy distribution solid oxide fuel cell stack as function of number of cells at $U_f = 80$ %, $r_c = 0$ % and $r_a = 0$ %.*

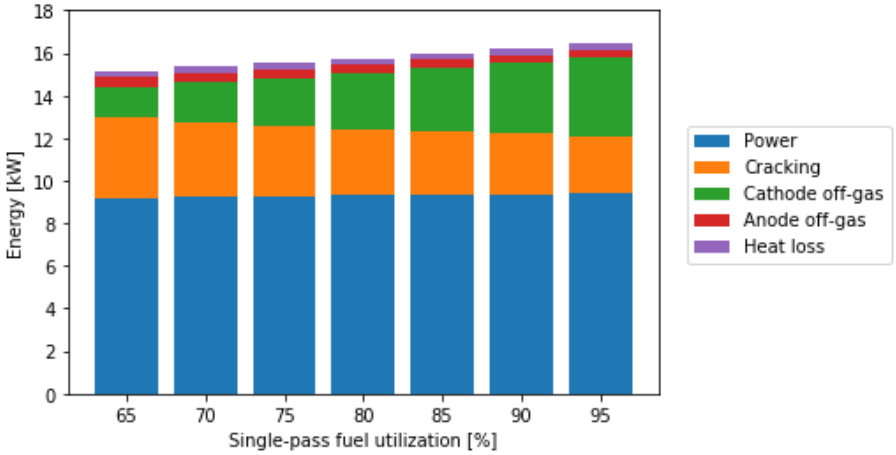

Figure 67: *Energy distribution solid oxide fuel cell stack as function of single-pass fuel utilization at # = 210, $r_c = 0$ % and $r_a = 0$ %.*

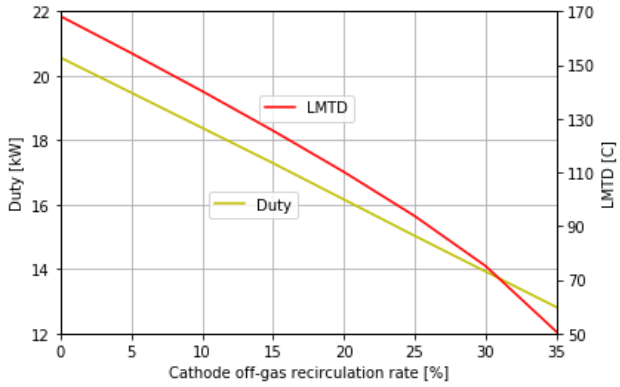

Figure 68: *Heat duty and logarithmic mean temperature difference cathodic heat exchanger as function of cathode off-gas recirculation rate at #= 210, U_f = 80 % and r_a = 0 %.*

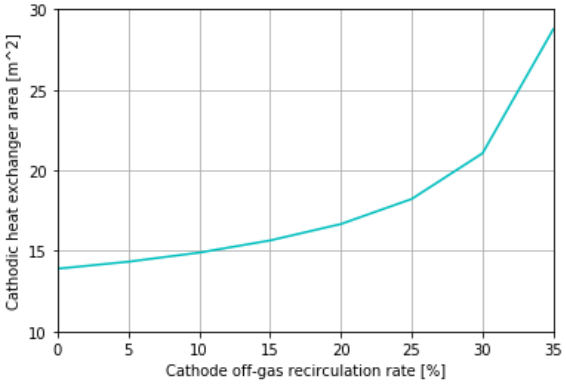

Figure 69: *Required heat transfer area cathodic heat exchanger as function of cathode off-gas recirculation rate at #= 210, U_f = 80 % and r_a = 0 %.*

Appendix E: Aspen Model Alternative Solid Oxide Fuel Cell Configuration

The SOFC model represented in section 4.1.1 could be simplified: The HOR and Cathode could be combined in a RStoich module labelled by AN+CA, since stoichiometry is known by the single-pass fuel utilization. The alternative approach of the SOFC model as in Aspen Plus is shown in Figure 70.

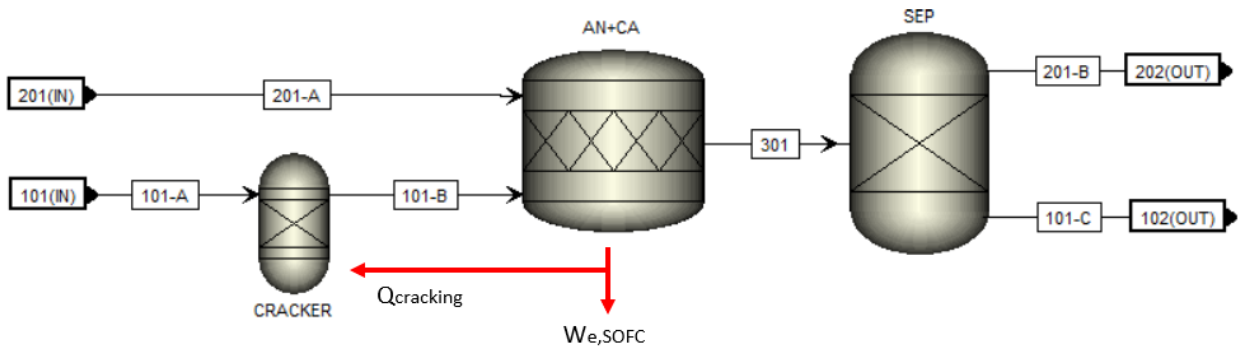

Figure 70: *Aspen Plus model alternative solid oxide fuel cell.*

The RStoich module has only one outlet stream. Therefore, a separator module labelled by SEP is implemented to divide the outlet stream in a anodic and cathodic stream. One reaction for the RStoich module is given: Hydrogen reacts with oxygen to water with a conversion equal to the single-pass fuel utilization. For the separator, the specification for the cathodic product stream will be given. This includes oxygen and nitrogen only. For the oxygen the split fraction is equal to 1, since no oxygen is present in the anode off-gas. The amount of nitrogen is equal to the amount of nitrogen entering in the cathode inlet stream.

For the alternative SOFC model, the energy balance is equal to the energy balance of the current SOFC model in Equation 19. An example of a stream table for the alternative SOFC model is shown in Figure 71.

Heat and Material Balance Table							
Stream ID		SOFC.101-A	SOFC.101-B	SOFC.201-A	SOFC.301	SOFC.101-C	SOFC.201-B
Temperature	C	700,0	800,0	700,0	800,0	800,0	800,0
Pressure	bar	1,000	1,000	1,000	1,000	1,000	1,000
Vapor Frac		1,000	1,000	1,000	1,000	1,000	1,000
Mole Flow	kmol/hr	0,814	1,629	35,469	36,578	1,629	34,950
Mass Flow	kg/hr	13,869	13,869	1023,281	1037,150	30,477	1006,673
Volume Flow	cum/hr	65,883	145,335	2870,481	3264,400	145,298	3119,090
Enthalpy	Gcal/hr	-0,003	0,009	0,176	0,152	-0,049	0,202
Mole Flow	kmol/hr						
WATER					1,038	1,038	
HYDROGEN			1,221		0,183	0,183	
NITROGEN			0,407	28,020	28,427	0,407	28,020
AMMONIA		0,814	< 0,001		< 0,001	< 0,001	
OXYGEN				7,448	6,929		6,929

Figure 71: *Stream table alternative SOFC model.*

Appendix F: Derivation of Equations

Energy Balance SOFC stack

Starting with the general energy balance for an open system as in Equation 18:

$$\frac{dE}{dt} = \dot{Q} - \dot{W} + \sum h_i \cdot \dot{m}_i - \sum h_e \cdot \dot{m}_e + H_{source} \tag{18}$$

When defining the control volume of the energy system; electrical work done by the SOFC and heat losses to the environment are leaving the steady-state system. Both the anode and the cathode have an inlet and a outlet stream. This results in Equation 84.

$$0 = -\dot{Q}_{loss} - P_{,stack} + H_{101-A} + H_{201-A} - H_{101-E} - H_{201-E} \tag{84}$$

For each component of the SOFC, the general energy balance can be applied as well. This leads to Equations 85 till Equation 91.

$$Heater\ 1 : 0 = \dot{Q}_{heater1} + H_{203-A} - H_{203-B} \tag{85}$$

$$Cathode : 0 = H_{203-B} - H_{203-C} - H_{203-D} \tag{86}$$

$$Heater\ 2 : 0 = \dot{Q}_{heater2} + H_{203-D} - H_{203-E} \tag{87}$$

$$Heater\ 3 : 0 = \dot{Q}_{heater3} + H_{103-A} - H_{103-B} \tag{88}$$

$$Cracker : 0 = \dot{H}_{cracker} + H_{103-B} - H_{103-C} \tag{89}$$

$$HOR : 0 = -\dot{H}_{HOR} + H_{103-C} + H_{203-C} - H_{103-D} \tag{90}$$

$$Heater\ 4 : 0 = \dot{Q}_{heater4} + H_{103-D} - H_{203-E} \tag{91}$$

Substitute the intermediate enthalpy streams in Equations 85 till 91 results in Equation 92.

$$H_{103-A} + H_{203-A} - H_{103-E} - H_{203-E} = -\dot{Q}_{heater1} - \dot{Q}_{heater2} - \dot{Q}_{heater3} - \dot{H}_{cracker} + \dot{H}_{HOR} - \dot{Q}_{heater4} \tag{92}$$

Finally, combining Equations 84 and 92 gives the energy balance of the SOFC in Aspen Plus as in Equation 19.

$$P_{stack} = -\dot{H}_{HOR} - \dot{H}_{cracker} - (\dot{Q}_{heater1} + \dot{Q}_{heater2}) - (\dot{Q}_{heater3} + \dot{Q}_{heater4}) - \dot{Q}_{loss} \tag{19}$$

Heat losses surroundings

Churchill et al. [39] gives the relation between the Nusselt number and the Rayleigh number Ra for a flat horizontal plate by Equation 93.

$$Nu_{top} = \frac{\lambda \cdot W_{stack}}{\kappa} = 0.14 \cdot Ra_{top}^{\frac{1}{3}} \tag{93}$$

$$Ra_{top} = \frac{(T_{wall} - T_o) \cdot g \cdot W_{stack}^3}{310.65\ K \cdot 1.57^{-5} \cdot 2.21^{-5}}$$

where g is the gravitational constant of 9.81 m/s^2, 1/335.65 K is the expansion coefficient for an ideal gas at the mean air temperature, 1.57E-5 is the kinematic viscosity of air at the mean temperature and 2.21E-5 is the thermal diffusivity of air at the mean temperature.

By inserting the Rayleigh number in Equation 93, the unknown W_{stack} cancels out. Therefore, the heat transfer coefficient λ is constant for the top and is used to calculate the insulation thickness of the top by Equation 21 and 24.

McAdams [40] gives the relation between the Nusselt number and the Rayleigh number for a flat vertical plate by Equation 94. Note that the stack height is known since the insulation thickness of the top is calculated.

$$\bar{Nu}_{sides} = 0.68 + 0,670 \cdot (Ra_{sides} \cdot \psi)^{\frac{1}{4}} \cdot (1 + 1.6E-8 \cdot Ra_{sides} \cdot \psi)^{\frac{1}{12}} \tag{94}$$

$$Ra_{sides} = \frac{(T_{wall} - T_o) \cdot g \cdot H_{stack}^3}{310.65\ K \cdot 1.57^{-5} \cdot 2.21^{-5}}$$

$$\psi = (1 + (\frac{0.493}{Pr})^{\frac{9}{16}})^{-\frac{16}{9}}$$

where Pr is the Prantl number.

With the heat transfer coefficient of the sides, the heat loss from the sides can be calculated by Equation 22. This is substituted in Equation 24 to calculated the insulation thickness of the sides. Last, the heat loss from the top is calculated.

Nernst Potential

Using Equation 67 with the activity for a gas in Equation 68 results in Equation 95.

$$\phi_{rev} = \phi^{\circ}_{rev} - \frac{R \cdot T}{\mu \cdot F}\ ln(\frac{a_{H20}}{a_{H2} \cdot a_{O2}^{0.5}}) = \phi^{\circ}_{rev} - \frac{R \cdot T}{\mu \cdot F}\ ln(\frac{f_{H_2O}\ \frac{p_{H_2O}}{p^{\circ}}}{f_{H_2}\ \frac{p_{H_2}}{p^{\circ}} \cdot (f_{O_2}\ \frac{p_{O_2}}{p^{\circ}})^{0.5}}) \tag{95}$$

The fugacity is 1 for ideal gasses. Furthermore, according to Henry's law, the partial pressure is equal to the product of the molar fraction and the total pressure. Implementing these aspects for a fuel cell according to Equation 4 results in Equation 29.

$$\phi_{rev} = \phi^{\circ}_{rev} - \frac{R \cdot T}{n \cdot F} \ln(\frac{y_{H_2O} \frac{p}{p^{\circ}}}{y_{H_2}\ \frac{p}{p^{\circ}} \cdot (y_{O_2}\ \frac{p}{p^{\circ}})^{0.5}}) = \phi^{\circ}_{rev} - \frac{R \cdot T}{n \cdot F} \ln(\frac{y_{H_2O}}{y_{H_2} \cdot y_{O_2}^{0.5}}) + \frac{R \cdot T}{2 \cdot n \cdot F} \ln(\frac{p}{p^{\circ}}) \tag{29}$$

BE-GV equation

Starting from the Butler - Erdey-Grúz - Volmer Equation 31.

$$i = i_o[\exp(\frac{\alpha_a \cdot F}{R \cdot T}\ \phi_{act}) - \exp(-\frac{\alpha_c \cdot F}{R \cdot T}\ \phi_{act})] \tag{31}$$

Assuming an equal amount of Gibbs free energy goes into lowering the activation barrier of the cathodic reaction and the anodic reaction, i.e. the symmetry factor is 0.5, results in Equations 96 and 97 for the anodic and cathodic transfer coefficients respectively.

$$\alpha_a = (1 - \beta) \cdot \mu = \frac{1}{2}\ \mu = \alpha \tag{96}$$

$$\alpha_b = \beta \cdot \mu = \frac{1}{2}\ \mu = \alpha \tag{97}$$

Inserting Equations 96 and 97 in the Erdey-Grúz - Volmer Equation 31 results in Equation 98.

$$i = i_o[\exp(\frac{\alpha \cdot F}{R \cdot T}\ \phi_{act}) - \exp(-\frac{\alpha \cdot F}{R \cdot T}\ \phi_{act})] = i_o \cdot \frac{1}{2}\ \sinh(\frac{\alpha \cdot F}{R \cdot T}\ \phi_{act}) \tag{98}$$

Rewriting Equation 98 for the overpotential losses results in Equation 32.

$$\phi_{act} = \frac{R \cdot T}{\alpha \cdot F} \sinh^{-1}(\frac{i}{2i_o}) \tag{32}$$

Ammonia storage system

$$d_{inner} = (\frac{6}{\pi} \cdot V_{NH_3})^{1/3} \tag{99}$$

$$V_{storage} = \frac{\pi}{6} \cdot (d_{inner} + 2\tau_{wall})^3 \tag{100}$$

$$m_{steel} = \rho_{steel} \cdot \frac{\pi}{6} \cdot ((d_{inner} + 2\tau_{wall})^3 - d_{inner}^3) \tag{101}$$

Weight and volume heat exchanger

$$\#_{tubes} = \frac{A}{\pi \cdot \frac{d_{tube,inner} + d_{tube,outer}}{2} \cdot L} \tag{102}$$

$$d_{bundle} = d_{tube,outer} \cdot (\frac{\#_{tubes}}{K1})^{1/n1} \tag{103}$$

$$d_{shell,outer} = d_{shell,inner} + 0.014 = d_{bundle} + p_tube + 0.014 \tag{104}$$

$$m = m_{tubes} + m_{shell} = \frac{\pi}{4}(d_{tube,outer}^2 - d_{tube,inner}^2) \cdot L \cdot \#_{tubes} \cdot \rho_{incoloy} + \frac{\pi}{4}(d_{shell,outer}^2 - d_{shell,inner}^2) \cdot L \cdot \rho_{incoloy} \tag{105}$$

$$V = \frac{\pi}{4} \cdot d_{shell,outer}^2 \cdot L \tag{106}$$

Mass of the SOFC components

$$m_{gw} = (V_{SOFC} - \#_{cells,width} \cdot W_{cell} \cdot \#_{cells,height} \cdot L_{cell} \cdot (\tau_{cell} \cdot \#_{cells,length} + \tau_{int}) \cdot \rho_{gw} \tag{107}$$

$$m_{PEN} = W_{cell} \cdot L_{cell} \cdot \tau_{PEN} \cdot \#_{cels,length} \cdot \rho_{PEN} \tag{108}$$

$$m_{int} = (W_{cell} \cdot L_{cell} \cdot 3\tau_{int} \cdot \#_{cell,length} + \tau_{int}) \cdot \rho_{aluminium} \tag{109}$$